INFLUENCE OF THE ELECTRON-PHONON INTERACTION ONTO ELECTRONIC TRANSPORT IN METALS

Dissertation
zur Erlangung des Doktorgrades der Naturwissenschaften
(*Dr. rer. nat.*)

der

Naturwissenschaftlichen Fakultät II
Chemie, Physik und Mathematik

der Martin-Luther-Universität
Halle-Wittenberg

vorgelegt von

Herrn FLORIAN RITTWEGER
geb. am 09.06.1988 in Halle (Saale)

Erstgutachterin: Prof. Dr. Ingrid Mertig
Zweitgutachter: Prof. Dr. Steffen Trimper
Drittgutachter: Prof. Dr. Jaroslav Fabian

Datum der Abgabe: 28.06.2017
Datum der öffentlichen Verteidigung: 31.01.2018
Vorsitz der Promotionskommission: Prof. Dr. Detlef Reichert

Abstract

This work studies the electron-phonon (e-ph) interaction in the archetypal elemental superconductor Pb on the basis of detailed electron and phonon state-dependent discussions. The real and imaginary part of the electron self-energy with respect to the e-ph interaction is used to investigate the influence of the e-ph coupling onto the electrical conductivity and thermopower. The analysis of the e-ph relaxation time and the renormalization of the electronic band structure is thereby of particular interest. The calculations are carried out with *ab initio* methods based on planewaves and pseudopotentials as well as Wannier functions. Subsequently, the transport properties are calculated with the linearized Boltzmann equation including a relaxation time, whose energy-dependency is directly obtained from its state-dependent character. The experimentally observed enhancement of the thermopower in lead at low temperatures can be reproduced and traced back to the peaked structure of the relaxation time at these temperatures without accounting for the phonon-drag effect. The renormalized band structure and its impact onto transport properties are discussed for a model system. It is shown, that the electrical conductivity decreases while the thermopower increases. Furthermore, a band splitting is observable depending on the parameter set of phonon band width, e-ph coupling strength, temperature and electron energy. Conclusively, the combined consideration of the renormalization and the relaxation time is discussed stating that the latter yields the dominant contribution to transport properties in the low-temperature regime.

Abriss

Die vorliegende Arbeit untersucht die Elektron-Phonon (E-Ph) Wechselwirkung im ursprünglichen elementaren Supraleiter Blei auf der Grundlage detaillierter Diskussionen relevanter Größen in Abhängigkeit von Elektron- und Phononzuständen. Dazu wird der Real- und Imaginärteil der Selbstenergie der Elektronen unter Berücksichtigung der E-Ph Wechselwirkung benutzt, um den Einfluss der E-Ph Kopplung auf die elektrische Leitfähigkeit und die Thermokraft zu untersuchen. Die Analyse der E-Ph Relaxationszeit und die Renormalisierung der elektronischen Bandstruktur sind dabei von besonderm Interesse. Die Berechnungen werden mit *ab initio* Methoden durchgeführt, welche auf ebenen Wellen und Pseudopotentialen sowie Wannier Funktionen basieren. Anschließend werden die Transporteigenschaften mit der linearisierten Boltzmann Gleichung berechnet. Es wird eine energieabhängige Relaxationszeit verwendet, deren Energieabhängigkeit direkt aus der Zustandsabhängigkeit gewonnen wird. Die experimentell beobachtete Erhöhung der Thermokraft bei tiefen Temperaturen in Blei kann reproduziert und auf die spezielle Struktur der Relaxationszeit bei diesen Temperaturen zurückgeführt werden, ohne den *phonon-drag* Effekt zu berücksichtigen. Die renormalisierte Bandstruktur und ihr Einfluss auf die Transporteigenschaften werden anhand eines Modellsystems diskutiert. Es wird gezeigt, dass die elektrische Leitfähigkeit abnimmt, wohingegen die Thermokraft zunimmt. Weiterhin ist eine Aufspaltung von elektronischen Zuständen zu beobachten, welche in Abhängigkeit der Parameter Phononenbandbreite, E-Ph Kopplungsstärke, Temperatur und Energie auftreten kann. Abschließend werden die Renormalisierung und die Relaxationszeit kombiniert betrachtet und es wird gezeigt, dass Letztere den entscheidenden Beitrag zu den Transporteigenschaften bei tiefen Temperaturen liefert.

Contents

1. Introduction 1

2. Theory 3
- 2.1. Electronic structure theory 3
  - 2.1.1. Ground state theory 3
  - 2.1.2. Interacting system 11
- 2.2. Boltzmann transport theory 18
  - 2.2.1. Boltzmann equation for electrons 18
  - 2.2.2. Transport coefficients in the Boltzmann theory 23
  - 2.2.3. Boltzmann equation for phonons with electron-phonon interaction 25
  - 2.2.4. Coupled electron and phonon Boltzmann equations 26

3. Results 31
- 3.1. Essential quantities 31
  - 3.1.1. Nesting 31
  - 3.1.2. Electron-phonon matrix elements 34
- 3.2. Properties related to the imaginary part of the electron self-energy 37
  - 3.2.1. Vital transport properties at the Fermi surface 37
  - 3.2.2. State-dependent properties away from the Fermi surface in lead 42
  - 3.2.3. From state- to energy-dependent relaxation times and other approximations 45
  - 3.2.4. Transport properties including electron-phonon interaction 47
- 3.3. The real part of the electron self-energy and its impact on electron properties 49
  - 3.3.1. Effects of the renormalization on the basis of a free electron model 49
  - 3.3.2. Renormalization in metals and possible issues with transport calculations 56
- 3.4. Spectral function and its application in transport calculations 58
  - 3.4.1. Spectral function in experiment and theory 58
  - 3.4.2. Remarks on transport calculations accounting for the full complex electron self-energy 59

4. Summary 63

A. Enlarged figures 65

Bibliography 67

List of publications 75

List of Figures

2.1. Schematic illustration of the pseudopotential approximation 6
2.2. Illustration of certain properties due to the use of *maximally-localized* Wannier functions 10
2.3. Feynman diagrams of the electron and phonon self-energy 11
2.4. Numerical evaluation of the real part of the self-energy according to the Kramers-Kronig transformation 16
2.5. Visualisation of the calculation of the nesting function in copper 17
2.6. Overview of scattering processes between electron states due to absorption or emission of a phonon 20
2.7. Phonon frequency spectrum of Cu and Si with superimposed phonon linewidths 26
2.8. Lorenz number as a function of the thermopower at 300K in n-doped silicon taken from Fiorentini *et. al* 28

3.1. Visualisation of nesting at the Fermi surface of Cu 32
3.2. Nesting function of Pb 33
3.3. Various phonon properties and mode-resolved electron-phonon matrix elements in Pb 34
3.4. State-dependent electron-phonon matrix element and band structure in lead 35
3.5. Fermi surface of lead with superimposed state-dependent electron-phonon relaxation times and group velocities 38
3.6. Band-splitted Fermi surface of lead with superimposed state-dependent electron-phonon relaxation times and group velocities 38
3.7. Matrix elements, relaxation times and phonon properties related to the electron-phonon coupling for a single initial electron state in lead 39
3.8. Illustration of the efficiency factor used while computing the transport relaxation time and transport coupling constant in lead 40
3.9. Convergence of the electron-phonon relaxation time with respect to the **k** point density 40
3.10. Matrix elements and relaxation times at the Fermi surface and phonon properties related to the electron-phonon interaction in n-doped Si 41
3.11. Phonon dispersion, phonon linewidth and electron state-dependent Éliashberg spectral function in lead 43
3.12. State-dependent coupling constant, linewidth and relaxation time due to electron-phonon interaction in lead along the high symmetry line 44
3.13. Comparison of state-dependent transport properties, i.e. relaxation time and coupling strength, with their spectroscopical counterparts 45
3.14. State- and energy-dependent relaxation time in lead due to electron-phonon interaction 46

3.15. Energy- and temperature-dependent relaxation times within various approximations in lead due to electron-phonon interaction . . . 47
3.16. Electrical conductivity and thermopower in lead with respect to electron-phonon interaction . . . 48
3.17. Complex self-energy obtained from an Einstein model at two different temperatures . . 49
3.18. Renormalized band structure of a free electron model . . . 51
3.19. Renormalized band structure of a modeled semiconductor with varying band gap . . . 52
3.20. Graphical solution of the renormalization condition for a self-energy obtained from an Einstein model . . . 52
3.21. Guide to find a splitting of bands in the band structure with respect to temperature, coupling strength and electron energy . . . 53
3.22. Transport distribution function of a renormalized free electron model due to electron-phonon coupling . . . 54
3.23. Electrical conductivity and thermopower of a renormalized free electron model due to electron-phonon coupling . . . 55
3.24. Renormalized band structure and transport distribution function in Pb due to electron-phonon interacion . . . 57
3.25. Photoemission data and obtained self-energy from the Be(0001) surface state taken from LaShell *et. al* . . . 58
3.26. Spectral function of a free electron model with respect to electron-phonon coupling. . 59
3.27. Comparison of the transport distribution function with respect to different considerations of the electron-phonon interaction, i.e. relaxation time, renormalized band structure or both parts combined . . . 60

1 | Introduction

The interaction between electrons and phonons is studied for almost 100 years to explain related phenomena like the temperature-dependent electrical resistivity or conventional superconductivity, which is probably still its most prominent feature. The first heyday of this research was already in the 1950s and 1960s due to the microscopical descriptions of Bardeen, Cooper, Schrieffer, Migdal, Éliashberg [9–11, 32, 33, 98, 101, 102, 120, 122] and others. Nevertheless, calculations based on these theories were only feasible for simple metals or semiconductors within various approximations due to the lack of computational power.

The heavy increase of the latter in the last three decades along with the description of the electron-phonon interaction by first principles theories, i.e. *density functional perturbation theory*, enabled the performance of accurate calculations to gain deeper insights of observed effects due to electron-phonon coupling. Additionally, the possibility to obtain and predict material specific transport properties by *ab initio* calculations attracted a lot of attention and the amount of publications focusing indirectly or directly on transport properties increases. For example, calculating the temperature dependence of band gaps and band structures in semiconductors [44, 90, 91], electron linewidths and lifetimes of metallic surface states [30, 31], elemental metals [77, 124, 125] and semiconductors [17, 123, 131] as well as calculating phonon linewidths and thermal conductivities with respect to electron-phonon coupling [27, 40, 82, 116, 139] is achievable nowadays. The estimation of the electrical resistivity due to the lowest-order variational expression for the solution of the Boltzmann equation started already in the late 90s with the investigation of metals [16, 115]. In the last decade, the focus shifted from metals to semiconductors [81, 113, 134] and 2D systems [21, 50, 65, 80, 82], e.g. MoS_2 and graphene, where the electron mobilities are calculated within different relaxation time approximations. Very recently, the calculation of electron mobilities and electrical resistivities in metals, semiconductors and 2D systems due to an iterative solution of the full Boltzmann equation became available [79] and even the inclusion of the phonon-drag contribution arising from non-equilibrium phonons within *ab initio* calculations is accessible today [140].

Apart from that, in-depth analyses of the coupling constant λ [1, 56, 126] and relaxation time τ [100, 110] in the sense of detailed state-dependent discussions are rare. Furthermore, investigations of the electrical conductivity and thermopower, which are related to renormalization effects due to the electron-phonon interaction are missing throughout the 2000s, altough its impact was discussed controversially in the 20th century [48, 64, 85, 111].

Embedded in this context, the aim of this thesis is to investigate the electron-phonon interaction in terms of a detailed electron and phonon state-dependent analysis with *ab initio* methods. Therefore, the coupling constant, the relaxation time as well as related quantities and renormalization effects are discussed in lead, which is an archetypal elemental superconductor. The influence onto the electrical conductivity and thermopower is thereby of particular interest.

The thesis is divided in two major parts. First, the basic ideas of electronic structure calculations are given. The concepts of the two ground state theories, *density functional theory* and *density functional perturbation theory*, are discussed along with the introduction of the Wannier representation to obtain the electronic band structure, the phonon spectrum and the electron-phonon matrix elements (section 2.1.1). Subsequently, the concept of the *self-energy* in an interacting electron system with respect to the electron-phonon interaction is introduced (section 2.1.2). The first part closes with an evaluation of the Boltzmann transport theory under the influence of the electron-phonon interaction. Here, electrons (section 2.2.1) and phonons (section 2.2.3) are treated indepently as well as fully coupled to each other (section 2.2.4). The second part deals with the properties and consequences of the electron-phonon coupling in solids. The beginning is addressed to the electron-phonon matrix elements and the nesting function (section 3.1). Later on, the discussion is splitted with respect to the investigation of the imaginary (section 3.2) and real part of the self-energy (section 3.3). Especially, the relaxation time and renormalization effects in addition to their influence on transport properties are investigated. Finally, the spectral function and a coupled description due to the real and imaginary part are discussed (section 3.4). A summary will close the thesis.

2 | Theory

2.1. Electronic structure theory

The following chapter addresses the theoretical description of the electronic structure of a solid from first principles meaning that the formalism does not include any empirical parameters.

The evaluation of such a concept started already in the beginning of the 20th century with the upcoming field of quantum mechanics and leads to the formulation of the *density functional theory* (DFT). The latter is a so called ground state theory, where the interaction of the electrons with its surrounding is neglected. In the beginning of the first part of this chapter, a brief introduction into the density functional theory is given. Later on, the treatment of phonons wihtin DFT as a perturbation is discussed, which leads to the *density functional perturbation theory* (DFPT). In the end of this part, the concept of Wannier functions is introduced, which enables the mapping of *ab initio* calculated quantities onto analytical expressions. As discussed later, this mapping crucially promotes the investigation of the electron-phonon interaction in solid state systems.

The results obtained in the first part of this chapter are based on an effective, non-interacting and single-particle picture. While different perturbations, e.g. phonons, can be treated within DFPT, a complete physical picture beyond the ground state theory requires a description, which directly addresses many-body effects. According to the electron-phonon interaction, the most important effects are the lifetime-broadening of the electron and phonon states as well as their renormalization. The method of choice is typically a Green's function approach with the use of Feynman diagrams, which represents the interaction of all quasi-particles among and between each other. Regarding the electron-phonon interaction, the simplest approximation in the electron and phonon self-energy allows for a calculation of both quantities using only results from DFPT. Since the 50's, many well-known scientists like Fröhlich, Bardeen, Engelsberg and Schrieffer contributed to the description of the electron-phonon interaction within a first principle environment, which is used nowadays. Really good overviews on different aspects of the historical development are provided by Poncé [109] and Giustino [42]. Additionally, most of the technical details are included there as well and the second part of this chapter will focus on the final expressions of the self-energies only, since they are of major interest in this thesis.

2.1.1. Ground state theory

Density functional theory

In modern solid state physics it is necessary to calculate physical properties of an material based on the quantum mechanical description of electrons (e) and nuclei (n) interacting with themselves and each other. However, a straight-forward solution of the Schroedinger equation with the corresponding Hamiltonian $H = H_{\mathrm{n}}(\mathbf{R}) + H_{\mathrm{e}}(\mathbf{r}) + H_{\mathrm{en}}(\mathbf{r}, \mathbf{R})$ depending on the coordinates of the electrons $\mathbf{r}$ and nuclei

$\mathbf{R}$, is impossible due to the large number of particles in a solid and simplifications have to be made. First, the adiabatic approximation proposed by Born and Oppenheimer in 1927 enables the separation of the motion of electrons and nuclei. Hence, a product ansatz for the many-body wavefunction $\Phi(\mathbf{r}, \mathbf{R})$ allows for an isolated solution of the electronic part of H, in which $\mathbf{R}$ remains as a parameter. H_e reads as

$$H_\mathrm{e} = \sum_{i=1}^{N} \frac{\hat{\mathbf{p}}_i^2}{2m} + \frac{1}{2} \sum_{i,j \neq i} \frac{e^2}{\left|\mathbf{r}_i - \mathbf{r}_j\right|} + \sum_{i=1}^{N} v_\mathrm{ext}(\mathbf{r}_i) \quad . \tag{2.1.1}$$

The first term is the operator of the kinetic energy T with the momentum operator $\hat{\mathbf{p}}$. The second term accounts for the Coulomb repulsion among the electrons V_ee and the last term describes an external potential V_ext, which is related to the interaction of the electrons with the localized nuclei. Nevertheless, solving the remaining interacting electron system is still extremly demanding and impracticable. Almost 40 years later, Hohenberg and Kohn [60] introduced an efficient way to translate the many-electron problem in terms of a one-electron charge density $n(\mathbf{r})$ description, which is the basis for today's density functional theory (DFT) calculations. They propose, that in an interacting electron-system the external potential is exactly determinded by the ground state charge density $n^0(\mathbf{r})$ and furhter on, the sought ground state energy is a unique functional of $n(\mathbf{r})$, which has its global minimum for the ground state charge density

$$E_0 = E[n^0(\mathbf{r})] \leq E[n(\mathbf{r})] \quad . \tag{2.1.2}$$

Based on these ideas, Kohn and Sham established a practical formalism to map the interacting electron system onto a non-interacting one embedded in an effective potential [72]. Herein, the description of the many-body interaction of the energy functional $E[n]$ is hidden in an exchange-correlation functional $E_\mathrm{xc}[n]$, which functional derivative is the exchange correlation potential, $v_\mathrm{xc} = {}^{\partial E_\mathrm{xc}[n]}\!/_{\partial n}$. Then, the kinetic energy functional is described by the non-interacting electron system

$$T[n] = \frac{1}{2m} \sum_{i=1}^{N} \int \mathrm{d}\mathbf{r}\, \psi_i^*(\mathbf{r}) \hat{\mathbf{p}}^2 \psi_i(\mathbf{r}) \quad . \tag{2.1.3}$$

$\psi_i(\mathbf{r})$ are the corresponding one-electron wavefunctions and the charge density is given by a sum over all occupied states

$$n(\mathbf{r}) = \sum_{i}^{\mathrm{occ.}} \left|\psi_i(\mathbf{r})\right|^2 \quad . \tag{2.1.4}$$

The interaction of the electrons among each other is accounted for in the Hartree energy functional

$$E_\mathrm{H}[n] = \frac{e^2}{2} \int \mathrm{d}\mathbf{r} \int \mathrm{d}\mathbf{r}' \frac{n(\mathbf{r}) n(\mathbf{r}')}{|\mathbf{r} - \mathbf{r}'|} \quad . \tag{2.1.5}$$

Adding the energy functional of the external potential, the total energy functional of the charge density reads as

$$E[n] = T[n] + \int \mathrm{d}\mathbf{r}\, v_\mathrm{ext}(\mathbf{r}) n(\mathbf{r}) + \frac{e^2}{2} \int \mathrm{d}\mathbf{r} \int \mathrm{d}\mathbf{r}' \frac{n(\mathbf{r}) n(\mathbf{r}')}{|\mathbf{r} - \mathbf{r}'|} + E_\mathrm{xc}[n] \quad . \tag{2.1.6}$$

The charge density, which minimizes the energy functional is calculated self-consistently via the variational principle ${}^{\partial E[n]}\!/_{\partial n} = 0$. This leads to the Kohn-Sham-equations, which have the form of a single-particle Schroedinger-equation within an effective potential

$$\begin{aligned} \left[\frac{\hat{\mathbf{p}}^2}{2m} + v_{\text{eff}}(\mathbf{r})\right]\psi_i(\mathbf{r}) &= \epsilon_i \psi_i(\mathbf{r}) \quad , \\ v_{\text{eff}} &= v_{\text{ext}}(\mathbf{r}) + v_{\text{xc}} + e^2 \int d\mathbf{r}' \frac{n(\mathbf{r}')}{|\mathbf{r}-\mathbf{r}'|} \quad . \end{aligned} \tag{2.1.7}$$

The last term in the effective potential is the Hartree term, which describes the Coulomb repulsion between the electrons.

Later, MacDonald and Vosko [86] showed, that the statements of Hohenberg and Kohn also holds in a fully-relativistic description and the interacting relativistic electron system can be treated in a similiar way yielding the Kohn-Sham-Dirac equations.

In principal, the Kohn-Sham and Kohn-Sham-Dirac-equations are exact if the exchange and correlation potential would be known. Since this is not the case, approximations regarding v_{xc} are required and searching for these is still a main task in DFT. Up to now, the *local density approximation* (LDA) is probably the most relevant approximation with the highest cost-benefit relationship due to its simple footing on the homogenous electron gas (HEG). Therein, $E_{\text{xc}}^{\text{LDA}}$ is approximated by ε_{xc}, which is the exchange-correlation energy per particle of the HEG. The charge density of the exact and the approximated energy functional has to be equal. Finally, $E_{\text{xc}}^{\text{LDA}}$ reads as [72]

$$E_{\text{xc}}^{\text{LDA}}[n] = \int d\mathbf{r}\, n(\mathbf{r})\varepsilon_{\text{xc}}(\mathbf{r}) = -\frac{3}{4}e^2\left(\frac{3}{\pi}\right)^{1/3} \int d\mathbf{r}\,(n(\mathbf{r}))^{4/3} \quad . \tag{2.1.8}$$

This quantity is often calculated with quantum Monte Carlo techniques and afterwards parametrized to fit the analytical limit. The used parametrization in this work is provided by Perdew and Zunger [105]. Within LDA, the lattice constants are usually underestimated while phonon frequencies are typically overestimated. More complicated approximations like the generalized gradient approximation (GGA), which is based on a functional of the charge density and its derivative, may improve these problems.

Planewaves and pseudopotentials

Since DFT calculations involving all electrons are still demanding and need large computational efforts, planewaves combined with pseudopotentials are favourable to speed up calculations and reduce the computational cost.

Expanding the all-electron wavefunction ψ^{AE} in terms of planewaves, which are eigenfunctions of the kinetic energy operator $T = -\hbar^2\Delta/2m$, seems reasonable as long as the non-localized states are dominant. Starting with the periodicity of the crystal lattice and applying Blochs theorem, the Fourier series of the wavefunction reads as

$$\psi_{\mathbf{k}}(\mathbf{r}) = \sum_{\mathbf{G}} c_{\mathbf{k}+\mathbf{G}}\, e^{i(\mathbf{k}+\mathbf{G})\mathbf{r}} \tag{2.1.9}$$

with $\mathbf{G}$ being a reciprocal lattive vector and $c_{\mathbf{k}+\mathbf{G}}$ are the Fourier expansion coefficients. In principal, the transformed Kohn-Sham equations could be solved exactly for infinite number of $\mathbf{G}$. Practically, a direct solution is impossible due to the infinite sum. Therefore, the expansion into planwaves is truncated for a certain cutoff energy $E_{\text{cut}} \leq \frac{|\mathbf{k}+\mathbf{G}|^2}{2m}$, which limits the number of $\mathbf{G}$-vectors used. Unfortunately, wavefunctions of localized core or semi-core states show detailed features and require a large basis set,

Figure 2.1.: Schematic illustration of the pseudopotential approximation (ψ^{PS}, V^{PS}) to the all-electron wavefunction ψ^{AE} and potential V. Inside the core radius r_{c}, the strong core potential is replaced by a soft pseudopotential and the ground state pseudo-wavefunction is node-less while outside r_{c}, both quantities have to match their all-electron counterparts.

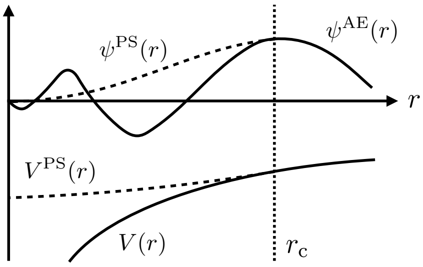

i.e. large E_{cut}.

The idea of a pseudopotential is to overcome this problem due to a simplified description of the core states based on a frozen core approximation. The core electrons are eliminated from the calculation and only the valence electrons remain, since they determine the chemical and physical properties of a system. An appropriate pseudopotential should screen the steep and strong core potential as much as possible, while securing that the node-less ground state pseudo-wavefunction ψ^{PS} is identical to the all-electron wavefunction outside a certain core radius r_{c} as shown in figure 2.1. Beyond these general conditions, there are several requirements for a pseudopotential related to its specific type. In the case of norm-conserving pseudopotentials [106], $\psi^{\mathrm{PS}}(r)$ is allowed to differ from $\psi^{\mathrm{AE}}(r)$ inside r_{c} but the integrated charge, and therefore the norm, has to be conserved,

$$\int_{r<r_{\mathrm{c}}} \mathrm{d}r\, r^2 \left|\psi^{\mathrm{PS}}(r)\right|^2 = \int_{r<r_{\mathrm{c}}} \mathrm{d}r\, r^2 \left|\psi^{\mathrm{AE}}(r)\right|^2 \quad . \tag{2.1.10}$$

Another criterion is the transferability, which means that a pseudopotential should behave equally when used in different chemical environments and the scattering properties of ψ^{AE} should be accurately described by ψ^{PS}. It is measured with the logarithmic derivatives at r_{c} and a reference energy E of the occupied states,

$$\frac{1}{\psi^{\mathrm{PS}}(r_{\mathrm{c}}, E)} \frac{\mathrm{d}\psi^{\mathrm{PS}}(r_{\mathrm{c}}, E)}{\mathrm{d}r} = \frac{1}{\psi^{\mathrm{AE}}(r_{\mathrm{c}}, E)} \frac{\mathrm{d}\psi^{\mathrm{AE}}(r_{\mathrm{c}}, E)}{\mathrm{d}r} \quad . \tag{2.1.11}$$

A pseudopotential generated under these conditions still turns out to be relatively hard and requires a large energy cutoff for the expansion of the planewave basis set. To further reduce E_{cut}, one can drop the norm-conserving constraint of eq. 2.1.10 and allows for an additional softening of the core potential, which is then known as ultrasoft pseudopotential [132]. Removing the constraint, one has to deal with some minor problems caused by the pseudo-wavefunctions, which now do not have to be normalized. The pseudo-charge density has to be calculated different from $\sum \left|\psi^{\mathrm{ps}}\right|^2$ to obtain the correct charge and additional terms appear in the secular equation while calculating the eigenvalues. Overall this might lead to a lower transferability of the pseudopotential but the cost reduction in calculations is worth the effort to generate pseudopotentials, which fit only a few systems.

Density functional perturbation theory

To account for an accurate description of a large variety of phenomena based on lattice dynamics only, such as Raman spectra, neutron-diffraction spectra, specific heat, thermal conductivity or based on the interaction of electrons and phonons, like finite temperature resistivity, the low-temperature phonon-drag effect and superconductivity, detailed knowledge about the vibrational spectrum and the electron-phonon interaction in the system is needed.

Supercell calcuations with imprinted lattice perturbations provide access to the vibrational spectrum.

They are methodically relatively simple but the computational effort increases rapidly with the size of the supercell. Hence, this approach is impracticle for systems with a large unit cell or for systems having stronger long-range interactions between the atoms in the supercell.

A different approach is given by density functional perturbation theory (DFPT) [12, 13, 39, 45, 46], where linear perturbation theory is applied within DFT. According to the Born-Oppenheimer approximation, the dynamics of the electrons and the lattice are separated, coupled by the parameter $\mathbf{R}$. Subsequently, a variation of $\mathbf{R}$ can be treated as a perturbation of the electronic ground state energy $E(\mathbf{R})$ and charge density with respect to the atomic positions. The density itself and its linear response to a lattice distortion is directly related to the matrix of the interatomic force constants (IFCs) in real space $C_{i,j}^{\alpha\beta}(\mathbf{R})$, where i, j are cartesian coordinates and α, β denote the atomic position within the unit cell [39]. $E(\mathbf{R})$ is also called the Born-Oppenheimer energy and the eigenvalues of its Hessian give the vibrational modes ω, while the corresponding eigenvectors describe the real-space motion of the atoms:

$$\det\left|\frac{1}{\sqrt{M_\alpha M_\beta}}C^{\alpha\beta}(\mathbf{R}) - \omega^2\right| = 0 \quad \text{and} \quad C^{\alpha\beta}(\mathbf{R}) = \frac{\partial^2 E(\mathbf{R})}{\partial \mathbf{R}_\alpha \partial \mathbf{R}_\beta} \quad . \tag{2.1.12}$$

In periodic crystals, the IFCs are Fourier-transformed yielding the dynamical matrix $D^{\alpha\beta}(\mathbf{q})$, which enables the calculation of the vibrational spectra via the secular equation

$$\sum_\beta D^{\alpha\beta}(\mathbf{q})\mathbf{u}_\beta(\mathbf{q}\nu) = \omega_{\mathbf{q}\nu}^2 \mathbf{u}_\alpha(\mathbf{q}\nu) \quad , \tag{2.1.13}$$

where $\mathbf{u}_\alpha$ is the displacement from the equilibrium position $\mathbf{R}_\alpha$. Equation 2.1.13 probably provides the greatest advantage of the DFPT over the supercell-approach in periodic systems because the spectra can be calculated at every arbitrary chosen phonon wave vector. Additionally, the electron-phonon matrix element $g_{\mathbf{k},\mathbf{k}+\mathbf{q}}^{\mathbf{q}\nu,nm}$, which is the main ingredient of the electon-phonon interaction, can be obtained as by-product. It is defined as the derivative of the perturbed potential with respect to a lattice distortion, which is directly related to the results obtained by DFPT.

The derivatives of the ground state energy with respect to a lattice distortion in eq. 2.1.12 are obtained via the Hellmann-Feynman theorem [36, 57] and depend clearly on the ground state charge density and its linear response to the distortion.

$$\frac{\partial E(\mathbf{R})}{\partial \mathbf{R}_\alpha} = \langle\psi|\frac{\partial H(\mathbf{R})}{\partial \mathbf{R}_\alpha}|\psi\rangle = \int d\mathbf{r}\frac{\partial V(\mathbf{r},\mathbf{R}_\alpha)}{\partial \mathbf{R}_\alpha}n(\mathbf{r},\mathbf{R}) \tag{2.1.14}$$

$$\frac{\partial^2 E(\mathbf{R})}{\partial \mathbf{R}_\alpha \partial \mathbf{R}_\beta} = \int d\mathbf{r}\frac{\partial^2 V(\mathbf{r},\mathbf{R}_\alpha)}{\partial \mathbf{R}_\alpha \partial \mathbf{R}_\beta}n(\mathbf{r},\mathbf{R}) + \int d\mathbf{r}\frac{\partial n(\mathbf{r},\mathbf{R})}{\partial \mathbf{R}_\alpha}\frac{\partial V(\mathbf{r},\mathbf{R})}{\partial \mathbf{R}_\alpha} \tag{2.1.15}$$

Following Baroni *et. al* [13], the response $\partial n(\mathbf{r},\mathbf{R})/\partial \mathbf{R}_\alpha$ can be obtained by linearising equation 2.1.4 and 2.1.7. The first-order correction of the wave function, $\psi^{(1)}$, is given by perturbation theory as the solution of a Sternheimer-type of equation,

$$\left(H^{(0)} - \epsilon_i^{(0)}\right)\psi^{(1)} = -\left(\Delta v_{\mathrm{KS}} - \epsilon_i^{(1)}\right)\psi^{(0)} \quad , \tag{2.1.16}$$

$$\Delta v_{\mathrm{KS}}(\mathbf{r}) = V_{\mathrm{ext}}^{(1)}(\mathbf{r}) + e^2\int d\mathbf{r}'\frac{n^{(1)}(\mathbf{r}')}{|\mathbf{r}-\mathbf{r}'|} + \int d\mathbf{r}'\frac{\partial v_{\mathrm{xc}}(n)}{\partial n}\Big|_{n=n(\mathbf{r})} n^{(1)}(\mathbf{r}') \quad , \tag{2.1.17}$$

$$\epsilon^{(1)} = \langle\psi_i^{(0)}|\Delta v_{\mathrm{KS}}|\psi_i^{(0)}\rangle \quad , \tag{2.1.18}$$

with $H^{(0)}$ being the unperturbed Kohn-Sham Hamiltonian. Δv_{KS} and $\epsilon^{(1)}$ are the first-order corrections to the potential and eigenvalue, where the normalization condition $\langle\psi_i|\psi_i\rangle = 1$ with the strong constraint $\langle\psi_i^{(1)}|\psi_i^{(0)}\rangle = 0$ is applied. The correction in the charge-density reads as

$$n^{(1)}(\mathbf{r}) = 4\sum_i^{\text{occ.}} \psi_i^{(0)*}(\mathbf{r})\psi_i^{(1)}(\mathbf{r}) \quad . \tag{2.1.19}$$

Finally, equations 2.1.16-2.1.19 form a set of equations, which are similar to the Kohn-Sham equations in an unperturbed system. Obviously, this set of equations has to be solved self-consistently due to the dependency of $H^{(1)}$ on $n^{(1)}$. The aforementioned electron-phonon matrix element in Born-approximation is then given by

$$g_{\mathbf{k},\mathbf{k}+\mathbf{q}}^{\mathbf{q}\nu,nm} = \left(\frac{\hbar}{2M\omega_{\mathbf{q}\nu}}\right)^{1/2} \langle\psi_{\mathbf{k}+\mathbf{q}m}^{(0)}|\delta v_{\text{KS}}^{\mathbf{q}\nu}|\psi_{\mathbf{k}n}^{(0)}\rangle \quad . \tag{2.1.20}$$

where $\delta v_{\text{KS}}^{\mathbf{q}\nu}$ is the change in the self-consistent potential with respect to a phonon perturbation.

An application of the formalism to metals requires a clear separation between occupied and unoccupied states. In principle, this is possible for vanishing electronic temperature but the amount of $\mathbf{k}$ points, which is needed at the Fermi surface would be quite large. One practicle implementation is based on the smearing-technique, where each Kohn-Sham state is broadend by a smearing function [41],

$$f(\epsilon,\sigma) = \frac{1}{\sigma}\tilde{\delta}\left(\frac{\epsilon}{\sigma}\right) \quad , \tag{2.1.21}$$

with the conditions

$$\int \mathrm{d}\epsilon\, f(\epsilon,\sigma) = 1 \quad \text{and} \quad \tilde{\delta} \xrightarrow{\sigma\to 0} \delta \quad , \tag{2.1.22}$$

where δ is the well-known Dirac δ-distribution and σ is a variable and manually eligible smearing parameter. Several types of smearing functions, e.g. Fermi-Dirac broadening, Gaussians, Methfessel-Paxton [97] or Marzari-Vanderbilt smearing functions [94] are commonly applied but which one is finally used, is usually an individual choice. Throughout this thesis, the Fermi-Dirac broadening is used, which is the derivative of the Fermi-Dirac distribution function

$$f = \frac{1}{e^{(\epsilon-\mu)/k_{\text{B}}T} + 1} \quad . \tag{2.1.23}$$

Starting from the modified charge-density,

$$n(\mathbf{r},\sigma) = \sum_i^{\text{occ.}} \frac{1}{\sigma}\tilde{\delta}\left(\frac{\epsilon-\epsilon_i}{\sigma}\right)\left|\psi_i(\mathbf{r})\right|^2 \quad , \tag{2.1.24}$$

evaluating the derivatives of the ground state energy with respect to a lattice distortion is done analog and nearly straight-forward to equation 2.1.14 and 2.1.15. From a computational perspective, the advantage of this technique is the reduction of required $\mathbf{k}$ points in the Brillouin zone to an acceptable amount. The disadvantage is that the total energy now depends on the smearing parameter and convergence has to be tested with respect to chosen parameters.

Wannier representation

The solutions of the Kohn-Sham equations in DFT or their counterpart in DFPT are usually written in terms of Bloch states

$$\psi_{\mathbf{k}n}(\mathbf{r}) = e^{i\mathbf{k}\cdot\mathbf{r}} u_{\mathbf{k}n}(\mathbf{r}) \quad , \tag{2.1.25}$$

where $u_{\mathbf{k}n}(\mathbf{r})$ accounts for the periodicity of the Hamiltonian and the lattice. Bloch states are extended and highly delocalized, which is unattractive in certain situations, e.g. studying chemical bondings.

In 1937, Gregory Wannier introduced an alternative representation called Wannier functions, which uses spatially-localized oribtals [135]. In the last years, this idea was picked up by Marzari and Vanderbilt, which found an iterative procedure to transform Bloch states, obtained from *ab initio* calculations, into *maximally-localized* Wannier functions (MLWFs) [92, 93]. Based on these MLWFs, a team around Giustino and Noffsinger developed the program EPW [43, 103, 110]. It provides an efficient way to calculate a huge number of electron-phonon (e-ph) matrix elements (MEs), which is necessary to investigate the interaction of electrons and phonons in detail. The main advantage is the mapping of self-consistently calculated e-ph MEs at a few **k** and **q** points to an analytical expression, which enables an interpolation of the MEs to an arbitrary large amount of **k** and **q** points with high accuracy and a comparable low computational effort.

The construction of Wannier functions $w_{\mathbf{R}m}(\mathbf{r})$ out of Bloch functions is given by

$$w_{\mathbf{R}m}(\mathbf{r}) = \frac{V}{(2\pi)^3} \int \mathrm{d}\mathbf{k} e^{-i\mathbf{k}\cdot\mathbf{R}} \sum_m U_{\mathbf{k}}^{nm} \psi_{\mathbf{k}n}(\mathbf{r}) \quad , \tag{2.1.26}$$

which is a generalized Fourier transformation in momentum **k** and lattice vector **R**. V is the primitive cell volume in real space and the **k**-integration is performed over the Brillouin zone. If the rotation matrix $U_{\mathbf{k}}^{nm}$, which accounts for possible bandmixing, is unitary, the Wannier functions are orthonormal. The Wannier representation in equation 2.1.26 is non-unique due to an arbitrary phase factor $e^{i\phi(\mathbf{k})}$ hidden in $U_{\mathbf{k}}^{nm}$, which is periodic in reciprocal space. To calculate reliable and reproducable Wannier functions, the random-factor in the rotation matrix has to be reduced. One approach is given by the *localization criterion* yielding *maximally-localized* Wannier functions [92]. Here, $U_{\mathbf{k}}^{nm}$ is chosen in such a way that the spread of the Wannier functions Ω is minimized:

$$\Omega = \sum_n \left[\langle \mathbf{0}n | r^2 | \mathbf{0}n \rangle - \langle \mathbf{0}n | \mathbf{r} | \mathbf{0}n \rangle^2 \right] \quad . \tag{2.1.27}$$

The sum is taken over the number of Wannier functions and $|\mathbf{0}n\rangle$ is the Dirac notation of the Wannier state $w_{\mathbf{0}n}(\mathbf{r})$.

The treatment of metals requires an adjustment for energy bands, which are attached to or mixed with other bands. Given a certain number of bands in an energy window, a disentanglement is used to separate these bands from the remaining ones and to form an optimally connected subspace [129]. Wihtin this subspace the MLWFs can be constructed as mentioned above.

After the construction of MLWFs, the e-ph matrix elements, can be transformed from the Bloch to the Wannier representation [43] via

$$g_{mn}^{\nu}(\mathbf{R}_e, \mathbf{R}_p) = \langle \mathbf{0}_e m | \delta_{\mathbf{R}_{p\nu}} \mathscr{V} | \mathbf{R}_e n \rangle = \frac{1}{N_p} \textstyle\sum_{\mathbf{k},\mathbf{q}} e^{-i(\mathbf{k}\cdot\mathbf{R}_e + \mathbf{q}\cdot\mathbf{R}_p)} (U_{\mathbf{k}+\mathbf{q}}^{nm})^{\dagger} g_{mn}^{\nu}(\mathbf{k}, \mathbf{q}) U_{\mathbf{k}}^{nm} (\mathbf{u}_{\mathbf{q}}^{\nu})^{-1} \quad , \tag{2.1.28}$$

with $\delta_{\mathbf{R}_{p\nu}} \mathscr{V}$ being the phonon perturbed potential in the Wannier representation. $\mathbf{R}_e$ and $\mathbf{R}_p$ are the lat-

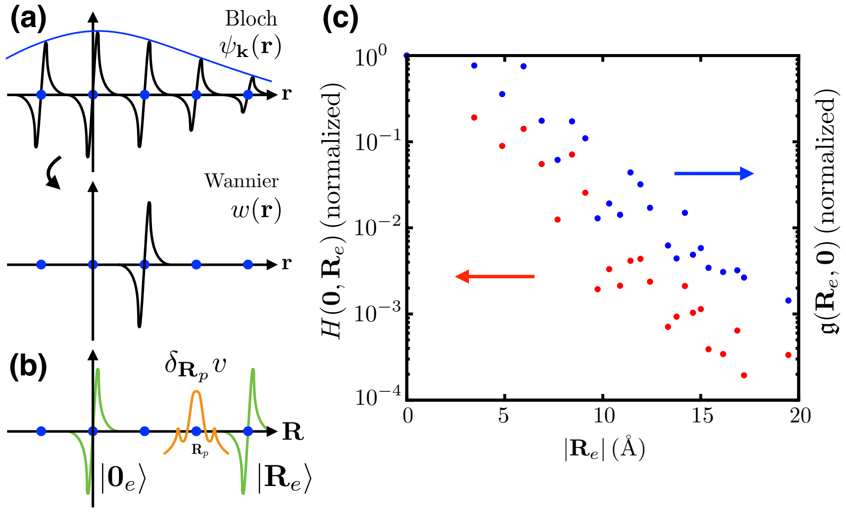

Figure 2.2.: Illustrations of certain properties ((a), (b)) in the Wannier representation (adopted from [92] and [43]). The blue points corresponds to the lattice vectors and the sketches are simplified to a 1D system. (a) Transformation from the extended wave function in the Bloch representation ($\psi_{\mathbf{k}}(\mathbf{r})$, top) to the localized Wannier function ($w(\mathbf{r})$, bottom) at a given wave vector $\mathbf{k}$ in a real-space representation. The blue line is the envelope $e^{i\mathbf{kr}}$ of the Bloch function. (b) The e-ph matrix element vanishes for the shown configuration of contributing electron Wannier functions (green) at lattice vectors $\mathbf{0}_e$ and $\mathbf{R}_e$ and phonon perturbation (orange) at $\mathbf{R}_p$ because two or more of these functions are centered on distant unit cells. (c) Spatial decay of the electronic Hamiltonian $H(\mathbf{0}, \mathbf{R}_e)$ and the e-ph matrix element $g(\mathbf{R}_e, \mathbf{0})$ in the Wannier representation for fcc Pb. Shown are the largest and normalized values with respect to Wannier function indices and unit cells at the same distance $|\mathbf{R}_e|$ as well as with respect to the ions in the unit cell and the cartesian directions in case of $g(\mathbf{R}_e, \mathbf{0})$. The corresponding Wannier functions were constructed with the adopted wannier90 [99] package inside the EPW [110] code and are used throughout this thesis.

tice vectors according to the electrons and ions and $\mathbf{u}_{\mathbf{q}}$ is the displacement field. In principal, equation 2.1.28 is simply a rotation of the ME in Bloch representation with $U_{\mathbf{k}}$, $U_{\mathbf{k}+\mathbf{q}}$ and the displacement field, followed by a Fourier transformation. More important is that $g^{\nu}_{mn}(\mathbf{R}_e, \mathbf{R}_p)$, whose calculation implements three points at $\mathbf{0}_e$, $\mathbf{R}_e$ and $\mathbf{R}_p$, vanishes whenever two of them correspond to sufficiently distant unit cells (see fig. 2.2(b)). Hence, the number of MEs in the Wannier representation, which actually has to be calculated, is quite small. Whether $g^{\nu}_{mn}(\mathbf{R}_e, \mathbf{R}_p)$ is zero or not, is roughly given by the overlap of the Wannier function at the three points, whose probability of presence decreases expontentially.

The electronic Hamiltonian in the Wannier representaion is given by

$$H^{nm}(\mathbf{R}_e, \mathbf{R}'_e) = \sum_{\mathbf{k}} e^{-i\mathbf{k}\cdot(\mathbf{R}'_e - \mathbf{R}_e)} (U^{nm}_{\mathbf{k}})^{\dagger} H^{nm}_{\mathbf{k}} U^{nm}_{\mathbf{k}} \quad . \tag{2.1.29}$$

Similiar to the vanishing MEs, $H^{nm}(\mathbf{R}_e, \mathbf{R}'_e)$ decays with the distance $|\mathbf{R}_e - \mathbf{R}'_e|$ as shown in figure 2.2(c) for Pb. The length scale of the decay is heavily influenced by the degree of localization of the constructed Wannier functions. Thus it can be treated as an additional quality feature of the MLWFs.

The dynamical matrix in the Wannier representation reads as

$$D^{\nu\mu}(\mathbf{R}_p, \mathbf{R}'_p) = \sum_{\mathbf{q}} e^{-i\mathbf{q}\cdot(\mathbf{R}'_p - \mathbf{R}_p)} e^{\nu\mu}_{\mathbf{q}} D^{\nu\mu}_{\mathbf{q}} (e^{\nu\mu}_{\mathbf{q}})^{\dagger} \quad , \tag{2.1.30}$$

where $D^{\nu\mu}_{\mathbf{q}}$ is the dynamical matrix in the Bloch representation and $e^{\nu\mu}_{\mathbf{q}}$ is a square matrix originating from the vibrational eigenmodes.

Finally, the inverse transformation of the e-ph matrix elements, the electronic Hamiltonian and the dynamical matrix, eq. 2.1.28-2.1.30, at new and particularly more electron and phonon momenta, $\mathbf{k}'$ and $\mathbf{q}'$, yields the basis for an computational accurate description of the e-ph interaction.

2.1.2. Interacting system

Self-energy including electron-phonon coupling

The physical meaning of the abstract concept of the self-energy can be described in the following way. Consider a non-interacting particle in a surrounding medium with a certain energy. If the particle now interacts with the medium, the energy of this particle will change due to changes in the environment, which are caused by the particle itself. This energy is called self-energy.

In general, the self-energy is a complex, non-hermitian, energy-dependent and non-local operator, which is calculated with the Green's functions or propagators of electrons and phonons. The relation between the electron self-energy Σ, the electron propagators of the the bare and interacting system (G_0, G) is given by the Dyson equation

$$G = G_0 + G_0 \Sigma G \quad , \tag{2.1.31}$$

which yields $\Sigma = G_0^{-1} - G^{-1}$. The same result is obtained for phonons, if one replaces Σ, G and G_0 by Π, D and D_0, where D and D_0 are the dressed and bare phonon propagators, respectively. If G and D would be known, the self-energies could be calculated exactly. Since this is not the case, the self-energies are usually written in terms of Feynman-diagrams (see fig. 2.3(a) and (b)) accounting explicitly for a certain interaction process. The number of diagrams is not limited and the exact self-energy would require a summation over infinite elements. Nevertheless, the contributions to Σ and Π can be orderd similarly to a perturbation series and higher order terms can be neglected in most situations since they are small compared to $\omega_{\mathrm{D}}/\epsilon_{\mathrm{F}}$. Here ω_{D} is a characteristic phonon frequency, which is usually the Debey frequency.

Considering only the first term in the electron self-energy, which is also called Fan self-energy [34,

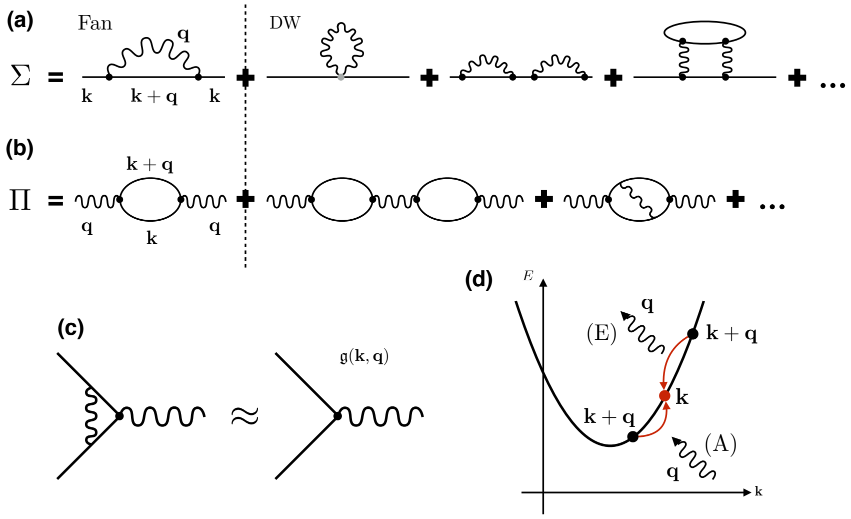

Figure 2.3.: (a), (b) Feynman diagrams contributing to the electron Σ and phonon self-energy Π. Only the lowest-order terms with respect to the atomic displacement are considered in the calculation (left from the dashed line). All other terms are of higher order (grey dot), multi-phonon processes or Vertex corrections and are therefore neglected. The first and second diagram in (a) are known as Fan self-energy in the Migdal approximation and Debye-Waller contribution to the self-energy, respectively. (c) Diagram of the screened electron-phonon vertex, which is approximated by the bare vertex $g(\mathbf{k}, \mathbf{q})$. (d) Sketch of the transition between the electron states $\mathbf{k}$ and $\mathbf{k} + \mathbf{q}$ via absorption (A) or emission (E) of a phonon $\mathbf{q}$ with energy $\hbar\omega_{\mathbf{q}}$.

35], and the first term in the phonon self-energy in figure 2.3(a), (b) one obtains [48, 87]

$$\Sigma(\mathbf{k},E) = \frac{i}{(2\pi)^4}\sum_{\nu}\int \mathrm{d}\Omega \int \mathrm{d}\mathbf{q}\left|g(\mathbf{k},\mathbf{q})\right|^2 D(\mathbf{q}\nu,\Omega)G_0(\mathbf{k}+\mathbf{q},E+\Omega) \tag{2.1.32}$$

$$\Pi(\mathbf{q}\nu,\Omega) = \frac{-2i}{(2\pi)^4}\int \mathrm{d}E \int \mathrm{d}\mathbf{k}\left|g(\mathbf{k},\mathbf{q})\right|^2 G_0(\mathbf{k},E)G_0(\mathbf{k}+\mathbf{q},E+\Omega) \tag{2.1.33}$$

The second term in the self-energy in fig. 2.3(a) is known as Debye-Waller (DW) term and is usually ignored in DFPT calculations, except for the YAMBO code [91]. This might be due to its complexity as well as to the evaluation of the self-energy. Expanding the total potential energy up to second-order in the displacement rather than expanding the Kohn-Sham potential, it is found that Σ^{DW} is of the same order as Σ^{Fan} and therefore equally important [2, 4, 23]. In metals, however, the approximation might be justified because Σ^{DW} is frequency-independent and might vary only slowly over the Fermi surface [42].

In an exact formulation of equation 2.1.32 and 2.1.33, all quantities have to be the dressed ones. Since this is quite complicated, one generally applies two major approximations, which are considered to be reasonable. First, the dressed matrix elements are approximated by the bare ones, which is known as Migdal approximation [98] (see fig. 2.3(c)). Additionally, the bare electron propagators are used to avoid self-consistency problems. The relevant bare and dressed electron and phonon propagators read as

$$G_0(\mathbf{k},E) = \frac{1}{E-\epsilon(\mathbf{k})} \quad , \tag{2.1.34}$$

$$G(\mathbf{k},E) = \frac{1}{E-\epsilon(\mathbf{k})-\Sigma(\mathbf{k},E)} \quad , \tag{2.1.35}$$

$$D(\mathbf{q}\nu,\Omega) = \frac{2\omega(\mathbf{q}\nu)}{\Omega^2-\omega(\mathbf{q}\nu)^2+i\delta} \quad . \tag{2.1.36}$$

The electron energy $\epsilon(\mathbf{k})$ is measured relative to the Fermi energy and the term $i\delta$ in eq. 2.1.36, with δ being a positive infinitesimal, replaces self-energy terms originating from phonon-phonon and electron-phonon interactions. Nevertheless, the fully renormalized phonon spectrum known from DFPT can be used in the phonon propagator [43, 55]. With eq. 2.1.34 and (2.1.36), the self-energies in eq. 2.1.32 and 2.1.33 can be analytically evaluated to

$$\Sigma(\mathbf{k},E) = \frac{1}{N_{\mathrm{q}}}\sum_{\mathrm{q}}\left|g(\mathbf{k},\mathbf{q})\right|^2\left[\frac{n(\omega_{\mathrm{q}})+1-f(\epsilon_{\mathrm{k+q}})}{E-\omega_{\mathrm{q}}-\epsilon_{\mathrm{k+q}}+i\delta}+\frac{n(\omega_{\mathrm{q}})+f(\epsilon_{\mathrm{k+q}})}{E+\omega_{\mathrm{q}}-\epsilon_{\mathrm{k+q}}+i\delta}\right] \quad , \tag{2.1.37}$$

$$\Pi(\mathbf{q},\omega) = \frac{2}{N_{\mathrm{k}}}\sum_{\mathrm{k}}\left|g(\mathbf{k},\mathbf{q})\right|^2\left[\frac{f(\epsilon_{\mathrm{k+q}})-f(\epsilon_{\mathrm{k}})}{\epsilon_{\mathrm{k+q}}-\epsilon_{\mathrm{k}}-\omega-i\eta}\right] \quad . \tag{2.1.38}$$

Here η is another positive infinitesimal, N_{q} and N_{k} are the number of $\mathbf{k}$ and $\mathbf{q}$ points, respectively, and $g(\mathbf{k},\mathbf{q})$ is the matrix element given in eq. 2.1.20. n and f are the Bose-Einstein and Fermi-Dirac distribution functions, in which the temperature dependence enters the self-energies. The band and mode indices of the electron and phonon states are omitted for simplicity. It is useful to rewrite the self-energies in terms of a real and an imaginary part. Then, the real part contributes to the renormalization of the bare energies while the imaginary part is related to the linewidth and a finite lifetime of the states due to the scattering of electrons by phonons or vice versa.

In the case of phonons the renormalization is already considered within DFPT and only the imaginary part is of interest. It reads in its general form

$$\Pi''_{\mathbf{q}}(\omega) = \frac{2}{N_{\mathbf{k}}} \sum_{\mathbf{k}} \left| g(\mathbf{k},\mathbf{q}) \right|^2 \left[f(\epsilon_{\mathbf{k}}) - f(\epsilon_{\mathbf{k+q}}) \delta(\omega_{\mathbf{q}} + \epsilon_{\mathbf{k}} - \epsilon_{\mathbf{k+q}}) \right] \tag{2.1.39}$$

and is directly related to the phonon linewidth $\gamma_{\mathbf{q}\nu} = 2\Pi''_{\mathbf{q}}(\omega\nu)$. However, in most first principles calculations the following expression, which was first derived by Allen [5], is used:

$$\gamma_{\mathbf{q}\nu} = 2\pi\omega_{\mathbf{q}} \sum_{\mathbf{q}} \left| g(\mathbf{k},\mathbf{q}) \right|^2 \delta(\epsilon_{\mathbf{k}} - \epsilon_{\mathrm{F}}) \delta(\epsilon_{\mathbf{k+q}} - \epsilon_{\mathrm{F}}) \quad . \tag{2.1.40}$$

One should keep in mind, that this formula is only valid for vanishing temperature ($T \longrightarrow 0$) or an T-independent linewidth. Calandra and Mauri [22] investigated the phonon linewidth of the E_{2g} mode in MgB_2 and compared $\gamma_{\mathbf{q}}$ given in eq. 2.1.39 with approximations due to the Allen formula and an approximation in which the phonon energy is considered in one δ-distribution function $\delta(\epsilon_{\mathbf{k+q}} - \epsilon_{\mathbf{k}n} - \epsilon_{\mathrm{F}} - \omega_{\mathbf{q}})$. They showed, that the neglection of the phonon energy in the Allen formula might lead to different results especially in the limit $|\mathbf{q}| \longrightarrow \Gamma$ and stated, that the magnitude of this effect strongly depends on the band structure around ϵ_{F} and the phonon frequency.

As mentioned above, equation 2.1.37 is usually written as $\Sigma = \Sigma' + i\Sigma''$, where Σ' is the real part of the electron self-energy and Σ'' is the imaginary part. The explicit expression of Σ' is not used in this work and therefore dropped here. Moreover, it can be calculated from the imaginary part using a Kramers-Kronig transformation as we will see in the next section. The imaginary part is related to the linewidth $\Gamma_{\mathbf{k}}$ and finite lifetime $\tau_{\mathbf{k}}$ of an electron, which is given by $\Gamma_{\mathbf{k}} = 2\Sigma''_{\mathbf{k}} = \hbar/\tau_{\mathbf{k}}$ with $\hbar$ being the reduced Planck constant and its detailed expression is

$$\Sigma''_{\mathbf{k}}(E) = \frac{1}{N_{\mathbf{q}}} \sum_{\mathbf{q}} \left| g(\mathbf{k},\mathbf{q}) \right|^2 \left[(1 - f(\epsilon_{\mathbf{k+q}}) + n(\omega_{\mathbf{q}}))\delta\left(E - \epsilon_{\mathbf{k+q}} - \omega_{\mathbf{q}}\right) + (f(\epsilon_{\mathbf{k+q}}) + n(\omega_{\mathbf{q}}))\delta\left(E - \epsilon_{\mathbf{k+q}} + \omega_{\mathbf{q}}\right) \right] . \tag{2.1.41}$$

The δ-functions ensure energy conservation in the scattering events. The first term corresponds to an absorption (A) process, where a phonon with the energy $\omega_{\mathbf{q}}$ is absorbed by an electron with the energy $\epsilon_{\mathbf{k+q}}$ yielding the new quasi-particle energy $E = \epsilon_{\mathbf{k+q}} + \omega_{\mathbf{q}}$ in the state $\mathbf{k}$. The second term is linked to the emission (E) of a phonon and the energy of the final state is $E = \epsilon_{\mathbf{k+q}} - \omega_{\mathbf{q}}$. A sketch of these processes is shown in figure 2.3(d). To rewrite eq. 2.1.41 in a more handy way, one generally introduces the Éliashberg spectral function . In principal, there is one for emission and one for absorption

$$\alpha^2 F^{\mathrm{E,A}}_{\mathbf{k}}(\epsilon,\omega) = \frac{1}{N_{\mathbf{q}}} \sum_{\mathbf{q}} \delta\left(\omega - \omega_{\mathbf{q}}\right) \left| g(\mathbf{k},\mathbf{q}) \right|^2 \delta\left(E - \epsilon_{\mathbf{k+q}} \pm \omega_{\mathbf{q}}\right) \tag{2.1.42}$$

but the difference between $\alpha^2 F^{\mathrm{A}}_{\mathbf{k}}(\epsilon,\omega)$ and $\alpha^2 F^{\mathrm{E}}_{\mathbf{k}}(\epsilon,\omega)$ is usually small and the *quasi-elastic assumption* can be applied, which leads to $\alpha^2 F^{\mathrm{E,A}}_{\mathbf{k}}(\epsilon,\omega) \approx \alpha^2 F_{\mathbf{k}}(\epsilon,\omega)$. Quasi-elastic means that all scattering processes take place only on the Fermi surface and the energy transfer arising from phonons is neglected. This seems reasonable because the phonon energy scale (meV) is typically much smaller than the electron energy scale (eV). Hence, the δ-functions reduce to

$$\delta\left(E - \epsilon_{\mathbf{k+q}} \pm \omega_{\mathbf{q}}\right) \approx \delta\left(E - \epsilon_{\mathbf{k+q}}\right) \quad . \tag{2.1.43}$$

and eq. (2.1.41) finally reads as

$$\Sigma''_{\mathbf{k}}(E) = \pi \int \mathrm{d}\omega\, \alpha^2 F_{\mathbf{k}}(\epsilon, \omega) \left[1 + 2n(\omega) + f(\epsilon_{\mathbf{k}} + \omega) - f(\epsilon_{\mathbf{k}} - \omega)\right] \quad . \tag{2.1.44}$$

Assuming that $\alpha^2 F_{\mathbf{k}}$ varies only slowly on the Fermi surface, the above equation can be simplified even further with the introduction of the Fermi surface-averaged Éliashberg spectral function

$$\alpha^2 F(\epsilon_{\mathrm{F}}, \omega) = \frac{1}{N_{\mathbf{q}} N_{\mathbf{k}} \mathcal{N}_{\epsilon_{\mathrm{F}}}} \sum_{\mathbf{q}} \delta\left(\omega - \omega_{\mathbf{q}}\right) \sum_{\mathbf{k}} \left|g(\mathbf{k}, \mathbf{q})\right|^2 \delta(\epsilon_{\mathbf{k}+\mathbf{q}} - \epsilon_{\mathrm{F}}) \delta(\epsilon_{\mathbf{k}} - \epsilon_{\mathrm{F}}) \quad , \tag{2.1.45}$$

which replaces the $\mathbf{k}$-dependent spectral function.

The electron-phonon coupling strength λ is generally calculated as [6]

$$\lambda = 2 \int_0^\infty \mathrm{d}\omega \, \frac{\alpha^2 F(\epsilon_{\mathrm{F}}, \omega)}{\omega} \quad , \tag{2.1.46}$$

which can be easily extended to a $\mathbf{k}$-dependent quantity using the $\mathbf{k}$-dependent Éliashberg spectral function . In a simple description λ forms the *mass enhancement factor* $(1 + \lambda)$, which is often found in standard textbooks to describe renormalization effects onto several physical properties.

One experimental access to the above mentioned quantities is given by *superconducting tunneling spectroscopy*, which enables the measurement of the Éliashberg spectral function and the calculation of the coupling strength [117, 136]. Another access is given by the spectral function $\mathscr{A}_{\mathbf{k}}(E, T)$, which can be obtained from *angle-resolved photoemission spectroscopy* (ARPES). The spectral function of an electron in state $\mathbf{k}$ includes the renormalization of the energies as well as the linewidth. The direct comparison with experiments needs further adjustments, which are discussed later in chapter 3.4. The spectral function itself is calculated as

$$\mathscr{A}_{\mathbf{k}}(E, T) = \frac{1}{\pi} \sum_n \frac{\left|\Sigma''_{\mathbf{k}n}(E, T)\right|}{\left[E - \epsilon_{\mathbf{k}n} - \Sigma'_{\mathbf{k}n}(E, T)\right]^2 + \Sigma''_{\mathbf{k}n}(E, T)^2} \quad . \tag{2.1.47}$$

$\mathscr{A}_{\mathbf{k}}$ is the analog to the band structure for the non-interacting electron in state $\mathbf{k}$ and band n. Although the band index is not a good quantum number of the interacting electron anymore, the spectral function of the total system is still written as a sum of spectral functions of each band according to

$$\mathscr{A}_{\mathbf{k}}(E, T) = \sum_n \mathscr{A}_{\mathbf{k}n}(E, T) \quad . \tag{2.1.48}$$

The discussion of transport properties will be in terms of a bandwise discussion relying on $\mathscr{A}_{\mathbf{k}n}$ instead of $\mathscr{A}_{\mathbf{k}}$. The reason is, that there exists no complete description based on Boltzmann theory to calculate transport properties directly from the total spectral function. Therefore, a detached investigation regarding the lifetime and the renormalization is the only way dealing with the electron-phonon interaction.

The poles in the spectral density in the limit of vanishing damping defines the renormalization condition of an electron state in the n-th band

$$E = \epsilon_{\mathbf{k}n} + \Sigma'_{\mathbf{k}}(E, T) \quad . \tag{2.1.49}$$

This equation has to be solved self-consistently due to the occurrence of the quasi-particle energy E on both sides.

Experimentally, the renormalized band structure is calculated via *momentum distribution curves* (MDC) and *energy distribution curves* (EDC), which are both obtained from a measured spectral function [26, 29]. Both methods are fits of the spectral function either at constant momentum (EDC) or at constant binding energy (MDC). The $\mathbf{k}$-dependent coupling strength is then calculated from the renormalized dispersion as

$$\lambda_{\mathbf{k}} = -\frac{\partial \Sigma'_{\mathbf{k}}(E)}{\partial E}\bigg|_{E=\epsilon_{\mathrm{F}}} \quad . \tag{2.1.50}$$

Kramers-Kronig Transformation

In the mathematical community, the Kramers-Kronig relation is known as Hilbert transform or Sokhotski-Plemelj theorem and was formulated more than one century ago. It is a powerful tool connecting the real and imaginary part of an arbitrary complex function χ, which fullfills the principle of causality. Thus it provides a large benefit in physics when dealing with response functions like dielectric functions and suszeptibilities. The relation was first used in the field of radiation and refraction by the name-giving physicists Kramers [73] and Kronig [75] in the late 20's.

According to the field of electron-phonon interaction, the Kramers-Kronig relations connect the real (Σ') and imaginary part (Σ'') of the complex electron self-energy $\Sigma = \Sigma' + i\Sigma''$, discussed in section 2.1.2, with the help of the Cauchy principal value $\mathscr{P}$ and are given by

$$\Sigma'(E) = \frac{1}{\pi}\mathscr{P}\int_{-\infty}^{+\infty} \mathrm{d}\omega\, \frac{\Sigma''(\omega)}{\omega - E} \quad \text{and} \tag{2.1.51}$$

$$\Sigma''(E) = -\frac{1}{\pi}\mathscr{P}\int_{-\infty}^{+\infty} \mathrm{d}\omega\, \frac{\Sigma'(\omega)}{\omega - E} \quad . \tag{2.1.52}$$

Hence, the above equations allow for a calculation of the total self-energy only by knowing either its real or imaginary part.

To ensure a numerically stable calculation it is useful to eliminate the poles in the denominators in equation 2.1.51 and 2.1.52 via an expansion with the term $(\omega + E)/(\omega + E)$ [78]. Considering the real part for instance and using the inherent odd symmetry, $\Sigma'(E) = -\Sigma'(-E)$, one obtains

$$\Sigma'(E) = \frac{2E}{\pi}\mathscr{P}\int_{0}^{\infty} \mathrm{d}\omega\, \frac{\Sigma''(\omega)}{\omega^2 - E^2} \quad . \tag{2.1.53}$$

In contrast to the real part, the imaginary part has an even symmetry, $\Sigma''(E) = \Sigma''(-E)$. An additional modification has to be applied in eq. 2.1.53 due to the non-vanishing imaginary part in the limit $|\omega| \longrightarrow \infty$. One simply adds $\mathscr{P}\int_{-\infty}^{\infty} \mathrm{d}\omega/(\omega - E) = 0$ yielding

$$\Sigma'(E) = \frac{2E}{\pi}\mathscr{P}\int_{0}^{\infty} \mathrm{d}\omega\, \frac{\Sigma''(\omega) - \Sigma''(E)}{\omega^2 - E^2} \quad , \tag{2.1.54}$$

which guarants a vanishing integrand for $|\omega| \longrightarrow \infty$. A comparison is shown in figure 2.4. The imaginary

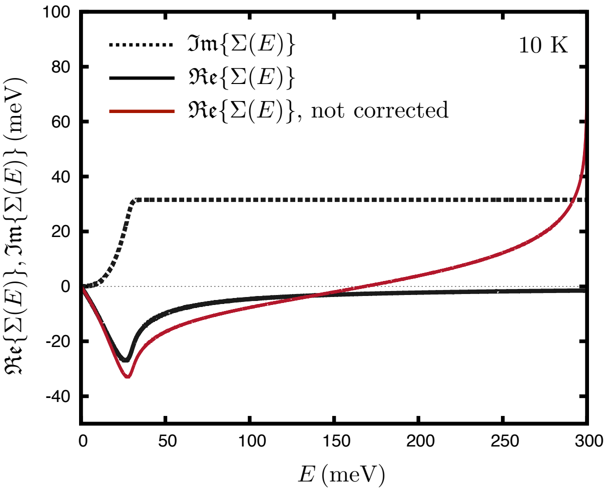

Figure 2.4.: Real part of the self-energy $Re\{\Sigma\}$ numerically evaluated with a Kramers-Kronig transformation. The corresponding imaginary part $Im\{\Sigma\}$ (dashed black line) is modeled with an isotropic Éliashberg spectral function for a Debye model. The parameters are $\omega_\mathrm{D} = 30\mathrm{meV}$, $\lambda = 1.0$ and $T = 10\mathrm{K}$. The straight-forwardly calculated real part (eq. (2.1.53)) is given by the solid red line. It diverges for large energies due to the non-vanishing integrand $Im\{\Sigma\}$ in the limit $E \longrightarrow 0$, which is not physical. The calculation with the modified transformation (eq. (2.1.54)) is shown as solid black line. Here, the real part goes to zero for energies far away from the inital energy of the electron state, which is given by $E = 0$ in this case.

part is calculated with eq. 2.1.44 and an isotropic Éliashberg spectral function for a 3D Debye model

$$\alpha^2 F_\mathrm{D}(E) = \begin{cases} \lambda \left(\frac{E}{\omega_\mathrm{D}}\right)^2 & , E \leq \omega_\mathrm{D} \\ 0 & , E > \omega_\mathrm{D} \quad . \end{cases} \tag{2.1.55}$$

The Debye frequency is $\omega_\mathrm{D} = 30\mathrm{meV}$, the coupling strength is set to $\lambda = 1.0$ and the temperature is $T = 10\mathrm{K}$.

Nesting function

The concept of nesting is more than 50 years old and strongly related to Kohn anomalies [71]. A Kohn anomaly is a singularity in the phonon dispersion of metals [28] or metallic systems [107]. More precisely, it is a significant reduction of the phonon frequencies and hence phonon energies $\omega_\mathbf{q}$ at a certain wave vector $\mathbf{q}$. Mathematically, its derivative has a discontinuity, $\left|\nabla_\mathbf{q}\omega_\mathbf{q}\right| = \infty$. Physically, the screening of the lattice vibrations of the ions by the electrons changes rapidly at this $\mathbf{q}$ point . The existence and peculiarity of a Kohn anomaly is determined by the Fermi surface of the electrons and described by the term nesting.

In a quasi-elastic description, nesting accounts for the connection of two points at the Fermi surface, $\mathbf{k}$ and $\mathbf{k}'$, via a phonon with wave vector $\mathbf{q}$ according to $\mathbf{k}' = \mathbf{k} + \mathbf{q} + \mathbf{G}$, where $\mathbf{G}$ is a reciprocal lattice vector. Hence, nesting is a purely geometrical property and does not depend on the phonon energy. Dropping the quasi-elastic assumption, a more general formulation requires the connection of $\mathbf{k}$ points with different energies, $\epsilon_\mathbf{k}$ and $\epsilon_{\mathbf{k}'}$, and therefore different iso-energy surfaces (IESs). Nevertheless, these IESs are almost identical in metals on the scale of phonon energies (meV) and the quasi-elastic assumption is justified.

A quantitativ measurement is the nesting function formulated by Kasinathan *et. al* [66, 67], which reads as

$$\xi_\mathbf{q} = \frac{1}{N_\mathbf{k}} \sum_\mathbf{k} \delta(\epsilon_{\mathbf{k}+\mathbf{q}} - \epsilon_\mathrm{F})\delta(\epsilon_\mathbf{k} - \epsilon_\mathrm{F}) \propto \oint \frac{\mathrm{d}L_\mathbf{k}}{\left|\mathbf{v}_\mathbf{k} \times \mathbf{v}_{\mathbf{k}+\mathbf{q}}\right|} \quad . \tag{2.1.56}$$

$\xi_\mathbf{q}$ is basically a line integral over shifted and intersected Fermi surfaces as shown in figure 2.5. To identify important nesting vectors one has to find parts at the Fermi surface, which are parallel orientated to each other. In that case a large number of electronic states are connected via a single phonon $\mathbf{q}^\mathrm{nest}$,

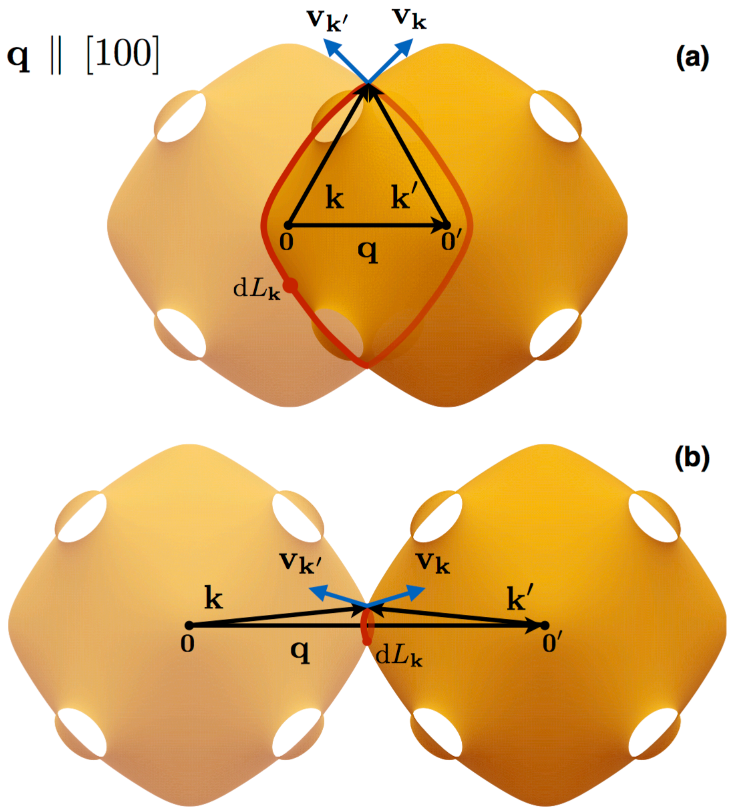
$\mathbf{q} \parallel [100]$
$\mathbf{v}_{\mathbf{k}'}$
$\mathbf{v}_{\mathbf{k}}$
(a)
$\mathbf{k}$
$\mathbf{k}'$
0
$\mathbf{q}$
0′
$\mathrm{d}L_{\mathbf{k}}$
(b)
$\mathbf{v}_{\mathbf{k}'}$
$\mathbf{v}_{\mathbf{k}}$
$\mathbf{k}$
$\mathbf{k}'$
0
$\mathbf{q}$
$\mathrm{d}L_{\mathbf{k}}$
0′

Figure 2.5.: Visualisation of eq. 2.1.56 to calculate the nesting function in the case of copper. The Fermi surface is shifted by $\mathbf{q}$ along the [100] direction. The intersecting line ($\mathrm{d}L_{\mathbf{k}}$) is shown in red and highlights all points on the Fermi surface, in which the electron states $\mathbf{k}$ and $\mathbf{k}' = \mathbf{k} + \mathbf{q}$ are connected by the phonon $\mathbf{q}$. The cross-product of the velocities $\mathbf{v}_{\mathbf{k}}$ and $\mathbf{v}_{\mathbf{k}'}$ in these points give rise to the nesting function $\xi_{\mathbf{q}}$. The contribution to $\xi_{\mathbf{q}}$ is small, when the velocities enclose a right angle (a) and large when they are almost parallel or antiparallel (b). The last one is an indicator for strong Fermi surface nesting, which might lead to Kohn anomalies.

which highly favours a Kohn anomaly at that wave vector. Making an explicit statement about the importance of $\mathbf{q}^{\text{nest}}$ in quantities related to electron-phonon interaction, like the phonon linewidth (eq. 2.1.40) or the Éliashberg spectral function (eq. 2.1.45), is usually not possible since the matrix element might suppress a large nesting contribution. At the same time, the coupling strength can increase the relevance of a phonon with an average nesting vector.

2.2. Boltzmann transport theory

The centerpiece of the Boltzmann transport theory is a balance equation of a single particle distribution function. The formalism is valid for charged particles, like electrons, as well as for charge-neutral particles, like phonons. It describes the diffusive transport regime, where the single scattering events of the particles are assumed to be independent from each other. Herefore the mean free path of the particles between two scattering events has to be larger than the average distance of two scatterers.

The theory provides a way to calculate macroscopic measurable observables based on the microscopic properties of the investigated system. It connects the motion of the particles due to external fields, like electric field or temperature gradient, with the scattering of the particles with its surrounding. While the motion is treated semiclassically, the scattering is directly obtained from a full quantum mechanical description.

The following chapter deals with the derivation of the linearised electron and phonon Boltzmann equation. The contribution of the electron-phonon interaction to both scattering terms is evaluated. Subsequently, the final expressions to calculate the electrical and thermal conductivity as well as the thermopower are given. The chapter closes with some thoughts about the solution of the coupled Boltzmann equations.

2.2.1. Boltzmann equation for electrons

Linearisation

The Boltzmann transport theory is based on a balance equation of the classical one-particle distribution function $f(\mathbf{k}, \mathbf{r}, t)$ of carriers, typically electrons. The latter depends on the quantum-mechanical state $\mathbf{k}$ as well as on the real space position $\mathbf{r}$ and the time t. In order to simplify the upcoming expressions, $\mathbf{k}$ is taken as a multi index, consisting of the wave vector $\mathbf{k}$, the spin σ and the band index n.

Within the semiclassical description, the distribution function has to be understood as a representation of an ensemble of electrons, which is confined in an infinitesimal phase space volume $^1\!/_{(2\pi)^3}\mathrm{d}\mathbf{k}\cdot\mathrm{d}\mathbf{r}$. Therefore and for simplicity, the distribution function is written as

$$f_{\mathbf{k}} \equiv f(\mathbf{k}, \mathbf{r}, t) \quad . \tag{2.2.1}$$

The integral over the first Brillouin zone (BZ) and the real space gives the total number of particles N

$$N = \int_{1.\mathrm{BZ}} \frac{\mathrm{d}\mathbf{k}\mathrm{d}\mathbf{r}}{(2\pi)^3} f(\mathbf{k}, \mathbf{r}, t) \quad . \tag{2.2.2}$$

The conservation of the particle number leads to the balance equation

$$\begin{aligned} \left(\frac{\partial f_{\mathbf{k}}}{\partial t}\right)\bigg|_{\text{scattering}} &= \frac{\partial f_{\mathbf{k}}}{\partial t} + \left(\frac{\partial f_{\mathbf{k}}}{\partial t}\right)\bigg|_{\text{drift}} = \frac{\partial f_{\mathbf{k}}}{\partial t} + \left(\frac{\partial f_{\mathbf{k}}}{\partial t}\right)\bigg|_{\text{diffusion}} + \left(\frac{\partial f_{\mathbf{k}}}{\partial t}\right)\bigg|_{\text{ext. fields}} \\ &= \frac{\partial f_{\mathbf{k}}}{\partial t} + \dot{\mathbf{r}}\frac{\partial f_{\mathbf{k}}}{\partial \mathbf{r}} + \dot{\mathbf{k}}\frac{\partial f_{\mathbf{k}}}{\partial \mathbf{k}} \quad . \end{aligned} \tag{2.2.3}$$

It describes the change of the distribution function due to an explicit time dependence of $f_{\mathbf{k}}$, the diffusion of electrons, the influence of external fields and scattering effects. The latter however, is counteracting the first three contributions resulting in a local equilibrium between the two competing parts

[96].

The time derivatives, $\dot{\mathbf{r}}$ and $\dot{\mathbf{k}}$, are given by the semiclassical equations of motion of an electron [143]

$$\frac{\mathrm{d}\mathbf{r}}{\mathrm{d}t} = \dot{\mathbf{r}} = \mathbf{v}_{\mathbf{k}} = \frac{1}{\hbar}\frac{\partial \epsilon_{\mathbf{k}}}{\partial \mathbf{k}} \quad , \tag{2.2.4}$$

$$\frac{\mathrm{d}\mathbf{k}}{\mathrm{d}t} = \dot{\mathbf{k}} = -\frac{|e|}{\hbar}\left(\mathbf{E}(\mathbf{r},t) + \frac{1}{c}\mathbf{v}_{\mathbf{k}} \times \mathbf{B}(\mathbf{r},t)\right) \quad . \tag{2.2.5}$$

Here, $\epsilon_{\mathbf{k}}$ is the energy eigenvalue of an electron with wave vector $\mathbf{k}$. The corresponding group velocity is denoted as $\mathbf{v}_{\mathbf{k}}$. $\mathbf{E}(\mathbf{r},t)$ and $\mathbf{B}(\mathbf{r},t)$ are the applied external electric and magnetic fields. Equation 2.2.3 is the electron Boltzmann equation in its general form. It is a non-linear integro-differential equation and usually not solvable without applying further approximations, especially for the scattering term. Nevertheless, an obtained solution for the electronic distribution function $f_{\mathbf{k}}$ provides all informations about the response of the electrons under the influence of diffusion and external fields.

In order to evaluate equation 2.2.3, we only consider a temperature gradient $\nabla T(\mathbf{r})$ and a time-independent electric field, while we neglect magnetic fields. The distribution function is time-independent as well. If the electric field is sufficiently small, we can assume that the perturbed system differs only slightly from its equilibrium state. Hence, it is reasonable to separate the distribution function $f_{\mathbf{k}}$ into its equilibrium part $f_{\mathbf{k}}^0$, which is given by the Fermi-Dirac distribution function, and a small deviation $\Delta f_{\mathbf{k}}$

$$f_{\mathbf{k}} = f_{\mathbf{k}}^0 + \Delta f_{\mathbf{k}} \quad , \quad f_{\mathbf{k}}^0 = \frac{1}{\mathrm{e}^{(\epsilon_{\mathbf{k}}-\mu)/k_{\mathrm{B}}T} + 1} \quad . \tag{2.2.6}$$

Including equation 2.2.4, 2.2.5 and 2.2.6 and assuming the distribution function to be homogenous, i.e. $\partial f_{\mathbf{k}}/\partial \mathbf{r} = 0$, the balance equation 2.2.3 reads as

$$\left(\frac{\partial f_{\mathbf{k}}}{\partial t}\right)\bigg|_{\text{scatt.}} = -\frac{\mathrm{d}f_{\mathbf{k}}^0}{\mathrm{d}\epsilon}\mathbf{v}_{\mathbf{k}}\left[(\epsilon_{\mathbf{k}} - \mu)\frac{1}{T}\nabla T + |e|\mathbf{E}\right] \quad . \tag{2.2.7}$$

Additionally, the emerging term $-(|e|/\hbar)(\partial \Delta f_{\mathbf{k}}/\partial \mathbf{k})\mathbf{E}$ is neglected since it is of higher order in the electric field. Equation 2.2.7 is the linearised Boltzmann equation with a general scattering term, which is also known as collision integral. Despite several typical types of scattering, like electron-electron, electron-impurity or electron-defect scattering, the interaction of electrons and phonons is of most interest in this thesis and therefore addressed in the next section.

Collision integral with electron-phonon interaction

Considering electron-phonon (e-ph) interaction, the scattering term in the Boltzmann equation 2.2.7 is given by

$$\begin{aligned}\frac{\partial f_{\mathbf{k}}}{\partial t}\bigg|_{\text{scatt.}} = \sum_{\mathbf{q}}\Bigg\{ & -\overbrace{\mathscr{P}_{\mathbf{kq}}^{\mathbf{k}'}[f_{\mathbf{k}}(1-f_{\mathbf{k}'})n_{\mathbf{q}}]}^{(i)} - \overbrace{\mathscr{P}_{\mathbf{k}}^{\mathbf{k}'\mathbf{q}}[f_{\mathbf{k}}(1-f_{\mathbf{k}'})(1+n_{\mathbf{q}})]}^{(iii)} \\ & + \underbrace{\mathscr{P}_{\mathbf{k}'}^{\mathbf{kq}}[(1-f_{\mathbf{k}})f_{\mathbf{k}'}(1+n_{\mathbf{q}})]}_{(ii)} + \underbrace{\mathscr{P}_{\mathbf{k}'\mathbf{q}}^{\mathbf{k}}[(1-f_{\mathbf{k}})f_{\mathbf{k}'}n_{\mathbf{q}}]}_{(iv)} \Bigg\} \quad .\end{aligned} \tag{2.2.8}$$

The band indices of the electronic states n,m and the mode index of the phonons ν are omitted for simplicity. The terms $f_{\mathbf{k}}$ and $(1 - f_{\mathbf{k}'})$ are related to the probabilty of the initial state $\mathbf{k}$ being occupied

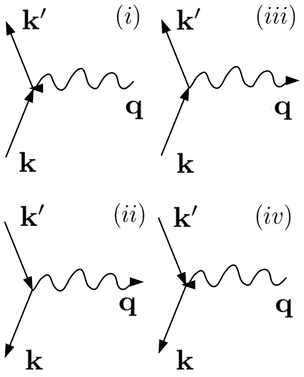

- (i) A: $\mathbf{k} \xrightarrow{\mathbf{q}} \mathbf{k}'$, $\mathbf{k}+\mathbf{q}=\mathbf{k}'$, $\epsilon_{\mathbf{k}} + \hbar\omega_{\mathbf{q}} = \epsilon_{\mathbf{k}'}$
- (ii) E: $\mathbf{k}' \xrightarrow{\mathbf{q}} \mathbf{k}$, $\mathbf{k}'-\mathbf{q}=\mathbf{k}$, $\epsilon_{\mathbf{k}'} - \hbar\omega_{\mathbf{q}} = \epsilon_{\mathbf{k}}$
- (iii) E: $\mathbf{k} \xrightarrow{\mathbf{q}} \mathbf{k}'$, $\mathbf{k}-\mathbf{q}=\mathbf{k}'$, $\epsilon_{\mathbf{k}} - \hbar\omega_{\mathbf{q}} = \epsilon_{\mathbf{k}'}$
- (iv) A: $\mathbf{k}' \xrightarrow{\mathbf{q}} \mathbf{k}$, $\mathbf{k}'+\mathbf{q}=\mathbf{k}$, $\epsilon_{\mathbf{k}'} + \hbar\omega_{\mathbf{q}} = \epsilon_{\mathbf{k}}$

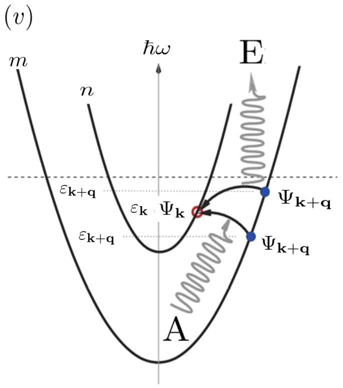

Figure 2.6.: (i)-(iv) The lowest order Feynman diagrams for scattering processes including electron-phonon interactions are shown on the left. The initial and final states are $\mathbf{k}$ and $\mathbf{k}' = \mathbf{k} \pm \mathbf{q}$. The corresponding momentum and energy relations as well as the distinction between absorption (A) and emission (E) process are given in the middle. (v) Adopted Sketch [59] of an absorption and emission process in a two-band picture for an initial $\Psi_{\mathbf{k}+\mathbf{q}}$ and a final state $\Psi_{\mathbf{k}}$ in bands m and n, respectively.

and to the final state $\mathbf{k}'$ being empty. Furthermore $n_{\mathbf{q}}$ and $(1+n_{\mathbf{q}})$ describe the absorption and emission process of a phonon, respectively.

The $\mathscr{P}$'s in eq. 2.2.8 are transition probabilities and correspond to different scattering processes for an electron from $\mathbf{k}$ into $\mathbf{k}'$ under the influence of a phonon $\mathbf{q}$. In lowest order of e-ph interaction, there are two absorption (A) and two emission (E) processes. An overview is given in figure 2.6. In all four transitions the crystal momentum and the energy are conserved. The transition probabilities are evaluated from *Fermi's golden rule* yielding

$$\mathscr{P}_{\mathbf{kq}}^{\mathbf{k}'} = \mathscr{P}_{\mathbf{k}'}^{\mathbf{kq}} = \mathscr{P}^{+} = \frac{2\pi}{\hbar} \left| g_{\mathbf{k},\mathbf{q}}^{\mathbf{k}'} \right|^2 \delta\left(\epsilon_{\mathbf{k}} - \epsilon_{\mathbf{k}+\mathbf{q}} + \omega_{\mathbf{q}}\right) \quad , \tag{2.2.9}$$

$$\mathscr{P}_{\mathbf{k}}^{\mathbf{k}'\mathbf{q}} = \mathscr{P}_{\mathbf{k}'\mathbf{q}}^{\mathbf{k}} = \mathscr{P}^{-} = \frac{2\pi}{\hbar} \left| g_{\mathbf{k}}^{\mathbf{k}',\mathbf{q}} \right|^2 \delta\left(\epsilon_{\mathbf{k}} - \epsilon_{\mathbf{k}+\mathbf{q}} - \omega_{\mathbf{q}}\right) \quad , \tag{2.2.10}$$

where the principle of microscopic reversibility was used in the first step. The matrix elements are calculated within DFPT as discussed in section 2.1.1. In greater detail they read as

$$g_{\mathbf{k},\mathbf{q}}^{\mathbf{k}'} = \left(\frac{\hbar}{2M\omega_{\mathbf{q}}}\right)^{1/2} \langle \Psi_{\mathbf{k}+\mathbf{q}} \left| \Delta V_{\mathbf{q}} \right| \Psi_{\mathbf{k}} \rangle \quad \text{with} \quad \Delta V_{\mathbf{q}} = \sum_{\mathbf{R},i} \frac{\partial V}{\partial \mathbf{u}_{\mathbf{R},i}} \cdot \mathbf{u}_{\mathbf{q},i} e^{i\mathbf{q}\mathbf{R}} \tag{2.2.11}$$

being the first-order derivative of the Kohn-Sham potential with respect to the atomic displacement $\mathbf{u}_{\mathbf{R},i}$ for the i-th atom.

The evaluation of the scattering term (eq. 2.2.8) requires knowledge about the actual distribution functions $f_{\mathbf{k}}$ and $n_{\mathbf{q}}$ including the consequences from the e-ph interaction. This treatment is related to the solution of the coupled Boltzmann equations for the electrons and phonons, which will be discussed more detailed in section 2.2.4.

Nevertheless, the electrons and phonons will be both described within a linear response formalism in a first step. This enables a derivation of the scattering term in a more general form, which can be easily simplified later on. The electron and phonon distribution functions read as

$$n_{\mathbf{q}} = n_{\mathbf{q}}^0 + \Delta n_{\mathbf{q}} \quad \text{and} \quad f_{\mathbf{k}} = f_{\mathbf{k}}^0 + \Delta f_{\mathbf{k}} \quad . \tag{2.2.12}$$

The electrons are treated in the same way as in section 2.2.1, while Δf_k is still a small deviation from the equilibrium Fermi-Dirac distribution function f^0_k. The phonons are described similarly with Δn_q being a small deviation from the equilibrium phonon distribution function

$$n^0_\mathrm{q} = \frac{1}{\mathrm{e}^{\hbar\omega_\mathrm{q}/k_\mathrm{B}T} - 1} \tag{2.2.13}$$

due to a thermal gradient. n^0_q is also known as Bose-Einstein distribution function.

Starting from eq. 2.2.8, using eq. 2.2.9, 2.2.10 and 2.2.12 and rearranging the resulting expressions with respect to the deviations Δf_k, $\Delta f_{\mathrm{k}'}$ and Δn_q, the scattering term is given by

$$\left.\frac{\partial f_\mathrm{k}}{\partial t}\right|_\mathrm{scatt.} = -\Bigg\{ \begin{aligned} & \Delta f_\mathrm{k} \sum_\mathrm{q} \left[\mathscr{P}^+(f^0_{\mathrm{k}'} + n^0_\mathrm{q}) + \mathscr{P}^-(1 + n^0_\mathrm{q} - f^0_{\mathrm{k}'})\right] \\ & - \sum_\mathrm{q} \Delta f_{\mathrm{k}'} \left[\mathscr{P}^+(1 + n^0_\mathrm{q} - f^0_\mathrm{k}) + \mathscr{P}^-(f^0_\mathrm{k} + n^0_\mathrm{q})\right] \\ & - \sum_\mathrm{q} \Delta n_\mathrm{q} \left[\mathscr{P}^+\left(f^0_{\mathrm{k}'} - f^0_\mathrm{k}\right) + \mathscr{P}^-\left(f^0_{\mathrm{k}'} - f^0_\mathrm{k}\right)\right] \end{aligned} \Bigg\} \; . \tag{2.2.14}$$

Higher order terms in the deviation functions, e.g. $\Delta f_\mathrm{k}\Delta f_{\mathrm{k}'}$ and $\Delta f_\mathrm{k}\Delta n_\mathrm{q}$, were neglected due to the linear response description. However, terms, which include the product $\Delta f_\mathrm{k}\Delta f_{\mathrm{k}'}\Delta n_\mathrm{q}$ cancel each other automatically.

To decouple and solve the electron Boltzmann equation independently one assumes the phonons to be in thermal equilibrium. This holds for sufficiently fast relaxations of excited phonons due to phonon-phonon or phonon-impurity scattering, which is known as *Born'sche Annahme*. Hence, $\Delta n_\mathrm{q} = 0$ and the last term in eq. 2.2.14 vanishes, which results in two contributions to the scattering term.

The first part describes scattering-out processes, particularly the transition from $\mathbf{k} \longrightarrow \mathbf{k}'$ under absorption or emission of a phonon. Thus, only the distribution function for an electron with wave vector $\mathbf{k}'$ appears. Furthermore, the first term leads to the *relaxation time approximation*, which will be discussed below. The second part accounts for the scattering-in processes from $\mathbf{k}' \longrightarrow \mathbf{k}$. The full solution of the independent electron Boltzmann equation, considering scattering-in and -out processes, can be achieved within an iterative scheme.

Another expression for the scattering term, which is often found in textbooks, is obatined by assuming the distribution functions n_q and f_k to be

$$n_\mathrm{q} = n^0_\mathrm{q} \quad \text{and} \quad f_\mathrm{k} = f^0_\mathrm{k} - \frac{\partial f^0_\mathrm{k}}{\partial \epsilon_\mathrm{k}} \phi_\mathrm{k} \tag{2.2.15}$$

with ϕ_k being the small deviation from the equilibrium distribution function. The final expression is then given by

$$\begin{aligned} \left.\frac{\partial f_\mathrm{k}}{\partial t}\right|_\mathrm{scatt.} &= -\sum_{\mathrm{k}'} \mathscr{W}(\mathbf{k},\mathbf{k}')\left[\phi_{\mathrm{k}'} - \phi_\mathrm{k}\right] \quad \text{with} \\ \mathscr{W}(\mathbf{k},\mathbf{k}') &= \frac{1}{k_\mathrm{B}T}\sum_\mathrm{q}\left\{\mathscr{P}^+ n^0_\mathrm{q}\left(1 - f^0_{\mathrm{k}'}\right) f^0_\mathrm{k} + \mathscr{P}^- n^0_\mathrm{q}\left(1 - f^0_\mathrm{k}\right) f^0_{\mathrm{k}'}\right\} \; , \end{aligned} \tag{2.2.16}$$

which is similar to the representation in Ziman's *Electrons and Phonons* [143] in eq. (9.5.1) for instance.

Nevertheless, equation 2.2.16 can be directly converted into 2.2.14 and vice versa.

Considering a small perturbation of an electric field $\mathbf{E}$ the response of the system can be assumed to be linear and the deviation $\Delta f_{\mathbf{k}}$ up to the first order in $\mathbf{E}$ reads as

$$\Delta f_{\mathbf{k}} = -|e| \frac{\partial f^0_{\mathbf{k}}}{\partial \epsilon_{\mathbf{k}}} \Lambda_{\mathbf{k}} \cdot \mathbf{E} \quad . \tag{2.2.17}$$

Here, $\Lambda_{\mathbf{k}}$ is the vector mean free path, which describes the linear change in the distribution function $f_{\mathbf{k}}$ in the presence of an electric field. The factor ${}^{\partial f^0_{\mathbf{k}}}/_{\partial \epsilon_{\mathbf{k}}}$ accounts for contributions to the transport exclusively from electrons nearby the Fermi energy.

Using eq. 2.2.7, 2.2.14 and 2.2.17 and applying the quasi-elastic assumption, the linearised Boltzmann equation with electron-phonon interaction is given by

$$\Lambda_{\mathbf{k}} = \tau_{\mathbf{k}} \left[\mathbf{v}_{\mathbf{k}} - \sum_{\mathbf{q}} \frac{\partial f^0_{\mathbf{k}'}}{\partial \epsilon_{\mathbf{k}'}} \left(\frac{\partial f^0_{\mathbf{k}}}{\partial \epsilon_{\mathbf{k}}} \right)^{-1} \Lambda_{\mathbf{k}'} \mathscr{P}^{\mathrm{qe}} (1 + 2n^0_{\mathbf{q}} + f^0(\epsilon_{\mathbf{k}} + \omega_{\mathbf{q}}) - f^0(\epsilon_{\mathbf{k}} + \omega_{\mathbf{q}})) \right] \quad , \tag{2.2.18}$$

where the transition probabilites of absorption and emission processes are considered to be equal

$$\mathscr{P}^{\mathrm{qe}} = \mathscr{P}^{+} = \mathscr{P}^{-} = \frac{2\pi}{\hbar} \left| g^{\mathbf{q}}_{\mathbf{k},\mathbf{k}+\mathbf{q}} \right|^2 \delta \left(\epsilon_{\mathbf{k}} - \epsilon_{\mathbf{k}+\mathbf{q}} \right) \quad . \tag{2.2.19}$$

The state-dependent relaxation time $\tau_{\mathbf{k}}$ was introduced as

$$(\tau_{\mathbf{k}})^{-1} = \sum_{\mathbf{q}} \mathscr{P}^{\mathrm{qe}} \left[1 + 2n^0_{\mathbf{q}} + f^0(\epsilon_{\mathbf{k}+\mathbf{q}} + \omega_{\mathbf{q}}) - f^0(\epsilon_{\mathbf{k}+\mathbf{q}} - \omega_{\mathbf{q}}) \right] \quad . \tag{2.2.20}$$

and is sometimes also called spectral relaxation time.

The exact solution of eq. 2.2.18 is given by an iterative scheme. In a first step, the vector mean free path is calculated without contributions from scattering-in processes yielding

$$\Lambda^{\mathrm{RTA}}_{\mathbf{k}} = \tau_{\mathbf{k}} \mathbf{v}_{\mathbf{k}} \quad , \tag{2.2.21}$$

which is known as relaxation time approximation (RTA). Usually the RTA is motivated in a different way stating that the perturbed steady-state distribution function will relax into its equilibrium distribution function when the external fields are switched off. Additionally, the relaxation is assumed to be driven by scattering processes only. Thus, the relaxation time $\tau_{\mathbf{k}}$ is introduced as an direct approximation of the collision integral in equation 2.2.7 given by

$$\left(\frac{\partial f_{\mathbf{k}}}{\partial t} \right) \Bigg|_{\text{scattering}} = -\frac{f_{\mathbf{k}} - f^0_{\mathbf{k}}}{\tau_{\mathbf{k}}} = -\frac{\Delta f_{\mathbf{k}}}{\tau_{\mathbf{k}}} \quad \text{with} \quad f_{\mathbf{k}}(t) = f^0_{\mathbf{k}} + \Delta f_{\mathbf{k}} \cdot \mathrm{e}^{-\frac{t}{\tau_{\mathbf{k}}}} \quad . \tag{2.2.22}$$

To continue with the iteration scheme, $\Lambda^{\mathrm{RTA}}_{\mathbf{k}}$ serves as input in the Boltzmann equation 2.2.18 and allows for a calculation of a vector mean free path $\Lambda^1_{\mathbf{k}}$, which then includes scattering-in processes. Subsequently, $\Lambda^2_{\mathbf{k}}$ is calculated with $\boxtimes^1_{\mathbf{k}}$ as a starting point. This procedure is repeated until $\left| \Lambda^i_{\mathbf{k}} - \Lambda^{i+1}_{\mathbf{k}} \right| \leq \varepsilon$ holds for the i-th iteration, where ε is a suitable cutoff. The calculation of the full, i.e. iterative, solution can be demanding if the Fermi surface is large and a lot of $\mathbf{k}$ points are required to evaluate the transport integrals, which are introduced in the next section.

To skip the iterative solution but keep information from the scattering-in processes, one generally introduces the transport relaxation time $\tau_{\mathbf{k}}^{\mathrm{tr}}$, which is often called the *momentum relaxation time approximation* (MRTA)

$$\begin{aligned}
\Lambda_{\mathbf{k}}^{\mathrm{MRTA}} &= \tau_{\mathbf{k}}^{\mathrm{tr}}\mathbf{v}_{\mathbf{k}} \quad , && (2.2.23)\\
\left(\tau_{\mathbf{k}}^{\mathrm{tr}}\right)^{-1} &= \sum_{\mathbf{q}} \mathscr{P}^{\mathrm{qe}}\left[1 + 2n_{\mathbf{q}}^{0} + f^{0}(\epsilon_{\mathbf{k+q}} + \omega_{\mathbf{q}}) - f^{0}(\epsilon_{\mathbf{k+q}} - \omega_{\mathbf{q}})\right]\left(1 - \frac{\mathbf{v}_{\mathbf{k}}\cdot\mathbf{v}_{\mathbf{k+q}}}{v_{\mathbf{k}}v_{\mathbf{k+q}}}\right) \quad . && (2.2.24)
\end{aligned}$$

Comparing with equation (2.2.20) one can see, that $\tau_{\mathbf{k}}^{\mathrm{tr}}$ is obtained by adding an additional term

$$\eta_{\mathbf{k}} = 1 - \frac{\mathbf{v}_{\mathbf{k}}\cdot\mathbf{v}_{\mathbf{k+q}}}{v_{\mathbf{k}}v_{\mathbf{k+q}}} \quad , \tag{2.2.25}$$

which accounts for the change in the direction of the velocity during the scattering process. The approximation of the full Boltzmann equation including the scattering-in term by the introduction of the transport relaxation time was supposed to be reasonable for quite some time. Recently, a quantitative investigation was made by Li [79]. He calculated the mobilities of the electrons in Si and $\mathrm{MoS_2}$ as well as the resistivity of Al within the RTA, MRTA and with the iterative solution of the Boltzmann equation. He showed, that all three solutions coincide for the two semiconductors. In the case of Al, however, only the MRTA agrees very well with the full solution. Nevertheless, both results may differ in other systems yielding a discrepancy even between the MRTA and the full solution.

2.2.2. Transport coefficients in the Boltzmann theory

The calculation of transport properties requires knowledge of the steady-state distribution function $f_{\mathbf{k}}$, which is accessible due to the perturbation of the equilibrium distribution function $f_{\mathbf{k}}^{0}$. Assuming the system to be perturbed by a weak electrical field, the deviation from $f_{\mathbf{k}}$ within the relaxation time approximation is given by equation 2.2.17 and 2.2.21. Rewriting $f_{\mathbf{k}}$ reveals, that the electric field linearly shifts the Fermi surface

$$f_{\mathbf{k}} = f_{\mathbf{k}}^{0} + \Delta f_{\mathbf{k}} = f_{\mathbf{k}}^{0} + |e|\tau_{\mathbf{k}}\mathbf{v}_{\mathbf{k}}\cdot\mathbf{E}\frac{\partial f_{\mathbf{k}}^{0}}{\partial\epsilon_{\mathbf{k}}} \approx f^{0}\left(\mathbf{k} + \frac{|e|\tau_{\mathbf{k}}}{\hbar}\mathbf{E}\right) \quad , \tag{2.2.26}$$

which leads to an asymmetric redistribution of populated states in the reciprocal space. In the simplest case, $\mathbf{E} = (E_{\mathrm{x}}, 0, 0)$, the Fermi surface seems to be shifted in $-\mathbf{k}$ direction and the net group velocity of the ensemble of electrons is distinct from zero. Hence, the electrical and heat current densities, $\mathbf{j}_{\mathrm{E}}$ and $\mathbf{j}_{\mathrm{Q}}$, caused solely by $\Delta f_{\mathbf{k}}$, are distinct from zero as well. Taking a temperature gradient into account and combining equation 2.2.7 and 2.2.22 to get an expression for $\Delta f_{\mathbf{k}}$, the current densities read as

$$\begin{aligned}
\mathbf{j}_{\mathrm{E}} &= -\frac{|e|}{(2\pi)^3}\int \mathrm{d}\mathbf{k}\,\mathbf{v}_{\mathbf{k}}\Delta f_{\mathbf{k}} = -\frac{|e|}{(2\pi)^3}\int \mathrm{d}\mathbf{k}\,\tau_{\mathbf{k}}\mathbf{v}_{\mathbf{k}}\circ\mathbf{v}_{\mathbf{k}}\frac{\partial f_{\mathbf{k}}^{0}}{\partial\epsilon}\left[(\epsilon_{\mathbf{k}} - \mu)\frac{1}{T}\nabla T + |e|\mathbf{E}\right] \quad \text{and} && (2.2.27)\\
\mathbf{j}_{\mathrm{Q}} &= \frac{1}{(2\pi)^3}\int \mathrm{d}\mathbf{k}\,\mathbf{v}_{\mathbf{k}}\left(\epsilon - \mu\right)\Delta f_{\mathbf{k}} = \frac{1}{(2\pi)^3}\int \mathrm{d}\mathbf{k}\,\tau_{\mathbf{k}}\mathbf{v}_{\mathbf{k}}\circ\mathbf{v}_{\mathbf{k}}\left(\epsilon - \mu\right)\frac{\partial f_{\mathbf{k}}^{0}}{\partial\epsilon}\left[(\epsilon_{\mathbf{k}} - \mu)\frac{1}{T}\nabla T + |e|\mathbf{E}\right] && (2.2.28)
\end{aligned}$$

To bring them into a more practical form, it is convenient to define the generalized transport coefficients or generalized conductance moments as

$$\underline{\underline{\mathscr{L}}}^{\alpha}(\mu, T) = \frac{1}{(2\pi)^3}\int \mathrm{d}\mathbf{k}\,\tau_{\mathbf{k}}\mathbf{v}_{\mathbf{k}}\circ\mathbf{v}_{\mathbf{k}}(\epsilon_{\mathbf{k}} - \mu)^{\alpha}\left(-\frac{\partial f_{\mathbf{k}}^{0}(\mu, T)}{\partial\epsilon}\right)_{\epsilon=\epsilon_{\mathbf{k}}} \quad , \tag{2.2.29}$$

where α denotes the order of the moment. The integration in the three dimensional $\mathbf{k}$-space is transformed via $\mathrm{d}\mathbf{k} = \mathrm{d}^2k\mathrm{d}k_\perp = \mathrm{d}S\mathrm{d}k_\perp = \mathrm{d}S\mathrm{d}\epsilon/\hbar|\mathbf{v_k}\backslash|$ into integrations over surfaces of constant energy. Following Mahan and Sofo [128], the *transport distribution function* (TDF) is introduced as

$$\underline{\underline{\Sigma}}(\epsilon) = \frac{1}{(2\pi)^3} \oint_{\epsilon=\epsilon_\mathbf{k}} \frac{\mathrm{d}S}{\hbar|\mathbf{v_k}|} \tau_\mathbf{k} \mathbf{v_k} \circ \mathbf{v_k} \quad , \tag{2.2.30}$$

which is the zeroth moment of the generalized transport coefficients at vanishing temperature, $\underline{\underline{\Sigma}}(\epsilon) = \underline{\underline{\mathscr{L}}}^0(\mu, 0)$. Since the difficult $\mathbf{k}$-space integration is hidden in the TDF, the integral in equation 2.2.29 reduces to a simple energy integration

$$\underline{\underline{\mathscr{L}}}^\alpha(\mu, T) = \int \mathrm{d}\epsilon\, \underline{\underline{\Sigma}}(\epsilon)(\epsilon_\mathbf{k} - \mu)^\alpha \left(-\frac{\partial f^0_\mathbf{k}(\mu, T)}{\partial \epsilon}\right) \quad . \tag{2.2.31}$$

The chemical potential μ is determined at a fixed temperature and charge carrier concentration N via an integration over the density of states $\mathcal{N}$. Assuming a semiconductor with a valence band maximum (VBM) and a conduction band minimum (CBM) it is

$$N = p + n = \int_{-\infty}^{\epsilon_\mathrm{VBM}} \mathrm{d}\epsilon\, \mathcal{N}(\epsilon)\left(1 - f^0_\mathbf{k}(\mu, T)\right) + \int_{\epsilon_\mathrm{CBM}}^{\infty} \mathrm{d}\epsilon\, \mathcal{N}(\epsilon) f^0_\mathbf{k}(\mu, T) \quad . \tag{2.2.32}$$

The two terms account for the hole and electron carrier concentration, p and n.

In general $\underline{\underline{\mathscr{L}}}^\alpha$ and $\underline{\underline{\Sigma}}$ are tensors. Nevertheless, there number of independent components is reduced due to crystal symmetry. In a cubic system for instance it holds $\mathscr{L}^\alpha_{ij}(\mu, T) = \mathscr{L}^\alpha(\mu, T)\delta_{ij}$, where only one independent component remains.

Finally, equation 2.2.27 and 2.2.28 can be rewritten in terms of $\mathscr{L}^\alpha$ to highlight the relations between the generalized fluxes, $\mathbf{j_E}$ and $\mathbf{j_Q}$, and the generalized forces $\mathbf{E}$ and ∇T

$$\mathbf{j_E} = e^2\mathscr{L}^0\mathbf{E} - \frac{e}{T}\mathscr{L}^1\nabla T \tag{2.2.33}$$

$$\mathbf{j_Q} = e\mathscr{L}^1\mathbf{E} - \frac{1}{T}\mathscr{L}^2\nabla T \quad . \tag{2.2.34}$$

Here, it is already seen that the two fluxes are coupled by the same generalized conductance moment $\mathscr{L}^1$. Since $\mathscr{L}^1$ and the other generalized conductance moments obey only a mathematical character, a physical interpretation of the coupling is missing. Fortunately, the relation between $\mathbf{j_E}$ and $\mathbf{j_Q}$ can be also expressed in terms of measurable observables, which gives insights in the physical picture. The transport properties itselves are then given by combinations of the different generalized transport coefficients.

Assuming a constant temperature, the electrical conductivity σ is obtained from eq. 2.2.33 and the comparison with Ohm's law

$$\mathbf{j_E} = \sigma\mathbf{E} \quad \text{with} \quad \sigma = e^2\mathscr{L}^0 \tag{2.2.35}$$

being directly proportional to $\mathscr{L}^0$. The electrical resistivity is given by the inverse quantitiy, $\rho = \sigma^{-1}$.

The second decoupled transport property is the electronic part of the thermal conductivity κ_el. In an open electrical circuit, i.e. $\mathbf{j_E} = 0$, eq. 2.2.34 reads as

$$\mathbf{j_Q} = -\kappa_\mathrm{el}\nabla T \quad \text{with} \quad \kappa_\mathrm{el} = \frac{1}{T}\left(\mathscr{L}^2 - \left(\mathscr{L}^1\right)^2\left(\mathscr{L}^0\right)^{-1}\right) \tag{2.2.36}$$

being obtained from the comparison with Fourier's law. The remaining part from the phonons, named lattice thermal conductivity κ_{ph}, can be calculated from the Peierls-Boltzmann equation for phonons, which is the equivalent to the Boltzmann equation for electrons. The total thermal conductivity is then given by the sum of both contributions.

Considering an electrical open circuit, the electric field is coupled to the temperature gradient

$$\mathbf{E} = S\nabla T \quad \text{by} \quad S = \frac{1}{eT}\mathscr{L}^1\left(\mathscr{L}^0\right)^{-1} \quad , \tag{2.2.37}$$

which is the thermopower or Seebeck coefficient first introduced by Seebeck [119].

The thermopower shown above originates only from the diffusion of electrons and is therefore also known as diffusive thermopower S^{d}. The actual calculation of S^{d} is performed within several simplifications, which may significantly affect the result. One can simply apply the *constant* relaxation time approximation (cRTA) given by $\Lambda_{\mathbf{k}}^{\mathrm{cRTA}} = \tau\mathbf{v}_{\mathbf{k}}$. This, however, results in a thermopower, which is solely obtained from electronic band structure effects. Considering a **k**-dependent or at least an energy-dependent relaxation time, includes explicitly the interaction of electrons and phonons in addition to band structure effects. Up to now, the phonons were assumed to be in thermal equilibrium according to eq. 2.2.13. Dropping this assumption and describing the phonons as perturbed by the electrons give rise to a second contribution to the thermopower, which is historically named phonon-drag thermopower S^{phd}. An expression for the latter can be derived while solving the coupled electron and phonon Boltzmann equations as we will see in section 2.2.4.

2.2.3. Boltzmann equation for phonons with electron-phonon interaction

The structure of the phonon Boltzmann equation, which is also known as Peierls-Boltzmann equation, is similar to the electron Boltzmann equation. The balance equation for the phonon distribution function n_{q} is given by

$$\left(\frac{\partial n_{\mathrm{q}}}{\partial t}\right)\bigg|_{\mathrm{drift}} = \left(\frac{\partial n_{\mathrm{q}}}{\partial t}\right)\bigg|_{\mathrm{scattering}} \quad , \tag{2.2.38}$$

where the drift term depends only on a thermal gradient

$$\left(\frac{\partial n_{\mathrm{q}}}{\partial t}\right)\bigg|_{\mathrm{drift}} = -\mathbf{v}_{\mathrm{q}}\frac{\partial n_{\mathrm{q}}}{\partial \mathbf{r}} = -\mathbf{v}_{\mathrm{q}}\frac{\partial n_{\mathrm{q}}}{\partial T}\nabla T = -\mathbf{v}_{\mathrm{q}}\hbar\omega_{\mathrm{q}}\left(-\frac{\partial n_{\mathrm{q}}}{\partial \omega_{\mathrm{q}}}\right)\frac{1}{T}\nabla T \quad . \tag{2.2.39}$$

The electron-phonon contribution to the scattering term in its general form reads as

$$\begin{aligned}\frac{\partial n_{\mathrm{q}}}{\partial t}\bigg|_{\mathrm{scatt.}} = \frac{1}{2}\sum_{\mathbf{k}}\bigg\{ \quad & -\mathscr{P}^{+}[n_{\mathrm{q}}f_{\mathbf{k}}(1-f_{\mathbf{k}'})] + \mathscr{P}^{+}[(1+n_{\mathrm{q}})(1-f_{\mathbf{k}})f_{\mathbf{k}'}] \\ & +\mathscr{P}^{-}[(1+n_{\mathrm{q}})f_{\mathbf{k}}(1-f_{\mathbf{k}'})] - \mathscr{P}^{-}[n_{\mathrm{q}}(1-f_{\mathbf{k}})f_{\mathbf{k}'}] \quad \bigg\} \quad .\end{aligned} \tag{2.2.40}$$

Comparing with eq. 2.2.8 shows slightly different signs for the four terms. Here, the distinction is related to absorption (n_{q}, -) and emission ($1+n_{\mathrm{q}}$, +) processes, while in the electronic case it is related to the occupation of the initial states. The additional factor ½ prevents double counting of the transitions $\mathbf{k} \longrightarrow \mathbf{k}'$ and $\mathbf{k}' \longrightarrow \mathbf{k}$, while summing up over the phonon wave vector **q**. The transition probabilities are already given by eq. 2.2.9 and 2.2.10 and are the same in both equations. With the ansatz from eq.

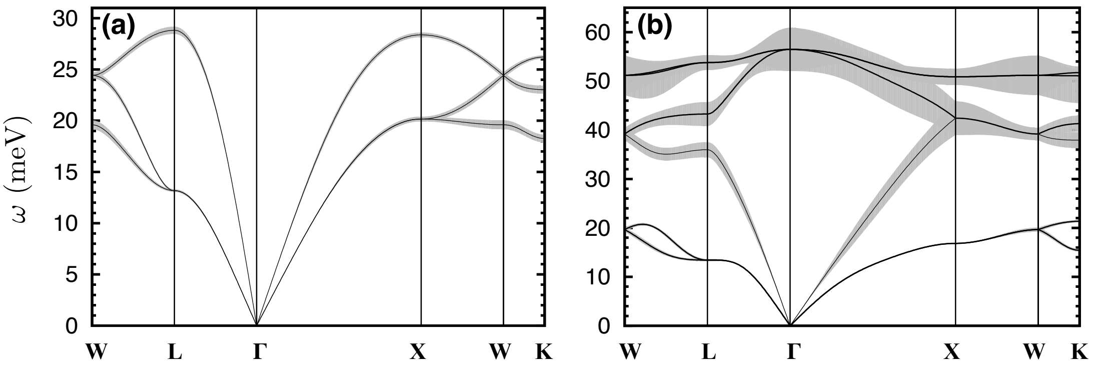

Figure 2.7.: Phonon frequency spectrum of Cu (a) and Si (b) with superimposed phonon linewidths γ_{q} due to electron-phonon coupling. The largest value in copper is 0.015meV while it is 0.37meV in silicon.

2.2.12, the scattering term can be evaluated into a similar form compared to eq. 2.2.14

$$\begin{aligned}\left.\frac{\partial n_{\mathrm{q}}}{\partial t}\right|_{\text{scattering}} = \quad & \frac{1}{2}\sum_{\mathbf{k}}\Big\{\Delta f_{\mathrm{k}}\left[-\mathscr{P}^{+}\left(n_{\mathrm{q}}^{0}+f_{\mathrm{k'}}^{0}\right)+\mathscr{P}^{-}\left(1+n_{\mathrm{q}}^{0}-f_{\mathrm{k'}}^{0}\right)\right] \\ & \qquad +\Delta f_{\mathrm{k'}}\left[\left(\mathscr{P}^{+}(1+n_{\mathrm{q}}^{0}-f_{\mathrm{k}}^{0}\right)-\mathscr{P}^{-}\left(n_{\mathrm{q}}^{0}+f_{\mathrm{k}}^{0}\right)\right]\Big\} \\ & -\frac{1}{2}\Big\{\sum_{\mathbf{k}}\left[\mathscr{P}^{+}\left(f_{\mathrm{k'}}^{0}-f_{\mathrm{k}}^{0}\right)-\mathscr{P}^{-}\left(f_{\mathrm{k'}}^{0}-f_{\mathrm{k}}^{0}\right)\right]\Big\}\cdot\Delta n_{\mathrm{q}} \quad .\end{aligned} \tag{2.2.41}$$

Assuming the electrons to be in equilibrium, i.e. $\Delta f_{\mathrm{k}} = 0$ and $\Delta f_{\mathrm{k'}} = 0$, leads to the relaxation time approximation for phonons

$$\Delta n_{\mathrm{q}} = \hbar\omega_{\mathrm{q}}\tau_{\mathrm{q}}\mathbf{v}_{\mathrm{q}}\frac{\partial n_{\mathrm{q}}}{\partial\omega_{\mathrm{q}}}\frac{1}{T}\nabla T \quad . \tag{2.2.42}$$

with the relaxation time given by

$$\left(\tau_{\mathrm{q}}\right)^{-1} = \frac{1}{2}\sum_{\mathbf{k}}\left[\mathscr{P}^{+}\left(f_{\mathrm{k'}}^{0}-f_{\mathrm{k}}^{0}\right)-\mathscr{P}^{-}\left(f_{\mathrm{k'}}^{0}-f_{\mathrm{k}}^{0}\right)\right] \quad . \tag{2.2.43}$$

As in the description of electrons, the phonon relaxation time is also related to a phonon linewidth via $\gamma_{\mathrm{q}} = \hbar/\tau_{\mathrm{q}}$. It is shown superimposed onto the phonon frequency spectrum of Cu and Si in figure 2.7(a) and (b), respectively.

Conclusively, the electron-phonon contribution to the lattice thermal conductivity can be obatined from Δn_{q}.

2.2.4. Coupled electron and phonon Boltzmann equations

The terms in the phonon Boltzmann equation (phBE) (eq. 2.2.41), which include Δf_{k} and $\Delta f_{\mathrm{k'}}$, and the terms in the electron Boltzmann equation (elBE) (eq. 2.2.14) including Δn_{q} reveals the coupling of both equations. A full solution for the electron and phonon distribution functions requires an iterative procedure, which becomes rapidly very demanding as we will see later on.

In a first step, one can solve the elBE, where the phonons are treated within the RTA involving $\Delta f_{\mathrm{k}} = 0$ and $\Delta f_{\mathrm{k'}} = 0$ in eq. (2.2.41). The same approach can be used vice versa for the phBE with $\Delta f_{\mathrm{k'}} = 0$ and $\Delta n_{\mathrm{q}} = 0$ in eq. 2.2.14. Each solution provides an additional contribution to either the electrical or thermal conductivity, which leads to the phonon-drag thermopower S^{phd} and Peltier coefficient Π.

First ideas concerning the phonon-drag effect were formulated by Gurevich in the mid 40's [51, 52] and after that the effect was studied by many other authors, experimentalists or theoreticians, either way. One group, starting with Herring in 1954 [58], dealt with the Peltier effect and the influence of phonon-drag onto semiconductors. The other one around Gurevich, Cantrell, MacDonald, Ziman, Grimvall and others developed a theory based on the Seebeck effect and investigated metals [24, 48, 53, 143].

The simple physical picture of the phonon-drag is that during the scattering event, the non-equilibrium phonons transfer a part of their momentum to the electrons, which causes an additional electrical current. This will be called the Seebeck picture because the inverse argumentation (Peltier picture) is valid as well, which implies that the non-equilibrium electrons drag the phonons for an additional thermal current. Nevertheless, both are connected via the Kelvin relation $\Pi = S^{\mathrm{phd}} T$.

To be more precise, one follows the Seebeck picture and evaluates the elBE according to eq. 2.2.3, 2.2.7 and 2.2.14. For simplicity the final electron states are assumed to be in equilibrium $\Delta f_{\mathbf{k}'} = 0$. As mentioned above, $\Delta n_{\mathbf{q}}$ is taken from the phBE in relaxation time approximation (eq. 2.2.42). After some lenghty calculations one ends up with the total thermopower $S = S^{\mathrm{d}} + S^{\mathrm{phd}}$ with S^{d} from eq. 2.2.37 and the phonon-drag contribution

$$S^{\mathrm{phd}} = \frac{|e|}{\sigma V} \frac{1}{k_{\mathrm{B}} T^2} \sum_{\mathbf{k},\mathbf{q}} \hbar\omega_{\mathbf{q}} \tau_{\mathbf{q}} \mathbf{v}_{\mathbf{q}} \mathscr{P}^{+} f_{\mathbf{k}}^{0} \left(1 - f_{\mathbf{k}'}^{0}\right) n_{\mathbf{q}}^{0} \left(\tau_{\mathbf{k}} \mathbf{v}_{\mathbf{k}} - \tau_{\mathbf{k}'} \mathbf{v}_{\mathbf{k}'}\right) \quad , \tag{2.2.44}$$

which originates only from non-equilibrium phonons. In absolute values, this contribution is usually relatively small in metals but can be huge in low-doped semiconductors [15, 37, 88, 133].

Besides the increased thermopower, which is the most prominent feature of the phonon-drag effect, a correction to the electrical conductivity emerges as well [61, 143]

$$\sigma = \left(\rho^0 - \rho^{\mathrm{phd}}\right)^{-1} \quad \text{with} \quad \rho^{\mathrm{phd}} = \frac{\left(S^{\mathrm{phd}}\right)^2 T}{\kappa_{\mathrm{ph}}} \quad . \tag{2.2.45}$$

However, this is only a second order effect, which means that the electron current causes a current in the phonons, which subsequently acts back upon the electrons. Huebener already reported in the 60's that σ^{phd} is at least a factor of 10^3 smaller than the electrical conductivity $\sigma^0 = \left(\rho^0\right)^{-1}$, where no electron-phonon interaction was taken into account [61]. Although it is an effect of second order, this does not seem to be a general statement and is discussed since the 60's [19, 108, 121].

Following the Peltier picture and assuming isothermal conditions, the deviation from the phonon distribution function is obtained via eq. 2.2.39, 2.2.41 and 2.2.17 and reads as

$$\Delta n_{\mathbf{q}} = \frac{|e|}{2} \tau_{\mathbf{q}} \left\{ \sum_{\mathbf{k}} \tau_{\mathbf{k}} \mathbf{v}_{\mathbf{k}} \frac{\partial f_{\mathbf{k}}^{0}}{\partial \epsilon_{\mathbf{k}}} \left[-\mathscr{P}^{+} \left(n_{\mathbf{q}}^{0} + f_{\mathbf{k}'}^{0}\right) + \mathscr{P}^{-} \left(1 + n_{\mathbf{q}}^{0} - f_{\mathbf{k}'}^{0}\right) \right] \right\} \cdot \mathbf{E} \quad . \tag{2.2.46}$$

The additional thermal current is then given by

$$\mathbf{j}_{\mathrm{Q}} = \frac{1}{V} \sum_{\mathbf{q}} \hbar\omega_{\mathbf{q}} \mathbf{v}_{\mathbf{q}} \Delta n_{\mathbf{q}} \equiv \Pi \mathbf{j}_{\mathrm{E}} = \Pi \sigma \mathbf{E} \quad , \tag{2.2.47}$$

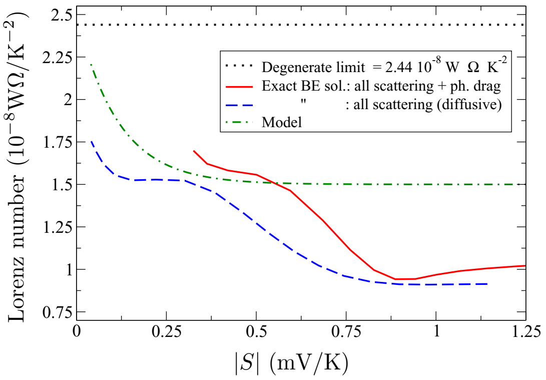

Figure 2.8.: Lorenz number L as a function of the thermopower at 300K in n-doped silicon. The calculation includes electron-phonon and electron-impurity scattering. Noticeable differences compared to the Wiedemann-Franz law (black dotted line) occur for both solutions of the Boltzmann equation, whether the phonon-drag effect is accounted for or not (solid red and dashed blue line, respectively). The graph was taken from Fiorentini *et. al* [37] and the model function (green line) is described in Ref. [69].

which leads to the Peltier coefficient written in a symmetric form

$$\Pi = \frac{|e|}{\sigma V}\frac{1}{k_\mathrm{B}T}\sum_{\mathbf{k},\mathbf{q}} \hbar\omega_\mathbf{q}\tau_\mathbf{q}\mathbf{v}_\mathbf{q}\mathscr{P}^+ f^0_\mathbf{k}\left(1-f^0_{\mathbf{k}'}\right) n^0_\mathbf{q}\left(\tau_\mathbf{k}\mathbf{v}_\mathbf{k}-\tau_{\mathbf{k}'}\mathbf{v}_{\mathbf{k}'}\right) \quad . \tag{2.2.48}$$

The comparison with S^{phd} from eq. (2.2.44) according to the Kelvin relation shows that both pictures, Seebeck and Peltier, are equivalent to each other.

Apart from the influence onto the elctrical conductivity and thermopower, the impact of the phonon-drag effect can be also seen in the Lorenz number $L = {}^{\varkappa_\mathrm{el}}/_{\sigma T}$. Fiorentini *et. al* [37] showed, that in n-doped silicon L varies with respect to the thermopower and differs noticeably from the degenerate limit of the Wiedemann-Franz law (fig. 2.8). They say, that the reason is given by the electronic part of the thermal conductivity $\varkappa_\mathrm{el}$ due to its sensitivity of certain terms, i.e. $(\epsilon-\mu)^2$, while solving the Boltzmann equation. Nevertheless, solving the Boltzmann equation without the phonon-drag contribution leads qualitatively to the same result, which can be seen by comparison of the solid red and the dashed blue line. Hence, the influence due to electron-phonon interaction onto transport properties can be rather large even though the calculation does not account for the phonon-drag effect.

To close this section, an iterative scheme to solve the coupled Boltzmann equations self-consistently is presented. To enable a compact formulation, the independent solutions of both Boltzmann equations within the RTA are rewritten as

$$\Delta f^{(1)}_\mathbf{k} = \frac{\partial f^0_\mathbf{k}}{\partial\epsilon_\mathbf{k}}\tau_\mathbf{k}\mathbf{v}_\mathbf{k}\left[(\epsilon_\mathbf{k}-\mu)\frac{1}{T}\nabla T + |e|\mathbf{E}\right] = X^{(1)}_\mathbf{k}\nabla T + Y^{(1)}_\mathbf{k}\mathbf{E} \tag{2.2.49}$$

$$\Delta n^{(1)}_\mathbf{q} = \frac{\partial n_\mathbf{q}}{\partial\omega_\mathbf{q}}\tau_\mathbf{q}\mathbf{v}_\mathbf{q}\hbar\omega_\mathbf{q}\frac{1}{T}\nabla T = \tilde{Z}^{(1)}_\mathbf{q}\nabla T \tag{2.2.50}$$

The general solutions up to the j-th order in electron and phonon contributions is then given by

$$\Delta f^{(j)}_\mathbf{k} = \sum_{i=1}^{j} X^{(i)}_\mathbf{k}\nabla T + Y^{(i)}_\mathbf{k}\mathbf{E} + Z^{(i)}_\mathbf{k}\nabla T \tag{2.2.51}$$

$$\Delta n^{(j)}_\mathbf{q} = \sum_{i=1}^{j} \tilde{Z}^{(i)}_\mathbf{q}\nabla T + \tilde{X}^{(i)}_\mathbf{q}\nabla T + \tilde{Y}^{(i)}_\mathbf{q}\mathbf{E} \quad . \tag{2.2.52}$$

Note that the first-order in $\Delta f^{(j)}_\mathbf{k}$ is always a sum of the independent solution of the elBE and the first correction coming from the phBE and vice versa. These first-order terms cause the above derived phonon-drag thermopower and Peltier coefficient. The **k**- and **q**-dependent coefficients in eq. (2.2.51) and (2.2.52) are given by the following iteration scheme:

$$\begin{aligned} X_{\mathbf{k}}^{(i+1)} &= \Xi_{\mathbf{k}}\Xi_{\mathbf{q}}X_{\mathbf{k}}^{(i)}, & \tilde{X}_{\mathbf{q}}^{(i)} &= \Xi_{\mathbf{q}}X_{\mathbf{k}}^{(i)}, \\ Y_{\mathbf{k}}^{(i+1)} &= \Xi_{\mathbf{k}}\Xi_{\mathbf{q}}Y_{\mathbf{k}}^{(i)}, & \tilde{Y}_{\mathbf{q}}^{(i)} &= \Xi_{\mathbf{q}}Y_{\mathbf{k}}^{(i)}, \\ Z_{\mathbf{k}}^{(i)} &= \Xi_{\mathbf{q}}\tilde{Z}_{\mathbf{q}}^{(i)}, & \tilde{Z}_{\mathbf{q}}^{(i+1)} &= \Xi_{\mathbf{q}}\Xi_{\mathbf{k}}\tilde{Z}_{\mathbf{q}}^{(i)}, \\ i &\geq 1, & i &\geq 1. \end{aligned} \tag{2.2.53}$$

The connecting quantities $\Xi_{\mathbf{k}}$ and $\Xi_{\mathbf{q}}$ are sums over phonon or electron wave vectors, respectively.

$$\begin{aligned} \Xi_{\mathbf{k}} &= \tau_{\mathbf{k}} \sum_{\mathbf{q}} \left[\mathscr{P}^{+}\left(f_{\mathbf{k}'}^{0} - f_{\mathbf{k}}^{0}\right) - \mathscr{P}^{-}\left(f_{\mathbf{k}'}^{0} - f_{\mathbf{k}}^{0}\right)\right] \quad , \\ \Xi_{\mathbf{q}} &= \frac{\tau_{\mathbf{q}}}{2} \sum_{\mathbf{k}} \left[-\mathscr{P}^{+}\left(n_{\mathbf{q}}^{0} + f_{\mathbf{k}'}^{0}\right) + \mathscr{P}^{-}\left(1 + n_{\mathbf{q}}^{0} - f_{\mathbf{k}'}^{0}\right)\right] \quad . \end{aligned} \tag{2.2.54}$$

Even though this scheme looks quite simple, its actual evaluation is extremly demanding since each sum typically runs over thousands of **k** and **q** points in addition to the number of bands, phonon modes and spin channels. One has to keep further in mind that combinations of $\Xi_{\mathbf{k}}$ and $\Xi_{\mathbf{q}}$ are not factorised, they are nested sums.

3 | Results

3.1. Essential quantities

The calculation of the electron-phonon interaction can be divided into two parts. One deals with the geometrical pairing mechanism due to the conservation of energy and momentum. The other one is related to the interaction strength of the electrons coupled via a phonon. Both ingredients are discussed in the upcoming section.

The first part is about the nesting function, which is a purely geometrical quantity. It will be discussed from an educational and computational perspective. A detailed analysis can be very challenging especially in the case of a manifold Fermi surface like in lead. The basic ideas and principles are therefore discussed at the Fermi surface of copper in the beginning. The second part deals with the electron-phonon matrix element $g^{\mathbf{q}}_{\mathbf{k},\mathbf{k}+\mathbf{q}}$ of the nested electron pairs in lead. Phonon properties and matrix elements are illustrated for a single initial electron state. Subsequently, the integrated coupling strength for each electron state at the Fermi surface is shown and their structure is discussed.

3.1.1. Nesting

Single sheeted Fermi surface: Copper

Figure 3.1 shows the construction of nested pairs at the Fermi surface. The initial electron state $\mathbf{k}$ (blue point) is fixed and all final states $\mathbf{k}'$ are shown in yellow. The quasi-elastic assumption is not used here, which means that phonons were explicitly matched according to their momentum, $\mathbf{k}' = \mathbf{k} + \mathbf{q}$, and energy, $\epsilon_{\mathbf{k}+\mathbf{q}} = \epsilon_{\mathbf{k}} + \hbar\omega_{\mathbf{q}}$. The phonon energy is set to 5meV. Nevertheless, the final states at $\epsilon_{\mathbf{k}+\mathbf{q}}$ are shown on the initial Fermi surface because the iso-energy surface does not change significantly within 5meV around ϵ_{F}. The deviation $\Delta|\mathbf{k}|$ for instance is $\sim 1 \times 10^{-4}$ along $\overline{\mathrm{WX}}$ and $\sim 4 \times 10^{-4}$ along $\overline{\Gamma\mathrm{X}}$ in units of $({}^{2\pi}/_{a})$, which is negligible with respect to the used accuracy of $\Delta|\mathbf{k}| = 1 \times 10^{-2}$ for finding an electron pair. Despite the fact that this value is quite large only less than 1% of the phonons mediate a nested pair.

The left figure shows the construction for an initial state along the $\overline{\Gamma\mathrm{X}}$ direction, which nearby environment at the Fermi surface is almost a sphere. The phonon iso-energy surfaces at 5meV are also shown and the connecting phonons are marked in yellow. As a consequence of the sperical-like Fermi surface they form rings at each phonon surface, which directly transfers to the ring structure of the final states at the Fermi surface. As long as Umklapp processes are not possible the nested final states always form a more or less ring-like pattern around the initial state. However, the construction is more complicated if the phonon momentum is large, the initial state is close to the zone boundary or the electron iso-energy surface of the final states changes significantly compared to the Fermi surface because Umklapp processes are then possible. Such an example is shown in the right figure. The initial

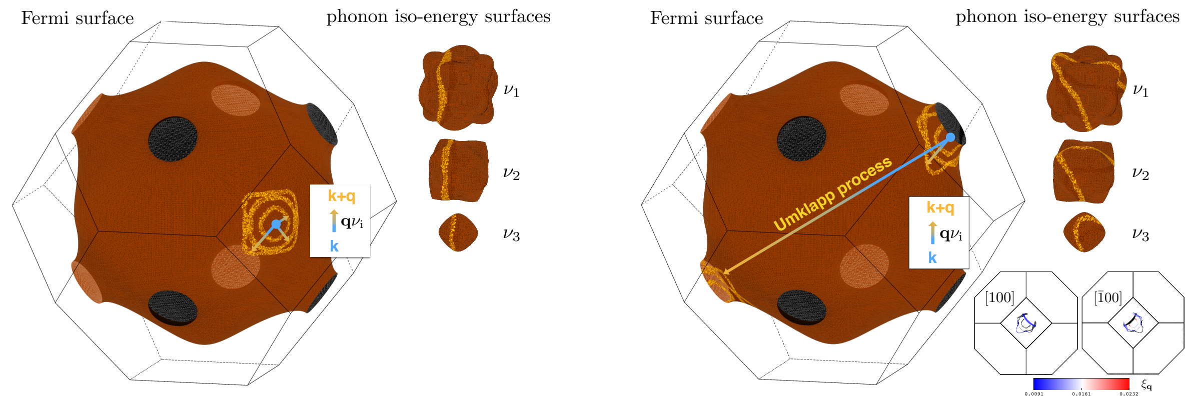

Figure 3.1.: Visualisation of nesting at the Fermi surface of copper due to transitions with phonons with $\hbar\omega_{\mathbf{q}} = 5\text{meV}$. The initial electron state $\mathbf{k}$ is highlighted as a blue point. All possible final states are shown in dark orange, while the actual connected final states $\mathbf{k}+\mathbf{q}$ are marked in yellow. Since the electron iso-energy surface does not change significantly within 5meV, initial and final states are both shown at the Fermi surface ($\epsilon_{\mathbf{k}} = \epsilon_{\mathbf{k}+\mathbf{q}}$). The colored arrows (blue-yellow) indicate the involved phonon wave vectors $\mathbf{q}$ with respect to the phonon mode ν. The corresponding iso-energy surfaces of the phonons are given next to the Fermi surfaces. Again, available phonon states are shown in dark orange and involved phonon states are marked in yellow. Left: Initial electron state is along $\overline{\Gamma X}$. Right: Initial electron state is located near the neck and lies at the zone boundary. Therefore, the phonon momentum is large enough to allow for Umklapp processes. The two figures bottom right show only the involved phonon wave vectors from all three modes. Their nesting values $\xi_{\mathbf{q}}$ are given as superimposed color code.

state is at the neck and lies directly at the zone boundary. The ring-like pattern of the final states still occurs but splits due to Normal and Umklapp processes. The first one forms the usual pattern, which was already explained. The second one, however, also forms a ring-like pattern but at a different position according to the reciprocal lattice vector used to construct the nested pairs. The figure in the bottom right corner additionally shows the nesting value $\xi_{\mathbf{q}}$ of the phonons. The largest values are obtained for phonons in the third mode, $\nu = 3$. Their momentum is small and therefore the velocities $\mathbf{v}_{\mathbf{k}}$ and $\mathbf{v}_{\mathbf{k}+\mathbf{q}}$ are still similarly orientated to each other, which maximises the denominator in equation 2.1.56.

Applying the quasi-elastic assumption allows coupling of electron states with phonons with an arbitrary momentum. This would lead to a fully-nested Fermi surface of final electron states. To compare it with figure 3.1, it means that every state in the left or right figure would appear in yellow.

Multi sheeted Fermi surface: Lead

As already discussed in section 2.1.2, the nesting function $\xi_{\mathbf{q}}$ allows for the identification of phonons from a geometrical point of view, which might be important for the interaction of electrons and phonons.

Figure 3.2(a) shows $\xi_{\mathbf{q}}$ for initial and final states at the Fermi surface wihtin the quasi-elastic assumption for phonons along the high symmetry line. Due to the two Fermi sheets in lead one can distinguish between four nesting types - interband, intraband (inner sheet), intraband (outer sheet) and total nesting as combination of the other three. Each type and $\xi_{\mathbf{q}}$ in general have in common, that it holds $\xi_{\mathbf{q}} \longrightarrow \infty$ for $\mathbf{q} \longrightarrow 0$ due to the collinear alignment of the electron velocities. Phonons with $\mathbf{q} \neq 0$ and diverging or large nesting values connect parallel oriented parts of the Fermi surface, where the velocities of $\mathbf{k}$ and $\mathbf{k}+\mathbf{q}$ are (anti)parallel or almost (anti)parallel oriented to each other. These phonons typically connect large parts of the Fermi surface, which might resolve in a strong electron-phonon coupling. Within the literature these occurrences are known as Kohn anomalies and can be observed as a softening of phonon modes [7, 8, 68, 107, 142].

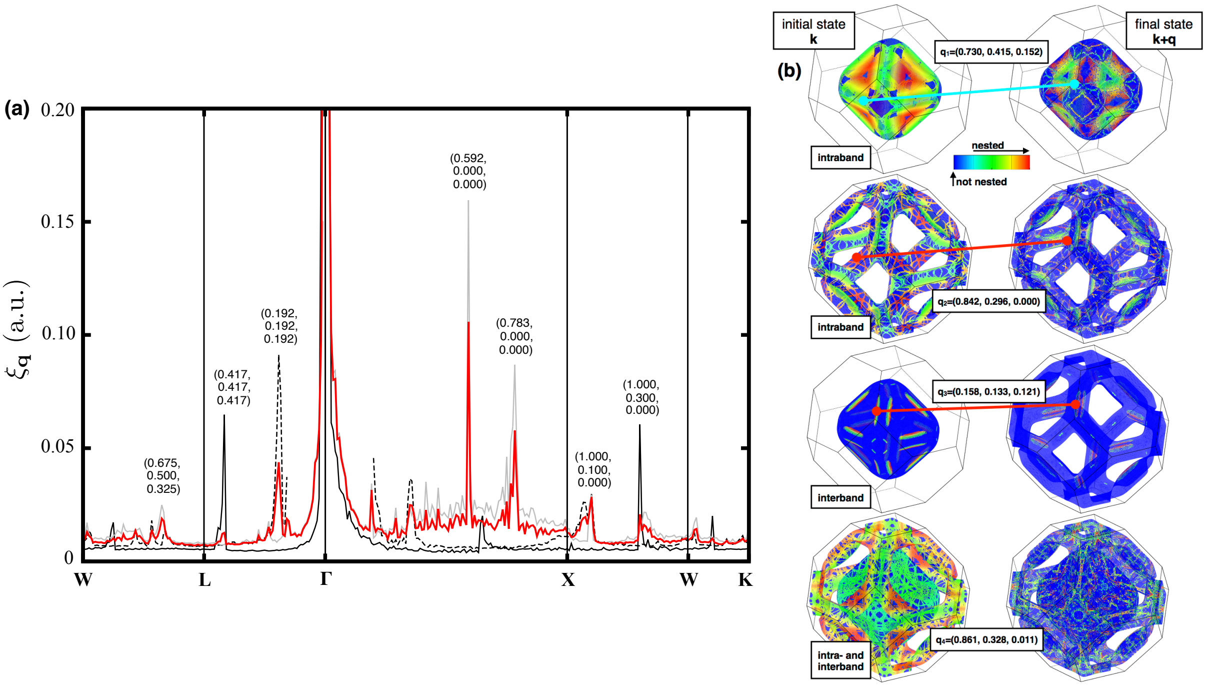

Figure 3.2.: Nesting in Pb at the Fermi energy. Left: Nesting function $\xi_{\mathbf{q}}$. The solid black (gray) line corresponds to intraband transitions in the inner (outer) Fermi sheet, while the dashed black line refers to interband transitions. The total nesting function for the whole Fermi surface, without distinguishing between intra- and interband transitions, is given in red. In each case the divergence at $\mathbf{q} = \mathbf{0}$ is obvious due to collinear velocities with $\mathbf{v}_{\mathbf{k}} = \mathbf{v}_{\mathbf{k}+\mathbf{q}}$. Right: Nested electronic states via phonons with the highest nesting value $\xi_{\mathbf{q}}$. Same color marks a nested pair with initial and final state, except for blue, which displays the bare Fermi surface. If $\mathbf{q}$ connects more than one pair only the pair with the highest weight is given. The top two figures show intraband transitions mediated by $\mathbf{q}_1$ (inner sheet, $\xi_{\mathbf{q}_1} \approx 0.495$) and $\mathbf{q}_2$ (outer sheet, $\xi_{\mathbf{q}_2} \approx 0.19$). The bottom figures show interband transitions via $\mathbf{q}_3$ ($\xi_{\mathbf{q}_3} \approx 0.219$) and the result, which accounts for both transition types ($\xi_{\mathbf{q}_4} \approx 0.108$).

Looking at each Fermi sheet separately (solid black (grey) line), $\xi_{\mathbf{q}}$ gets maximal at different wave vectors, according to the topology of each sheet, e.g. $\mathbf{q}_{\mathrm{in}}^{\mathrm{intra}} = (0.417, 0.417, 0.417)$ or $\mathbf{q}_{\mathrm{out}}^{\mathrm{intra}} = (0.592, 0.0, 0.0)$. The combination of intra- and interband transitions (red line) leads to a drastical reduction of some peaks due to the weighting with the total number of transitions, e.g. $\mathbf{q}_{\mathrm{B1}}^{\mathrm{intra}}$, while others remain dominant, e.g. $\mathbf{q}_{\mathrm{B2}}^{\mathrm{intra}}$.

The visualisation of nested pairs at a three-dimensional Fermi surface is complicated and usually done with two-dimensional cuts through the Fermi surface along certain high symmetry directions, which is shown for lead by Dal Corso *et. al* [28]. Figure 3.2(b) shows an approach, which is different from the more educational investigation of phonons along a high symmetry line. Here, wave vectors in the full phonon spectra with larger nesting values are shown. To be more precise, each of the four figures shows connected initial and final states via the phonon with the largest nesting. The pairs share the same color. If the phonon couples more than two states only the pair with the highest contribution to $\xi_{\mathbf{q}}$ is given. Comparing the nesting values given in the caption of figure 3.2 one can see, that the largest nesting vectors lie off the high symmetry line, especially in the case of separated intra- and interband transitions. Nevertheless, the visualisation of connected states with this approach is only practicable for single sheeted Fermi surfaces or simple multi sheeted ones. Otherwise the visual tracking of pairs is almost impossible as one can imagine from the bottom figure in (b).

The construction of nested pairs described in this section can be done only for an in-depth analysis of a certain problem. Using this scheme to compute the electron-phonon interaction and their influence on transport properties even within the quasi-elastic assumption is very demanding in terms of computational power and probably not worth the effort. Hence, a usual electron-phonon calculation is done without the construction of discrete electron and phonon iso-energy surfaces. By initialisation of the $\mathbf{k}$- and $\mathbf{q}$-grids, the initial and final electron states are always connected via a phonon and their effective contribution is measured with a smearing technique with respect to the energy of inital and final electron states. A more detailed description is given by the developers of the EPW code [43, 89, 103, 110]. Eventually, this scheme is very effective and the smearing technique can be qualitatively related to the discrete matching of states in the sense, that the smearing itself is the counterpart of the accuracy for finding a nested pair. Nevertheless, results obtained with one or the other approaches have to be checked for convergence regarding the smearing value or the accuracy anyhow.

3.1.2. Electron-phonon matrix elements

Mode-resolved coupling strength for one initial electron state

In addition to the purely geometrical tool of the nesting function, the coupling between electrons and phonons, given by $g^{\mathbf{q}}_{\mathbf{k},\mathbf{k}+\mathbf{q}}$ in eq. 2.2.11, is naturally of major interest.

The visualisation of the interaction strength in 3D-systems is quite difficult and confusing compared to 2D-systems, where $\left|g^{\mathbf{q}}_{\mathbf{k},\mathbf{k}+\mathbf{q}}\right|^2$ can be easily shown in a 2D-contour plot [50, 104]. Therefore, one initial electron state is selected and the properties of the phonons and the coupling strengths arising from these phonons are shown in figure 3.3. The selected electron state lies at the inner Fermi sheet along the $\overline{\Gamma X}$ direction (inset fig. 3.3(a), blue point). Considering a dense $\mathbf{q}$ grid with 2×10^6 phonons in the full Brillouin zone, only 12% are able to connect this state to a final electron state. The connecting phonons are well distributed within their available phase space (black background in (b)). Only low energy phonons with $|\mathbf{q}| \lesssim 0.1$ do not couple because the distance between the initial state and the

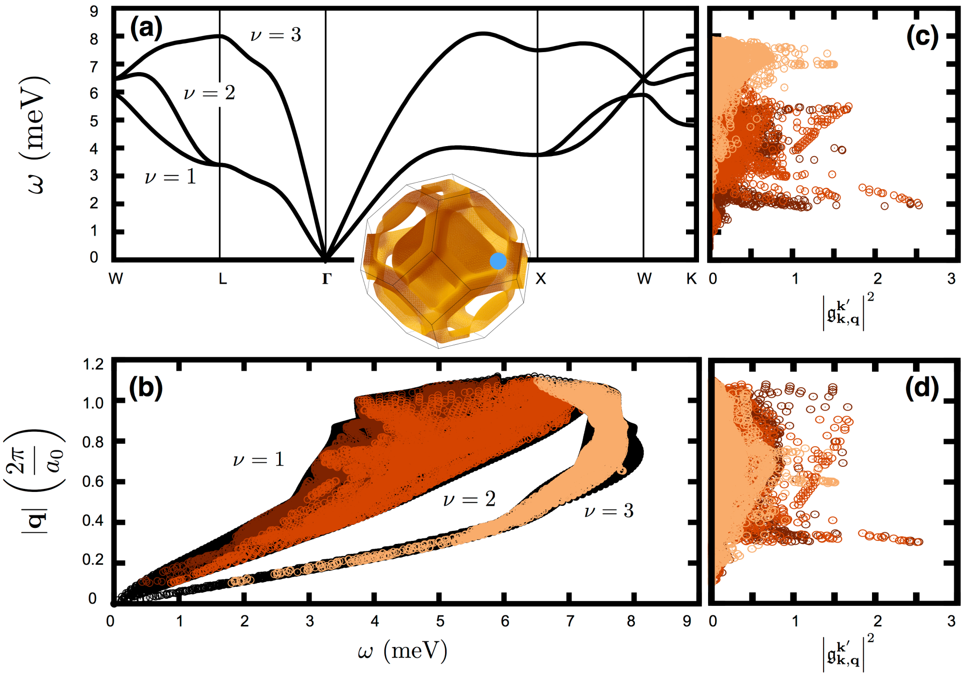

Figure 3.3.: Various phonon properties and mode-resolved electron-phonon matrix elements in lead. Each phonon mode ($\nu = 1, 2, 3$) is assigned a different color (brown, orange and yellow). The inset shows the two-sheeted Fermi surface and the blue point marks one selected initial electron state. The final states are not shown but detailed information about the connecting phonons are given in the remaining figures (b)-(d), where each circle tags one phonon wave vector. (a) Phonon dispersion. (b) Absolute wave vector of the connecting phonons with respect to their energy. The black background points show the available phonon phase space. (c), (d) Squared electron-phonon matrix elements $g^{\mathbf{q}}_{\mathbf{k},\mathbf{k}+\mathbf{q}}$ of the connecting phonons with respect to their energy and absolute wave vector, respectively.

final states at the second Fermi sheet is to large. Furthermore, coupling at the same Fermi sheet is not possible due the orientation of these phonons rather than their absolute momentum. The slope of the phonon dispersion around Γ is to large to enable a geometrical connection between the final electron states, which lie in the weak curved area around the initial state. The mode-resolved coupling strengths $\left|g^{\mathbf{q}}_{\mathbf{k},\mathbf{k+q}}\right|^2$ shown in (c) and (d) reveal additional qualitative informations. The highest coupling strengths are found for the two transversale phonon modes with energies around 2meV and and a distinct absolute momentum $|\mathbf{q}| \approx 0.3$. The remaining phonons with $\left|g^{\mathbf{q}}_{\mathbf{k},\mathbf{k+q}}\right|^2 > 1$ are more distributed with respect to $|\mathbf{q}|$. A decomposition of the coupling processes with respect to transition types yields a ratio of 34% intra- and 66% interband transitions. This ratio counts the bare number of transitions. The ratio concerning the integrated coupling strengths, however, is even larger yielding 15% and 85% for intra- and interband transitions. Thus, the overall coupling is stronger for interband than for intraband transitions.

However, such a detailed analysis is often not necessary, because for instance the relaxation time is eventually only **q**- or **k**-dependent and the summation over **k** or **q** can easily suppress certain details. Nevertheless, it could be useful if the Fermi surface is simpler like in silicon. Consider Si to be slightly n-doped Si with a 6-fold degenerate Fermi surface, the number of coupling phonons will be drastically reduced for each initial electron state compared to the available phase space, which is shown in section 3.2.1 in figure 3.10. Hence, a pronounced feature in the coupling strength might show up in the integrated quantities, e.g. $\tau_{\mathbf{k}}$ or $\tau_{\mathbf{q}}$.

State-dependent matrix elements at the Fermi surface

Integrating over all phonon information for each initial electron state leads to a pure **k**-dependence of the coupling strength, which can be displayed at the Fermi surface as shown in figure 3.4(a). One can see, that the coupling strength is larger at the outer Fermi sheet. The average difference between the coupling at the outer and inner sheet is almost a factor of 1.6. This is larger than the average variation within the sheets, which is roughly 30%. Although the figure shows only the coupling strength, it

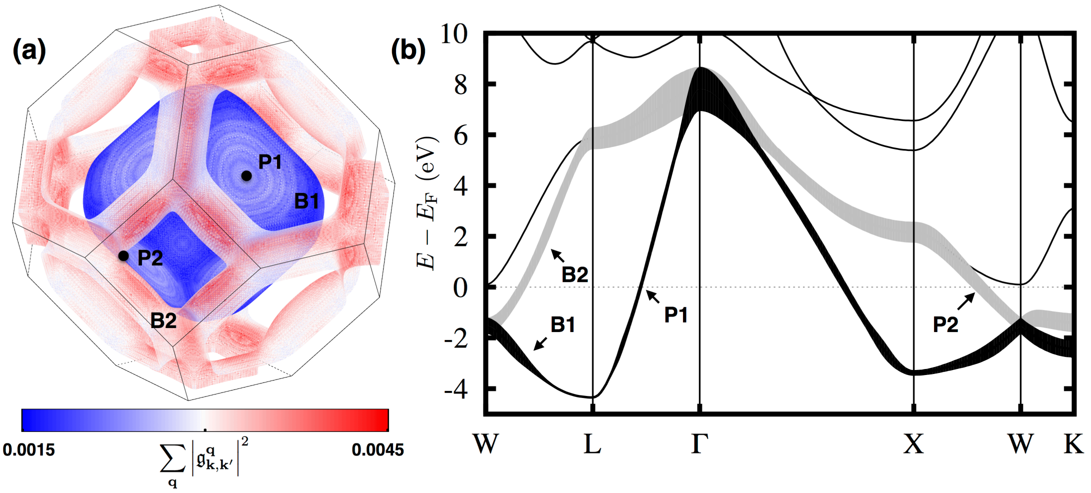

Figure 3.4.: (a) State-dependent electron-phonon matrix element in lead integrated over all phonons. $\sum_{\mathbf{q}}\left|g^{\mathbf{q}}_{\mathbf{k},\mathbf{k+q}}\right|^2$ is shown for each initial state at the Fermi surface. No distinction between intra- and interband scattering was made. Overall, the coupling is larger at the outer Fermi sheet. Two states (P1, P2) are marked additionally at the inner (B1) and outer (B2) Fermi sheet. The properties of these states will be discussed in detail in section 3.2. (b) Calculated band structure of lead within the scalar-relativistic framework. The width of the superimposed shaded areas onto the electronic states of band B1 and B2 is related to the magnitude of the **k**-dependent linewidth $\Gamma_{\mathbf{k}}$ due to electron-phonon interaction at 300K, which is shown and discussed in section 3.2.

already provides a good idea of the structure of the electron relaxation time. Since $\tau_{\mathbf{k}}$ is inverse proportional to the coupling strength initial states at the inner Fermi sheet will have larger relaxation times than states at the outer Fermi sheet. The missing prefactors, the δ-distribution and the occupation functions as part of $\tau_{\mathbf{k}}$ in equation (2.2.20) are solely important for the correct value of $\tau_{\mathbf{k}}$ but will not change the structure at the Fermi surface. The relaxation time itself is shown later on.

The band structure of lead is given in (b) to close this chapter. The calculation was done on a scalar-relativistic level. It resembles previous calculations[54, 126, 138] quite good but reveals deviations from experiments and fully-relativistic calculations due to spin-orbit interaction. Hence, the avoided crossing due to the spin-orbit coupling at W, L, Γ and on the high-symmetry line $\overline{\mathrm{XW}}$ is not seen in the figure. Nevertheless, these regions are not close to the Fermi energy and their influence on transport properties, e.g. the electrical conductivity or the thermopower, should be rather small.

3.2. Properties related to the imaginary part of the electron self-energy

The interaction of electrons and phonons leads to a broadening of electron as well as phonon states known as linewidth $\Gamma_{\mathbf{k}}$ and $\gamma_{\mathbf{q}}$, respectively. Both are indirect proportional to their relaxation times $\tau_{\mathbf{k}}$ and $\tau_{\mathbf{q}}$ and therefore of interest in transport calculations. Recent publications discuss the structure of $\tau_{\mathbf{k}}$ at the Fermi surface [100] as well as the influence of $\tau_{\mathbf{k}}$ onto the mobility, conductivity and other transport properties [17, 18, 50, 79, 81, 82, 130, 141], which shows the renewed interest in electron-phonon interaction in the last decade.

The first part of the following chapter addresses the impact of the electron-phonon interaction onto the electrons primarily by means of the relaxation time. Results are shown for lead and n-doped silicon for states at the Fermi energy. The second part is about state-dependent coupling constants $\lambda_{\mathbf{k}}$, Éliashberg functions $\alpha^2 F_{\mathbf{k}}$ and relaxation times $\tau_{\mathbf{k}}$ in lead for states, which are not at the Fermi surface. Part three and four deal with the transition from $\tau_{\mathbf{k}}$ to $\tau(E)$ and its influence onto the electrical conductivity and thermopower. Additionally, several common approximations for the relaxation time are discussed.

3.2.1. Vital transport properties at the Fermi surface

Lead

The matrix elements as well as the relaxation times and all other quantities needed to calculate the electrical conductivity and thermopower are calculated on a fine **k** point mesh with at least 40'000 points in the irreducible part of the Brillouin zone. The phonon grid is of the same size leading to more than 2.2 million **q** points in the full Brillouin zone, which are paired with each **k** point. A possible speed up of the calculation could be achieved due to the restriction of phonons to lie in the irreducible part of the Brillouin zone as well. This implies knowledge about the transformation of the matrix elements under symmetry operations with respect to **k** and **q**. The Fermi surface was extracted with an adaptive tetrahedron method[137] and consists of roughly 460'000 **k** points at the whole surface.

The relaxation time at the Fermi surface is shown in figure 3.5(a). $\tau_{\mathbf{k}}$ of the inner sheet (B1) is almost always larger than $\tau_{\mathbf{k}}$ of the outer sheet (B2). This was already explained in section 3.1.2 with the different magnitudes of the integrated matrix elements $\sum_{\mathbf{q}} \left|g^{\mathbf{q}}_{\mathbf{k},\mathbf{k}+\mathbf{q}}\right|^2$. The averaged relaxation times are $\bar{\tau}_{\mathrm{B1}} = 4.61\mathrm{fs}$ and $\bar{\tau}_{\mathrm{B2}} = 3.21\mathrm{fs}$ while the total Fermi surface averaged relaxation time is 3.6fs. Calculating τ in the high temperature limit according to

$$\tau(\epsilon_{\mathrm{F}}) = \frac{\hbar}{2\pi k_{\mathrm{B}}\lambda T} \quad , \tag{3.2.1}$$

which is reasonable at 300K, leads to values in the range 2.4 – 5.1fs for coupling constants from 1.7 to 0.8, which can be found in the literature for similar calculations based on a scalar-relativistic treatment [8, 38, 83]. The obtained coupling constant with $\tau = 3.6\mathrm{fs}$ is 1.13 and slightly larger than $\lambda = 1.05$ as reported by Sklyadneva *et. al* [126].

There is probably no obvious qualitative correlation between the carrier velocity $\mathbf{v}_{\mathbf{k}}$ of the initial state and its relaxation time $\tau_{\mathbf{k}}$ as one might suspect from recent results found for noble metals by

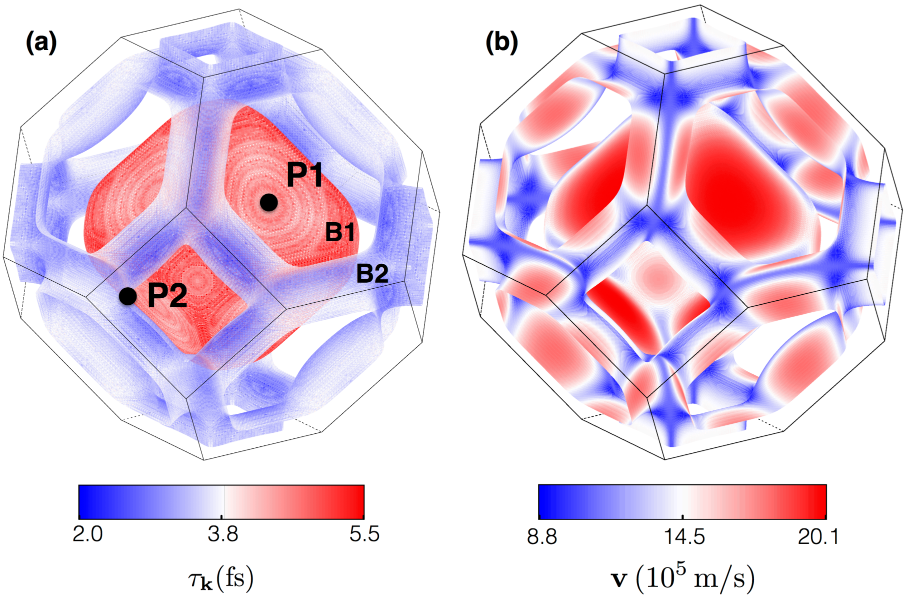

Figure 3.5.: (a) Fermi surface of Pb showing the **k**-dependent electron-phonon relaxation times $\tau_{\mathbf{k}}$ at T = 300K superimposed onto the two Fermi sheets. $\tau_{\mathbf{k}}$ is obtained within the relaxation time approximation. The relaxation time is almost doubled in the inner sheet (B1) indicating a less efficient electron-phonon coupling compared to the outer sheet (B2). $\tau_{\mathbf{k}}$ in P1 and P2 is about 4.60fs and 3.27fs, respectively. (b) Fermi surface with the superimposed Fermi velocities.

Mustafa *et. al*[100]. The relaxation time of a free electron is given within the Drude model by

$$\tau_D = \frac{m^*}{ne^2\rho} \quad . \tag{3.2.2}$$

Here, ρ is the electrical resistivity, n is the carrier density and m^* is the effective mass. The latter is indirect proportional to the velocity $m^* \propto v^{-1}$, which transfers directly to the relaxation time yielding $\tau_{\mathbf{k}} \propto (\mathbf{v}_{\mathbf{k}})^{-1}$ for a spherical Fermi surface. Surprisingly, this is partially valid in lead (fig. 3.6), since scattering from an initial state at the inner Fermi sheet (B1) shows an indirect proportionality between $\tau_{\mathbf{k}}$ and $\mathbf{v}_{\mathbf{k}}$ as well. On the other hand, it holds $\tau_{\mathbf{k}} \propto \mathbf{v}_{\mathbf{k}}$ for scattering starting at the outer Fermi sheet (B2). Additionally, an analysis of the orbital character of initial and final states, to predict smaller or larger relaxation times, as suggested in Ref. [100], fails for the particular case of Pb as well since states around the Fermi energy are dominated by p-type orbital character.

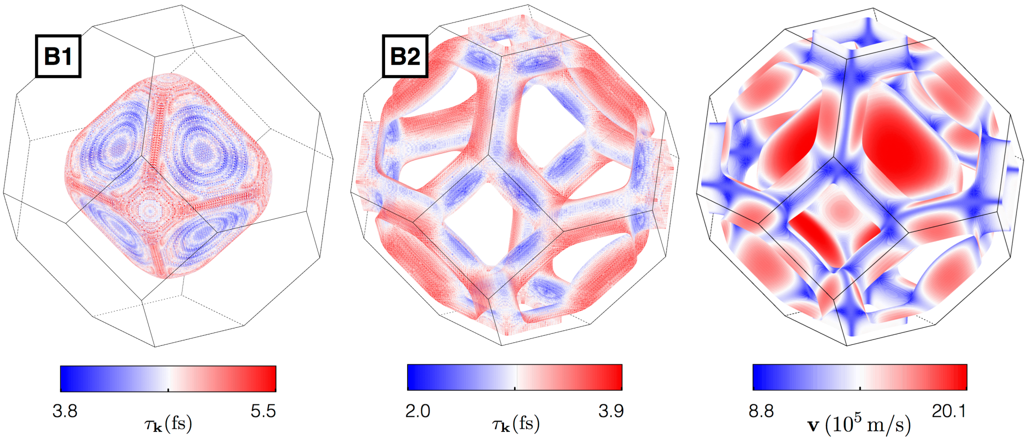

Figure 3.6.: Left and middle: **k**-dependent electron-phonon relaxation times for initial states at the inner (B1) and outer Fermi sheet (B2) at T = 300K. The velocities are given as well (right) to show that there is no clear relation between a large (small) $\tau_{\mathbf{k}}$ and a small (large) $\mathbf{v}_{\mathbf{k}}$.

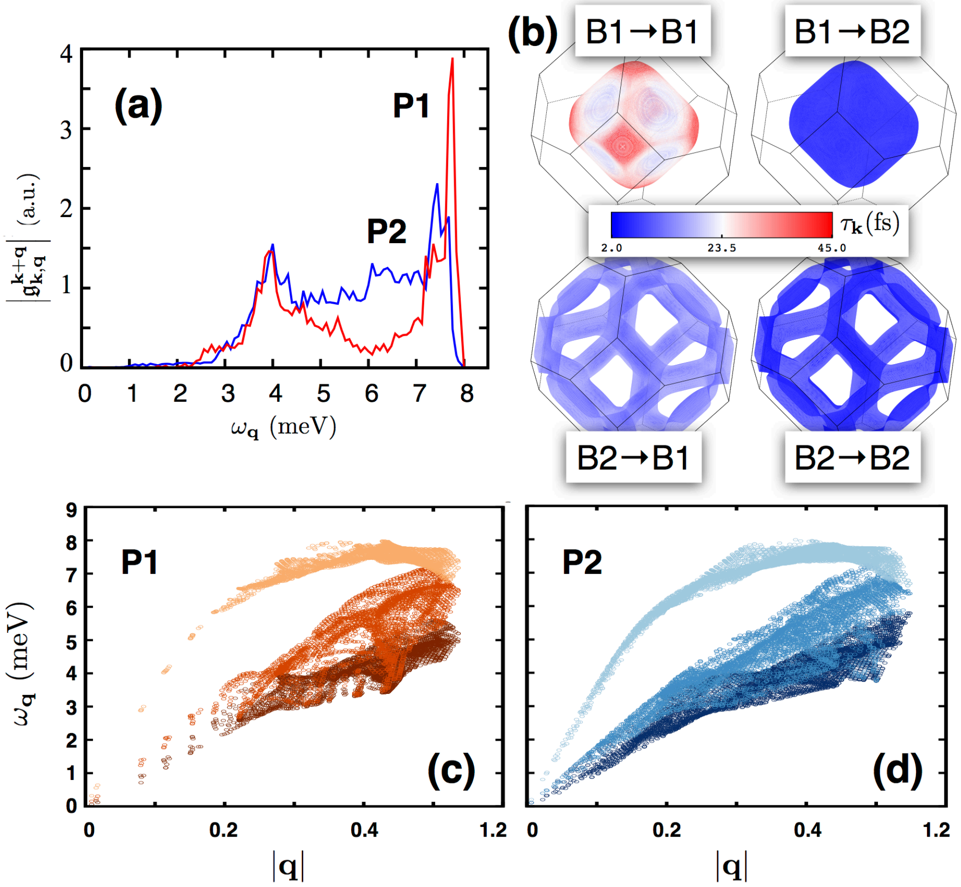

Figure 3.7.: (a) Electron-phonon matrix elements plotted versus the corresponding phonon energies for P1 and P2 shown in figure 3.5(a). The latter exhibits an uniform and in total larger electron-phonon coupling strength, which explains the smaller relaxation time. (b) Contributing parts to $\tau_{\mathbf{k}}$ arising from intra- and interband transitions. Each transition type is treated separatly and shown are the initial states. For both transition types, scattering at/to the inner sheet (B1) results in larger relaxation times but the Fermi surface averaged $\tau_{\mathbf{k}}$ is dominated by the scattering at/to the outer sheet (B2). (c,d) Phonon energies versus absolute momentum for phonons being involved in the scattering processes from the initial states P1 and P2. Each color corresponds to one phonon mode.

A closer look at fig. 3.5(a) reveals the high anisotropic structure of $\tau_{\mathbf{k}}$ throughout the Brillouin zone. This can be related to the shape of the Fermi surface itself and is discussed exemplarily for two states P1 and P2. Starting at P2, the variety of phonon momentum and energy is much larger compared to coupling from P1 because the Fermi surface is more structured around P2. Additionally, the bands are closer to each other, which allows the coupling of phonons with smaller momentum as seen in figure 3.7(d). Phonons with small momentum can be found at P1 as well but the surrounding at P1 preferably favours coupling in distinct directions, which can be seen in 3.7(c) due to the sparse filling. Hence, certain Fermi surfaces, probably simple ones, could act as a phonon filter.

Apart from the geometrical aspects, the **q**-dependent coupling strength in figure 3.7(a) shows two distinct peaks for P1 and is more uniform for P2, which can be taken as an expression of the geometrical phonon selection as well. The summation over **q** shows that the overall coupling for P2 is larger than for P1 and hence the relaxation time is smaller. Decomposing the relaxation time into contributions from intra- and interband scattering, one can see that the averaged $\tau(\epsilon_{\mathrm{F}})$ is dominated by transitions B1⟶B2 and B2⟶B2 (fig. 3.7(b)). Large relaxation times from transitions B1⟶B1 and B2⟶B1 are suppressed as one needs to add up the scattering rates instead of the scattering times to account for Matthiesen's rule. A comparison of the intraband transitions indicates that a simple single-sheeted Fermi surface exhibits larger relaxation times than complicated multi-sheeted ones. The enhancement

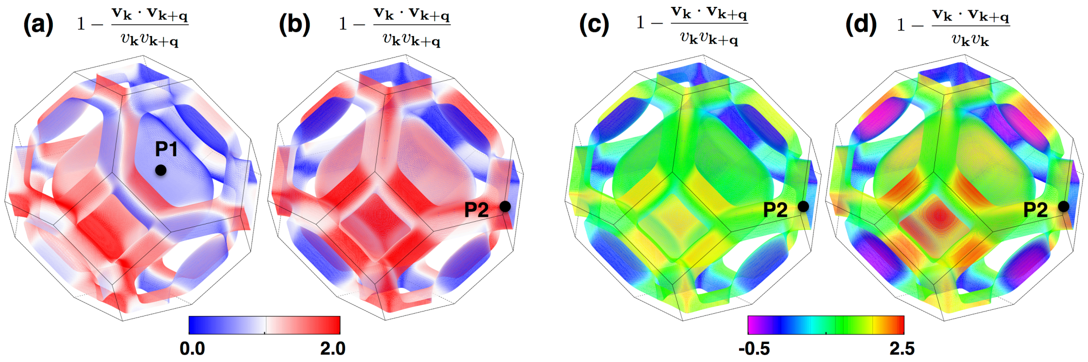
(a) $1-\frac{\mathbf{v}_{\mathbf{k}}\cdot\mathbf{v}_{\mathbf{k}+\mathbf{q}}}{v_{\mathbf{k}}v_{\mathbf{k}+\mathbf{q}}}$
(b) $1-\frac{\mathbf{v}_{\mathbf{k}}\cdot\mathbf{v}_{\mathbf{k}+\mathbf{q}}}{v_{\mathbf{k}}v_{\mathbf{k}+\mathbf{q}}}$
(c) $1-\frac{\mathbf{v}_{\mathbf{k}}\cdot\mathbf{v}_{\mathbf{k}+\mathbf{q}}}{v_{\mathbf{k}}v_{\mathbf{k}+\mathbf{q}}}$
(d) $1-\frac{\mathbf{v}_{\mathbf{k}}\cdot\mathbf{v}_{\mathbf{k}+\mathbf{q}}}{v_{\mathbf{k}}v_{\mathbf{k}}}$
P1
P2
P2
P2
0.0
2.0
-0.5
2.5

Figure 3.8.: Illustration of the efficiency factor, which is used for computing the transport relaxation time $\tau_{\mathbf{k}}^{\mathrm{tr}}$ or transport coupling constant $\lambda_{\mathbf{k}}^{\mathrm{tr}}$ in lead. The efficiency factor is shown for a single initial state coupled to all final states via phonons with wave vector $\mathbf{q}$. Initial states are P1 (a) and P2 (b)-(d). (c) and (d) shows the difference between the correct efficiency factor and a slightly different version, which is sometimes found in the literature. It is clearly seen, that the latter yields results, which are outside the value range $[0, 2]$. Further information are given in the text.

is up to 600% for the averaged values $\bar{\tau}_{\mathrm{B1}}^{\mathrm{intra}}$ and $\bar{\tau}_{\mathrm{B2}}^{\mathrm{intra}}$ in the case of lead.

To complete the detailed investigation of the electron states P1 and P2 figure 3.8 shows the efficiency factor

$$\eta_{\mathbf{k}} = 1 - \frac{\mathbf{v}_{\mathbf{k}} \cdot \mathbf{v}_{\mathbf{k}+\mathbf{q}}}{v_{\mathbf{k}}\, v_{\mathbf{k}+\mathbf{q}}} \tag{3.2.3}$$

for P1 (a) and P2 (b) as initial states. The value range for $\eta_{\mathbf{k}}$ is $[0, 2]$. It is minimal if $\mathbf{v}_{\mathbf{k}}$ and $\mathbf{v}_{\mathbf{k}+\mathbf{q}}$ are parallel alined while it is maximal if the velocities are anti-parallel alined. These properties are also known as forward- and backward-scattering. Sometimes in the literature the efficiency factor is calculated with a different denominator as $\tilde{\eta}_{\mathbf{k}} = 1 - \mathbf{v}_{\mathbf{k}} \cdot \mathbf{v}_{\mathbf{k}+\mathbf{q}}/v_{\mathbf{k}} v_{\mathbf{k}}$, which might yield false results as shown by comparison of (c) and (d). This seems to be the case especially for complicated manifold Fermi surfaces but might be not seen for simple single-sheeted Fermi surfaces. Assuming an isotropic spherical Fermi surface, the efficiency factor in eq. 3.2.3 would reduce to well-known expresssion $(1 - \cos(\mathbf{k}, \mathbf{k} + \mathbf{q}))$, which depends only on the angles between $\mathbf{k}$ and $\mathbf{k}'$ and would be the same if derived from the false expression of the efficiency factor.

Figure 3.9 gives insigths to some computational details while calculating the relaxation time. Shown

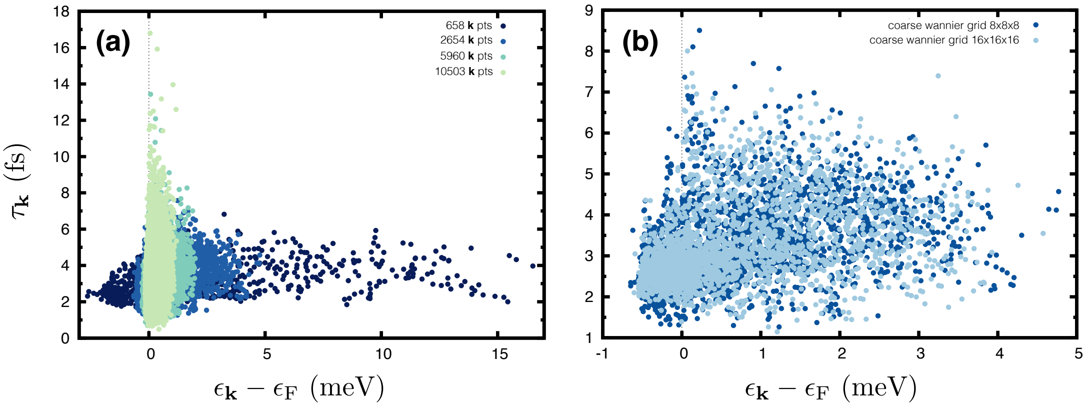

Figure 3.9.: Behaviour of the $\mathbf{k}$-dependent relaxation time for states at the inner Fermi sheet in lead within respect to several $\mathbf{k}$ point densities. The difference $\Delta\epsilon = \epsilon_{\mathbf{k}} - \epsilon_{\mathrm{F}}$ arises from the technical procedure, which is explained in the text. (a) In each case, the coarse wannier grid is given by an 8x8x8 $\mathbf{k}$-point mesh while the number of $\mathbf{k}$ points in the fine grid increases. The given numbers are the $\mathbf{k}$ points at the Fermi surface in the irreducible part of the Brillouin zone. The energy difference ΔE decreases with an increasing number of $\mathbf{k}$ points from 20meV to 1meV. The change of the values of $\tau_{\mathbf{k}}$ is also explained in the text. (b) The number of phonons and fine $\mathbf{k}$ points are fixed but the coarse wannier grid is changed from 8x8x8 to 16x16x16 revealing no significant impact onto $\epsilon_{\mathbf{k}}$ and $\tau_{\mathbf{k}}$.

is the influence of different fine (a) and coarse (b) $\mathbf{k}$ point grids onto $\tau_{\mathbf{k}}$. Each point in the figures displays a relaxation time at the Fermi surface of the inner Fermi sheet B1. Hence, the energy difference $\Delta\epsilon = \epsilon_{\mathbf{k}} - \epsilon_{\mathrm{F}}$ should be zero for every state. The reason for $\Delta\epsilon \neq 0$ stems from numerical inaccuracies when evaluating the Fermi surface. The eigenvalues $\epsilon_{\mathbf{k}}$ are computed within the EPW code but the Fermi surface is constructed separatly, which generates a new set of $\mathbf{k}$ points. These $\mathbf{k}$ points are then read into EPW and the matrix elements and relaxation times are calculated subsequently. In the end, the spread of $\epsilon_{\mathbf{k}}$ around ϵ_{F} arises from the density of the starting uniform grid due to the Fermi surface, which is described more accurately by the tetrahedron method if the $\mathbf{k}$ points are finer sampled. Hence, the energy difference $\Delta\epsilon$ is smaller. The sharpening of $\tau_{\mathbf{k}}$ with increasing number of $\mathbf{k}$ points at the Fermi surface, which coincides with a denser starting grid, is related to the approximation of the δ-distribution $\delta(\epsilon_{\mathbf{k}} - \epsilon_{\mathrm{F}})$ by a gaussian broadening function. Depending on the smearing value, the calculated relaxation time is washed out if $\Delta\epsilon$ is getting larger. Probably, these difficulties could be eliminated if the tetrahedron method would be directly implemented into the EPW code. Nevertheless, the energy difference can be decreased to roughly 1 meV, which is acceptable. The influence of the coarse $\mathbf{k}$ point mesh onto $\tau_{\mathbf{k}}$, which is important during the transformation of Bloch quantities to their Wannier representation, is exemplarily shown in (b). The differences between the calculations with an 8x8x8 and a 16x16x16 grid are small. No significant impact can be found neither onto $\tau_{\mathbf{k}}$ not on the energy spread $\Delta\epsilon = \epsilon_{\mathbf{k}} - \epsilon_{\mathrm{F}}$.

Silicon

The previous discussion is not restricted to metals and can be applied to semiconductors as well. Figure 3.10 summarises the results for silicon implying nesting, coupling strength and relaxation times at zero temperature.

The system is n-doped and the Fermi surface consists of 6 pockets, which are aligned along the $\overline{\Gamma X}$ directions (b). The connection between states in these pockets or between these pockets is known as intra- and intervalley transition and is restricted to either phonons with small momentum or to phonons with large momentum and an additional orientational dependency. The orientation is roughly

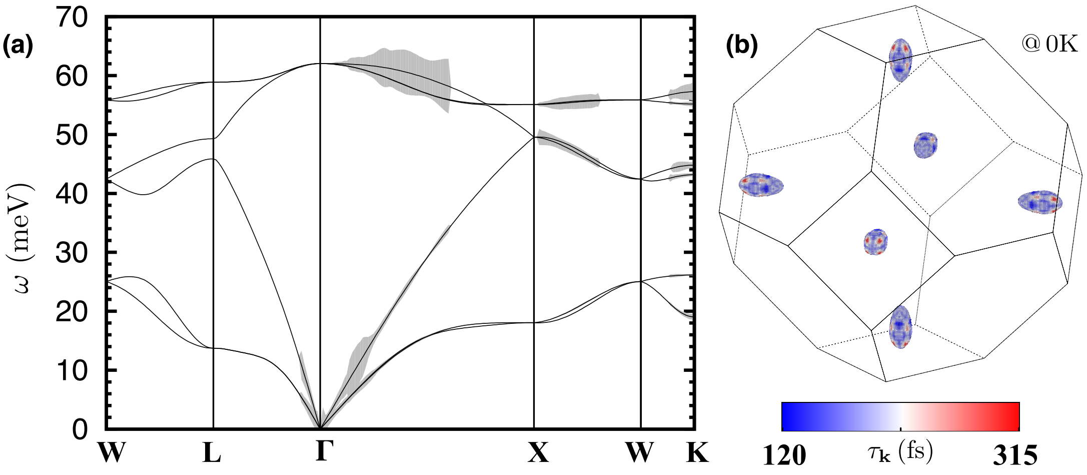

Figure 3.10.: (a) The solid lines show the phonon frequency spectrum in silicon. In the following, the system is n-doped with $E_{\mathrm{F}} = E_{\mathrm{CBM}} +$ 100meV and the Fermi surface consists of 6 small pockets (b). The magnitude of the $\mathbf{q}$-resolved coupling strength for transitions between states in these pockets is given as superimposed linewidth in (a). Due to the selective character of the Fermi surface, some phonons are not able to connect the pockets resulting in a vanishing linewidth, which is directly linked to the nesting function. The color code in (b) shows $\tau_{\mathbf{k}}$ at zero temperature revealing an anisotropical structure at the Fermi surface.

given by the $\overline{\Gamma \mathrm{X}}$ and $\overline{\Gamma \mathrm{L}}$ direction, which can be seen in (a). Here, the **q**-resolved coupling strength $\sum_{\mathbf{k}} \left| g^{\mathbf{q}}_{\mathbf{k},\mathbf{k}+\mathbf{q}} \right|^2$ is shown as superimposed linewidth onto the frequency spectrum. If their is no phonon mediating an initial and final electron state, the coupling strength is zero. Phonons with high energies parallel to [100] exhibits the largest coupling strengths. These originate from either intra- or intervalley scattering since a clear separation with respect to phonon momentum $|\mathbf{q}|$ is not possible because the largest distance within a pocket is larger than the minimal distance between two pockets. Nevertheless, the main contribution stems probably from intervalley transitions since coupling strengths obtained from deformation potentials show, that the coupling is largest for optical g-processes, which are intervalley transitions in [100] direction [62, 63, 127, 134].

The relaxation time is anisotropic and does not reflect the ellipsoidal geometry of the pockets, which is probably due to intervalley transitions between them. Assuming a less doped system with $\epsilon_{\mathrm{F}} = \epsilon_{\mathrm{CBM}} + 20\mathrm{meV}$ only intravalley scattering can take place and $\tau_{\mathbf{k}}$ might feature an ellipsoidal symmetry. Nevertheless, the values of $\tau_{\mathbf{k}}$ are in agreement with results by Poncé *et. al*[110] and Bernardi *et. al*[17].

3.2.2. State-dependent properties away from the Fermi surface in lead

The following section is primarily addressed to the discussion of the coupling constants

$$\lambda_{\mathbf{k}} = 2 \int_0^{\infty} \mathrm{d}\omega \, \frac{\alpha^2 F_{\mathbf{k}}(\epsilon_{\mathbf{k}}, \omega)}{\omega} \quad \text{and} \tag{3.2.4}$$

$$\lambda^{\mathrm{tr}}_{\mathbf{k}} = 2 \int_0^{\infty} \mathrm{d}\omega \, \frac{\alpha^2 F^{\mathrm{tr}}_{\mathbf{k}}(\epsilon_{\mathbf{k}}, \omega)}{\omega} \quad . \tag{3.2.5}$$

$\alpha^2 F^{\mathrm{tr}}_{\mathbf{k}}$ is the **k**-dependent Éliashberg spectral function, where the efficiency factor

$$\eta_{\mathbf{k}} = 1 - \frac{\mathbf{v}_{\mathbf{k}} \cdot \mathbf{v}_{\mathbf{k}+\mathbf{q}}}{v_{\mathbf{k}} v_{\mathbf{k}+\mathbf{q}}} \tag{3.2.6}$$

is added to account for the change of the velocity during the scattering process. Quantities including this factor are therefore refered to transport while quantities without are assigned to spectroscopy.

Spectroscopical properties

Figure 3.11(b) and (c) show the Éliashberg spectral functions along the high symmetry line in lead for the two bands B1 and B2, which cross the Fermi energy. The Éliashberg function basically measures the coupling strength of phonons to a certain electron state. The phonon spectrum is therefore shown in (a). The comparison with experimental data and other calculations, which include spin-orbit interaction, points out the drawbacks of the scalar-relativistic calculation [28, 54]. Three features can be identified. First of all, the absolute value of the phonon bandwidth is ≈ 10% to large. Second, a mode softening at certain points (e.g. X) in the Brillouin zone can not be observed. Third, Kohn anomalies, e.g. along the $\overline{\Gamma \mathrm{K}}$-line, due to Fermi surface nesting are not accounted for. In the end, these features result in an enlarged value of the electron-phonon coupling parameter but do not change the overall behaviour. Additionally, the phonon linewidth $\gamma_{\mathbf{q}}$ is shown superimposed onto the frequencies $\omega_{\mathbf{q}}$. It can be seen that the linewidth is large for high-energy phonons and drops to zero with $\omega \longrightarrow 0$.

Heading back to the spectral functions shown in (b) and (c), the shape of each $\alpha^2 F_{\mathbf{k}}$ is quite similar to the isotropic Fermi surface averaged Éliashberg function given as red line in (d). Two peaks are seen,

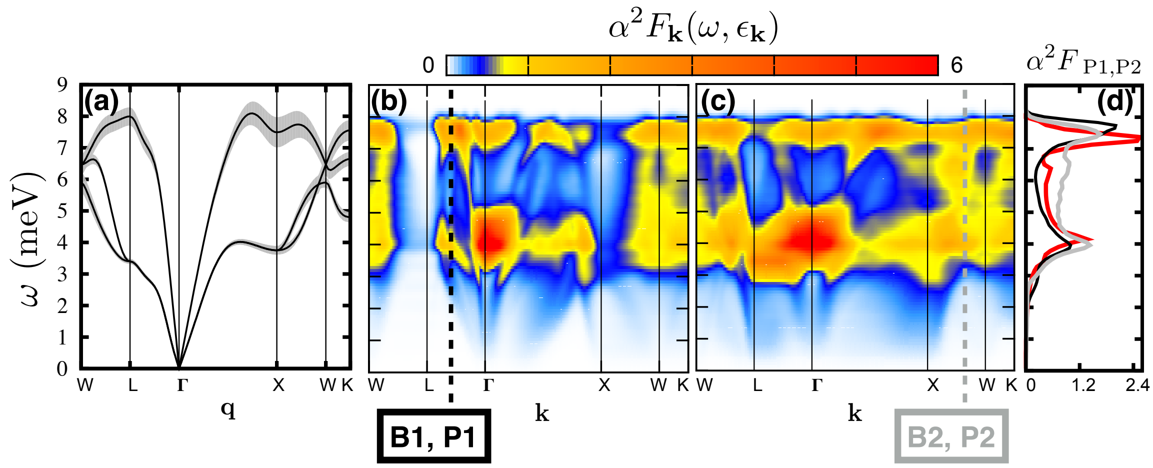

Figure 3.11.: (a) Phonon dispersion curves with superimposed linewidths due to electron-phonon interaction. The maximum width corresponds to ~ 32meV. (b), (c) **k**-dependent Éliashberg spectral function $\alpha^2 F_{\mathbf{k}}(\epsilon_{\mathbf{k}}, \omega)$ for the bands B1 and B2. The colour-code is related to the values of $\alpha^2 F_{\mathbf{k}}$. The states P1 and P2 are highlighted as dashed black and grey lines. (d) $\alpha^2 F_{\mathbf{k}}$ of electron state P1 (black) and P2 (grey) on the Fermi surface. The contributions to the spectral function in P1 arise almost merely from the high-energy phonons, while the involved phonons to the coupling in P2 are more spread in energy. The red line shows the Fermi surface averaged spectral function.

which are more or less distinct from each other. One originates from high-energy phonons with $\omega_{\mathbf{q}} \approx 7-8$meV and the other one arises from flat phonon modes around $3-4$meV. This pattern is even seen at the L point in the band B1, where the scattering phase space, which counts the number of available final electron states, is almost zero. The highest values of $\alpha^2 F_{\mathbf{k}}$ are found around Γ. Here, the electronic band structure favours coupling to phonons with wave vector **q** along the $\overline{\Gamma\mathrm{X}}$ direction. Due to the flat dispersion of these phonons at 3 ... 4meV, their contribution to $\alpha^2 F_{\mathbf{k}}$ is large. The spectral functions of the previously discussed electron states P1 and P2 are highlighted with dashed black and grey lines and shown separately in (d). As already said, both Éliashberg functions provide the two-peak-structure. Nevertheless, $\alpha^2 F_{\mathrm{P1}}$ is dominated by mid- and high-energy phonons with a low dispersion while the contributing phonons to $\alpha^2 F_{\mathrm{P2}}$ are spread in energy. In both cases the coupling to phonons with energy less than 2meV is weak. These characteristics were also found earlier while investigating the matix elements in figure 3.7(a) and explain the anisotropy of each **k**-dependent property like the Éliashberg spectral function , the coupling constant, the linewidth and the relaxation time.

The **k**-dependent coupling constant is shown in fig. 3.12(a). The calculated values along the $\overline{\Gamma\mathrm{L}}$ line are qualitatively in good agreement with data from Sklyadneva *et al.*[126]. The same **k**-dependence is found for B1 as well as for B2. The coupling at the special points P1 and P2 are $\lambda(\mathrm{P1}) = 1.30$ and $\lambda(\mathrm{P2}) = 1.79$. Since $\lambda_{\mathbf{k}}$ is more or less the integrated $\alpha^2 F_{\mathbf{k}}$, the largest values are obtained at the Γ point and the smallest one at the L point. One can see from figure (b), that the shape of $\lambda_{\mathbf{k}}$ and the linewidth $\Gamma_{\mathbf{k}}$ are almost identical at $T = 300$K. Equation 2.1.44 and 3.2.4 are related at higher temperatures due to a similar ω-dependence given by

$$\left[1 + 2n(\omega) + f(\epsilon_{\mathbf{k}} + \omega) - f(\epsilon_{\mathbf{k}} - \omega)\right] \approx \frac{A}{\omega} \quad , \tag{3.2.7}$$

where A is in units of energy. $\Gamma_{\mathbf{k}}$ is 0.211 eV and 0.295 eV for P1 and P2, respectively. The inverse linewidth gives rise to the relaxation time, which is shown in (c). Complementarily to $\lambda_{\mathbf{k}}$ and $\Gamma_{\mathbf{k}}$, largest relaxation times are observed for B1 at L. Vice versa, $\tau_{\mathbf{k}}$ is smallest at Γ due to the strong coupling between electrons and phonons.

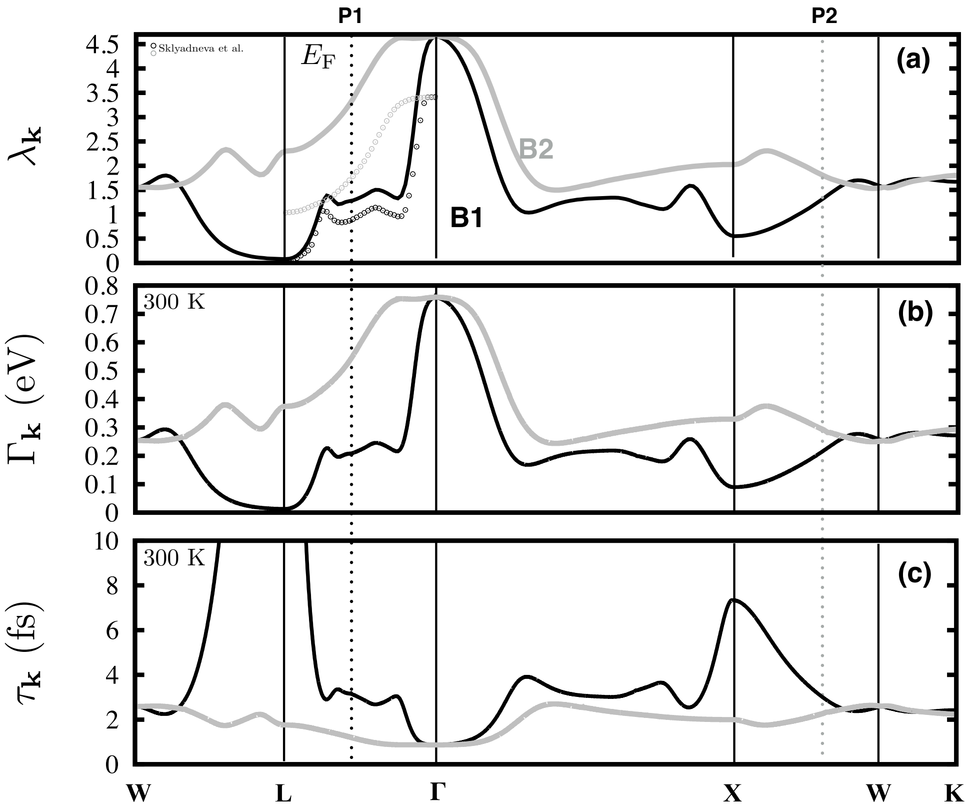

Figure 3.12.: Various $\mathbf{k}$-dependent properties related to the electron-phonon interaction. The black (grey) vertical points indicate the point P1 (P2), where the band B1 (B2) cross the Fermi energy. All quantities in (a)-(c) are calculated via an integration over the Éliashberg spectral function given in figure 3.11(b) and (c). (a) Electron-phonon coupling constant λ_k. (b) Electron linewidth Γ_k at 300K. (c) Electron-phonon relaxation time τ_k obtained from the linewidths in (b). At 300K, τ_k is about 3.15fs and 2.15fs in P1 and P2, respectively.

Transport relaxation time and coupling constant

The influence of the efficiency factor η_k (eq. 3.2.3) onto λ_k and τ_k is shown in figure 3.13. The overall trend, obtained by the spectroscopical properties, does not change drastically when taking the efficiency factor into account (see (a) and (c)).

Nevertheless, certain **k** points favour either effective forward- (↑↑) or backward-scattering (↑↓), depending on the sign of the function $\lambda_\mathrm{k} - \lambda_\mathrm{k}^{\mathrm{tr}}$, which is shown in (b). Thereby, the second arrow indicates the direction of scattering whether the effective orientation of the velocity of all final states relative to the velocity of the initial state is parallel (↑) or anti-parallel (↓). In the end, the arrows shall guide the eyes and the coupling strength λ_k is either enhanced or decreased. *A priori* the type of scattering, which is favoured, is usually not predictable. It can depend on the geometry of the iso-energy surface, the coupling strength, or on a mixture of both of them. A prediction would require a detailed analysis of each scattering event, which is done exemplarily at the highlighted states Y and Z of the band B2 around the high symmetry point X. It turns out that the efficiency factor decreases (increases) $\alpha^2 F_\mathrm{k}$ at lower phonon energies at Y (Z) but keeps $\alpha^2 F_\mathrm{k}$ almost uneffected at higher energies. The resulting transport coupling constant is therefore smaller (larger) and forward (backward)-scattering is favoured. Applying the constant coupling approximation, $\left|g^{\mathrm{q}}_{\mathrm{k,k+q}}\right|^2$ equals unity, shows that the decrease of λ_k at Y due to the efficiency factor is caused solely by the geometry of the iso-energy surface. This does not hold at Z, where the coupling strength itself is more important than the geometry of the iso-energy surface.

Directly at the high-symmetry points, $\lambda_\mathrm{k}^{\mathrm{tr}}$ equals λ_k due to the vanishing velocity at the zone bound-

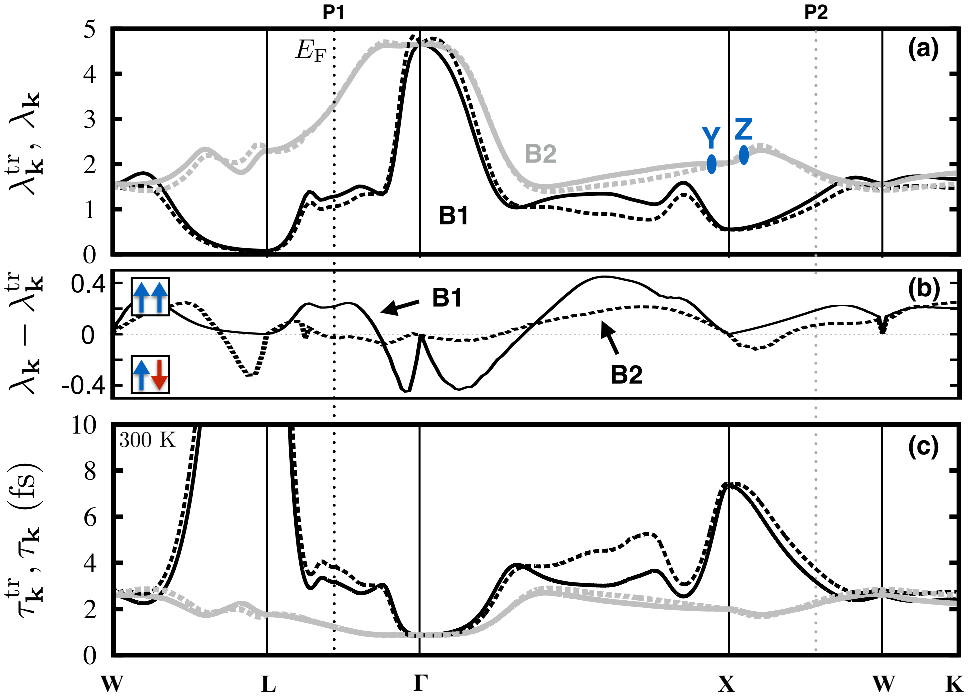

Figure 3.13.: Comparison of **k**-dependent transport properties with their spectroscopical counterparts. The graphical layout is the same as in figure 3.12. (a) Coupling constants $\lambda_{\mathbf{k}}^{\text{tr}}$ (dashed lines) and $\lambda_{\mathbf{k}}$ (solid lines). Y and Z are highlighted **k** points which are discussed in more detail within the text. (b) Difference $\lambda_{\mathbf{k}} - \lambda_{\mathbf{k}}^{\text{tr}}$, at some **k** points either effective forward- (positive, ↑↑) or backward-scattering (negative, ↑↓) is favoured. (c) Relaxation times $\tau_{\mathbf{k}}^{\text{tr}}$ (dashed lines) and $\tau_{\mathbf{k}}$ (solid lines) at 300 K.

aries.

Similar to the coupling constants, the transport relaxation time differs only slightly from its spectroscopical counterpart. The increase of $\tau_{\mathbf{k}}^{\text{tr}}$ compared to $\tau_{\mathbf{k}}$ is about 21% and 8% at P1 and P2 at the Fermi energy.

3.2.3. From state- to energy-dependent relaxation times and other approximations

The implementation of the relaxation time into transport calculations is usually done within a constant relaxation time approximation (cRTA) with one specific value, which is taken from a fit of experimental data. Another possibility is given by equation 3.2.1 to obtain τ at least in the high-temperature limit. Since the computational power increased over the last decades detailed investigations of the electron-phonon interaction on an *ab initio* level become possible. The consideration of τ shifts from a simple parameter to a truly calculated quantity. Here, the focus is on the evaluation of an energy-dependent relaxation time (ERTA) with $\tau_{\mathbf{k}}$ as starting point, which is a step beyond the cRTA . Nevertheless, transport calculations explicitly including $\tau_{\mathbf{k}}$ are also performed recently [79].

The used approach is shown in figure 3.14 and demonstrates the way from $\tau(\epsilon)$ to $\tau(\mathbf{k})$ at the temperature $T = 50$K. The open circles in (a) correspond to a relaxation time in state **k** and its related energy $\epsilon_{\mathbf{k}}$. Subsequently, the arithmetic mean value (AMV) of the scattering rate is computed. Its in-

Table 3.1.: Used smearing values in the gaussians to smoothen the calculated arithemtic mean values of the relaxation time. Smearing is given in meV.

segment	10K	50K	100K	300K	600K
I	2	2	20	50	50
II/III	50	50	50	50	50

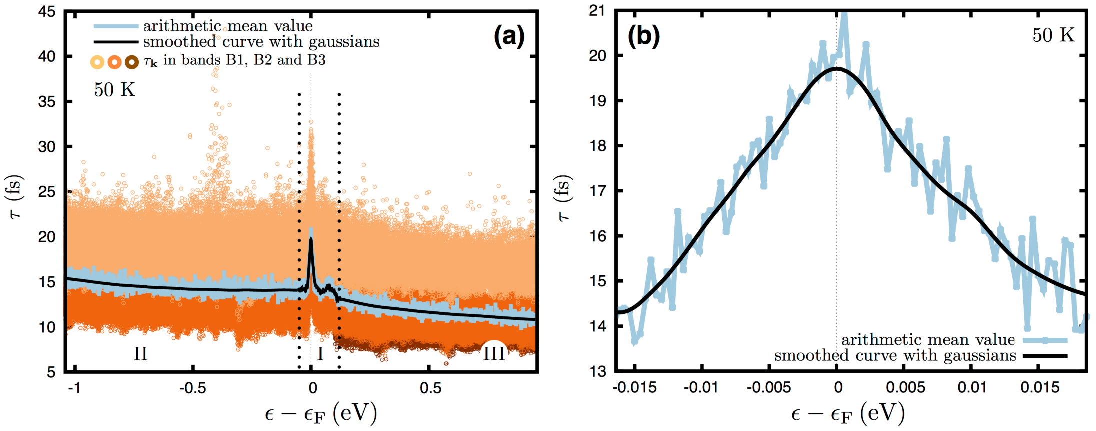

Figure 3.14.: (a) State-dependent relaxation times $\tau_{\mathbf{k}}$ for the bands B1 and B2 as well as the next higher band are shown (open circles). Starting from $\tau_{\mathbf{k}}$, the energy-dependent $\tau(\epsilon)$ is calculated as a arithmetic mean value (light blue line). Afterwards an adaptive smearing method (black line) was applied. (b) A more detailed picture of the energy-dependent relaxation time at 50K with a smaller energy window around the Fermi energy to show the jagged arithmetic mean value τ^{AMV}.

verse quantitiy, $\tau_{\mathrm{AMV}}(\epsilon)$, is shown as a solid light blue line. However, the result depends on the width of the energy interval used to calculate the AMV and is rather jagged. This does not affect the results of the electrical conductivity but strongly influences the calculation of the thermopower. The last is very sensitive to the slope of the transport distribution function (eq. 2.2.30) around the Fermi energy and needs to be as smooth as possible. To overcome this issue, an adaptive smearing method is used to smooth out the arithmetic mean values given as solid black line in (a). The smearing is done with gaussians of different widths, which are manually related to the slope of τ_{AMV}. A distinction between three segments was made. One, which is labeled as II, includes the peak at the Fermi energy and the little bumb above. The other two consist of the remaining parts below and above ϵ_F and are labeled as I and III. The main peak of $\tau(\epsilon)$ at ϵ_F is shown in (b) at a smaller energy scale to justify the gaussian smoothing. In a last step, a spline interpolation is used, which does not change the result at all and is therefore not shown in the figure. The smearing values used at each temperature in the gaussians are given in tabel 3.1.

The final energy-dependent relaxation time at each temperature is shown in figure 3.15(a). Apart from the Fermi energy, the factor $\left[1 + 2n(\omega) + f(\epsilon_{\mathbf{k}} + \omega) - f(\epsilon_{\mathbf{k}} - \omega)\right]$ in equation 2.2.20 determines the magnitude of τ due to the temperature-dependence of the distribution functions n and f. There is no significant impact on the functional behaviour of $\tau(\epsilon)$. At ϵ_F however, the factor is responsible for the peaked structure at low temperatures. The peak originates from the decreasing scattering phase space for phonons at temperatures below the Debye temperature, $\Theta_D \approx 95$K, as phonons with larger wave vectors are frozen out and the number of scattering events is drastically reduced. Hence, width and slope are different at every temperature. The little bumb around 100 meV above ϵ_F marks the bottom of the next higher band and the relaxation time decreases above this energy due to the additional

Table 3.2.: Overview of the used approximations of the **k**-dependent relaxation time to calculate the electrical conductivity and the thermopower.

name	ϵ-dependent	T-dependent	basis	band-resolved
τ^{cRTA}	∘	•	$\tau(\epsilon_F)$	∘
$\tau^{\mathrm{bd\text{-}cRTA}}$	∘	•	$\tau(\epsilon_F)$	•
τ^{DOS}	•	•	DOS and $\tau(\epsilon_F)$	∘
$\tau(\epsilon)$	•	•	$\tau_{\mathbf{k}}(\epsilon_{\mathbf{k}})$	∘

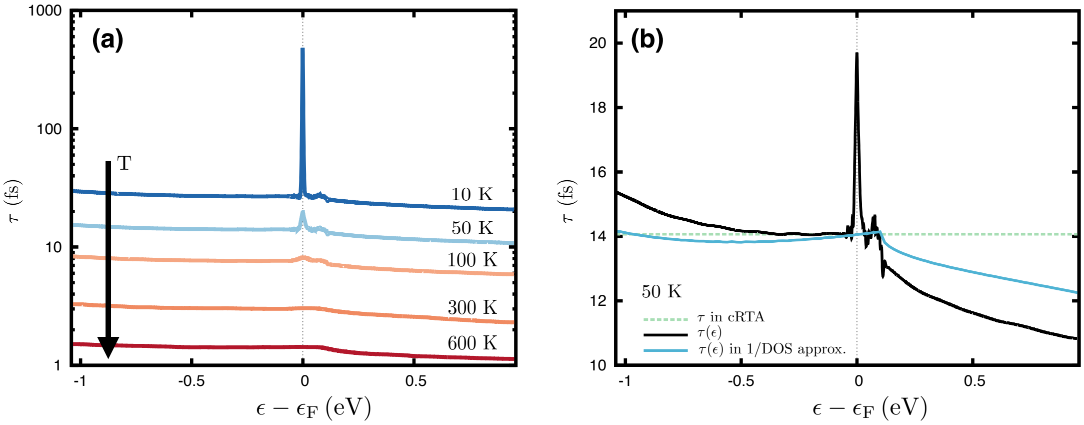

Figure 3.15.: (a) Energy-dependent relaxation times are shown for several temperatures from 10K (blue line) to 600K (red line). τ is decreasing with increasing temperature as indicated by the black arrow. The peak at ϵ_F is characteristic for temperatures below Θ_D and originates from a freeze-out of long phonon wave vectors and a decreased scattering phase space. (b) Overview of some approximations applied to the relaxation time at 50K to calculate transport properties. Each approximated τ has a different slope around ϵ_F changing subsequently the slope of the transport distribution function, which directly influences the calculated thermopower.

scattering channels for the electrons.

Finally, a comparison between different types of relaxation time approximations and their influence on the electrical conductivity and thermopower is possible. The types are classified in tabe 3.2 and some of them are shown in figure 3.15(b). The values of τ^{cRTA} and $\tau^{\text{bd-cRTA}}$, which is a band-dependent constant relaxation time approximation, are estimated from $\tau(\epsilon)$ at the Fermi energy for each temperature separately. Another commonly used approximation includes the density of states DOS as

$$\tau^{\text{DOS}}(\epsilon, T) = \frac{A(T)}{\text{DOS}(\epsilon)} \quad . \tag{3.2.8}$$

$A(T)$ is chosen in this way, that the condition $\tau^{\text{DOS}}(\epsilon_F, T) = \tau(\epsilon_F, T)$ is fullfilled.

3.2.4. Transport properties including electron-phonon interaction

The obtained energy-dependent relaxation time allows for the calculation of the electrical conductivity σ and the thermopower S under the influence of the interaction of electrons and phonons. Both quantities are calculated with the help of the generalized transport coefficients, which are slightly different defined as in equation 2.2.31. To be more precise, the state-dependence of the relaxation time τ_k in equation 2.2.30 is shifted into an energy-dependence. It therefore shows up in the energy integration as $\tau(\epsilon)$. The generalized transport coefficients $\underline{\underline{\mathscr{L}}}^\alpha$ and the transport distribution function $\underline{\underline{\Sigma}}$ finally reads as

$$\underline{\underline{\mathscr{L}}}^\alpha(\mu, T) = \int d\epsilon\, \underline{\underline{\Sigma}}(\epsilon)\tau(\epsilon)(\epsilon_k - \mu)^\alpha \left(-\frac{\partial f_k^0(\mu, T)}{\partial \epsilon}\right) \quad \text{and} \tag{3.2.9}$$

$$\underline{\underline{\Sigma}}(\epsilon) = \frac{1}{(2\pi)^3} \oint_{\epsilon=\epsilon_k} \frac{dS}{\hbar|\mathbf{v}_k|} \mathbf{v}_k \circ \mathbf{v}_k \quad . \tag{3.2.10}$$

Figure 3.16(a) shows the electrical conductivity calculated within the various relaxation time approximations introduced in the previous section. Qualitatively, the agreement with published experimental and theoretical data is good. A quantitativ analysis, however, in terms of a fitted power law is not possible due to the low amount of calculated data points but it seems reasonable that $\sigma(T) \approx T^{-1}$ holds

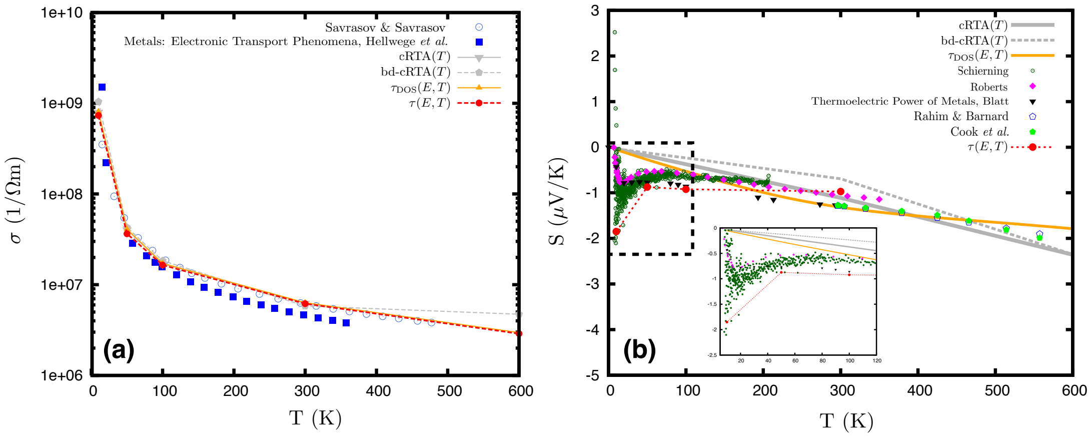

Figure 3.16.: Calculated electrical conductivity σ (a) and thermopower S (b) of lead. The electron-phonon interaction is included within several approximations (lines with points). The results of σ are compared to experimental[14] and theoretical[115] data (closed squares and open circles). S is compared to a variety of measured values (different types of points) [20, 25, 112, 114, 118]. While the relaxation time approximations can not reproduce the experimental data at low temperatures, the energy- and temperature-dependent τ describes them very well.

for temperatures far above the Debye temperature. The comparison with respect to the used approximations reveals basically no difference in the conductivity in the temperature range $10\ldots300$K and even the simple temperature-dependent cRTA yields acceptable results. The reason is given by the integrand of equation 3.2.9. The electrical conductivity is proportional to the zeroth moment of the TDF, $\sigma(\mu, T) \approx \mathscr{L}^{(0)}$ and the important integration range is determined by the energy width of the derivative of the Fermi-Dirac distribution function, which is in the order of $k_B T$. Eventually, there is almost no difference in the integrand around ϵ_F for each of the applied relaxation time approximations.

The situation is different for the diffusive thermopower. It is $S \propto \mathscr{L}^{(1)}(\mathscr{L}^{(0)})^{-1}$ and the specific functional behaviour of Σ nearby ϵ_F is crucial. Depending on the chosen approximation $\tau^{\text{cRTA}}(T)$, $\tau^{\text{bd-cRTA}}(T)$, $\tau^{\text{DOS}}(E, T)$ or $\tau(E, T)$ the slope of Σ changes, which directly transfers to the value of the thermopower. In the first two cases, the slope of $\text{TDF}(\epsilon)$ does not change with temperature, only the absolute values are affected by T. The obtained thermopower within these approximations is almost linear in temperature and can not reproduce the experimental data for $T < \Theta_D \approx 95$K, which are shown in figure 3.16(b). Nevertheless, they fit quite well at temperatures far above Θ_D, which is expected since all additional features in $\tau(E, T)$ around the Fermi energy are lost anyways at higher temperatures and approximations considering the whole phonon spectrum are reliable because all phonon states are occupied.

If the energy-dependent relaxation time $\tau(E, T)$ is used, the thermopower is enhanced at $T < \Theta_D$, which describes the experimental data very well. Since the standard approach for solving the Boltzmann equation with electron-phonon interaction is used, which says that phonons are treated within their equilibrium state[143], the experimentally observed enhancement of S is not or at least not solely caused by the phonon-drag effect. At least in low-doped semiconductors, the phonon-drag effect is usually the only explanation for an increased thermopower. Nonetheless, the phonon-drag contribution S^{phd} might be only one part of the enhanced thermopower in metals. In fact, the peaked structure of $\tau(E, T)$ at low temperatures as a result of an explicit description of the electron-phonon interaction gives rise to an additional thermopower even for the diffusive part, which qualitatively reproduces the measured thermopower. It additionally fits the general observation of an enhanced absolute thermopower, $S^{\text{e-ph}} \propto S(1 + \lambda)$, at low temperatures.

3.3. The real part of the electron self-energy and its impact on electron properties

After the discussion of the influence of the imaginary part of the self-energy onto the electrical conductivity and thermopower, the upcoming chapter is about the impact of the real part of the self-energy.

First, the appearence and the calculation of the characteristic *kinks* in the band structure due to electron-phonon coupling are explained. It is shown, that *band-splitting* can occur in dependence on the coupling strength, temperature, phonon band width and electron energy. Afterwards, the electrical conductivity and thermopower is calculated. These investigations are made for a model system. The second part addresses the renormalization of electron states in Pb. Possible issues due to the calculation of transport properties are discussed, which indicates the need of large computational effort for metallic systems with a small phonon band width.

3.3.1. Effects of the renormalization on the basis of a free electron model

Physical meaning of the real and imaginary part of the electron self-energy

Throughout this chapter, the phonons are primarily treated within an Einstein model with the single characteristic phonon frequency ω_E. The according Éliashberg spectral function is given by

$$\alpha^2 F_E(\omega) = \frac{1}{2}\lambda\omega_E\delta(\omega - \omega_E) \quad , \tag{3.3.1}$$

where λ is the electron-phonon coupling constant. Subsequently, the imaginary part of the self-energy Σ'' is calculated via eq. 2.1.44 and the real part of the self-energy Σ' is obtained by a Kramers-Kronig transformation. The result for the parameter set $\omega_E = 30\text{meV}$ and $\lambda = 0.5$ are shown in figure 3.17 for a low (10K) and a high temperature (300K). One has to keep in mind, that the self-energy is usually $\mathbf{k}$-dependent and the energy ω is the quasi-particle energy of the interacting electron at $\mathbf{k}$ with respect to its bare energy value $\epsilon_{\mathbf{k}}$.

Now, consider the low temperature case for an electron at the Fermi surface and $\omega > 0$. The imaginary part of Σ, which is directly proportional to the linewidth Γ, is nearly zero for small energies since the electron states below the Fermi energy are almost fully occupied due to the Fermi-Dirac distribution function and scattering from above ϵ_F into these states via emission of a phonon is suppressed. On the other hand, the absorption of a phonon is allowed since the states above ϵ_F are not occupied. If ω is larger than ω_E, the emission of phonons becomes possible and Σ'' increases drastically. The real

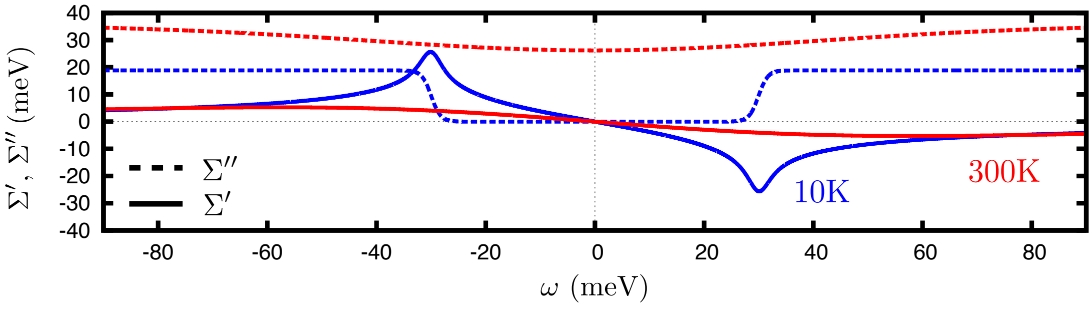

Figure 3.17.: Real (Σ', solid line) and imaginary (Σ'', dashed line) part of the electron self-energy $\Sigma(\omega)$ for an Einstein model. The Einstein frequency is $\omega_E = 30\text{meV}$ and the coupling constant is set as $\lambda = 0.5$. The peak in Σ' around the Einstein frequency is clearly seen in the low temperature regime (blue) but washed out for high temperatures (red).

part of the self-energy describes the effective gain ($\omega < 0$) or loss ($\omega > 0$) of the electron energy $\epsilon_{\mathbf{k}}$ due to scattering with phonons. The maximal energy transfer is obtained at $T \longrightarrow 0$ and given by the largest phonon energy, which is ω_{E} in this case. The largest values of Σ' at each temperature are found around ω_{E}, which coincides with the jump in Σ''.

The description of phonons with the Debye model or more realistically with a fully calculated phonon spectrum does not change the overall behaviour of Σ' and Σ''. Therefore, both phonon models are used to fit linewidths and band structures obtained from experiments, which enables the extraction of Σ'' and Σ' from measurements and additionally yields information about the phonon spectrum [59].

Differences in Σ'' and Σ', which arise from the modeled phonon spectrum and a real phonon spectrum, can be seen at very low temperatures only (compare fig. 3.17 and fig. 3.24(b)). At higher temperatures, all special features originating from the phonon dispersion are lost anyway. Especially the imaginary part becomes almost constant at elevated temperatures, which is directly linked to the T-dependence of the relaxation time $\tau(\epsilon)$ shown in figure 3.15.

Band structure renormalization

As stated earlier, the renormalization is performed by finding the poles in the spectral density $\mathscr{A}$ in eq. 2.1.47 in the limit of vanishing damping, which yields the following equation at each $\mathbf{k}$ point

$$\omega = \epsilon_{\mathbf{k}} + \Sigma'(\omega, T) \quad . \tag{3.3.2}$$

This equation is solved self-consistently for a free electron model with quadratic dispersion $\epsilon_{\mathbf{k}} \propto \mathbf{k}^2$ and a modeled semiconductor with a parabolic band dispersion as well. The results are shown in figure 3.18 (a)-(c) and 3.19, respectively. The dashed horizontal line in each figure marks the Einstein frequency, where so-called *kinks* occur at low temperatures. These kinks are characteristic for the renormalization of electron states due to electron-phonon interaction. Their existence and shape depend on the band structure and the Fermi energy, which is easy to modify using a model system enabling a qualitative investigation of the effects due to the renormalization. In each case, $\epsilon_{\mathbf{k}}$ (black line) is decreased lying above the Fermi energy and increased lying below it, which is in agreement with Σ'. In the following a distinction between both electron systems is made starting with the free electron model in fig. 3.18.

Probably the most common case is shown in (c), where the band bottom ϵ_{min} is far away from ω_{E} and kinks occur at $\pm\omega_{\mathrm{E}}$. Directly at these energies, the velocity drops to zero in the limit $T \longrightarrow 0$. As mentioned before, the band bottom is sligthly shifted. Besides this theoretical calculation, the kinks are also accessible in an experiment, which enables the estimation of the band structure. This is usually done with *angle-resolved photoemission spectroscopy* (ARPES) [59, 70]. Another technique (*Fourier transform scanning tunneling spectroscopy*) was recently used to investigate the parabolic surface state in Ag(111), which reveals the kinks in its dispersion due to the electron-phonon coupling [49] shown in (d). If the difference between ϵ_{min} and ω_{E} is to small, kinks are not formed and the energy shift in ϵ_{min} is very large (a). As an intermediate case, it is possible that the band will split up (b). Whether this happens or not depends strongly on the combination of coupling strength, temperature, band structure, phonon band width and Fermi energy. One has to keep in mind, that the term *band-splitting* might be misleading, since the electron energy is not well defined in an interacting electron system, where the spectral function has to be used rather than the band structure to investigate electronic properties. To justify the application of the Boltzmann formalism, which is used to calculate the electrical conductivity and thermopower, the transport calculations will be restricted to sytems in which no splitting occurs. In

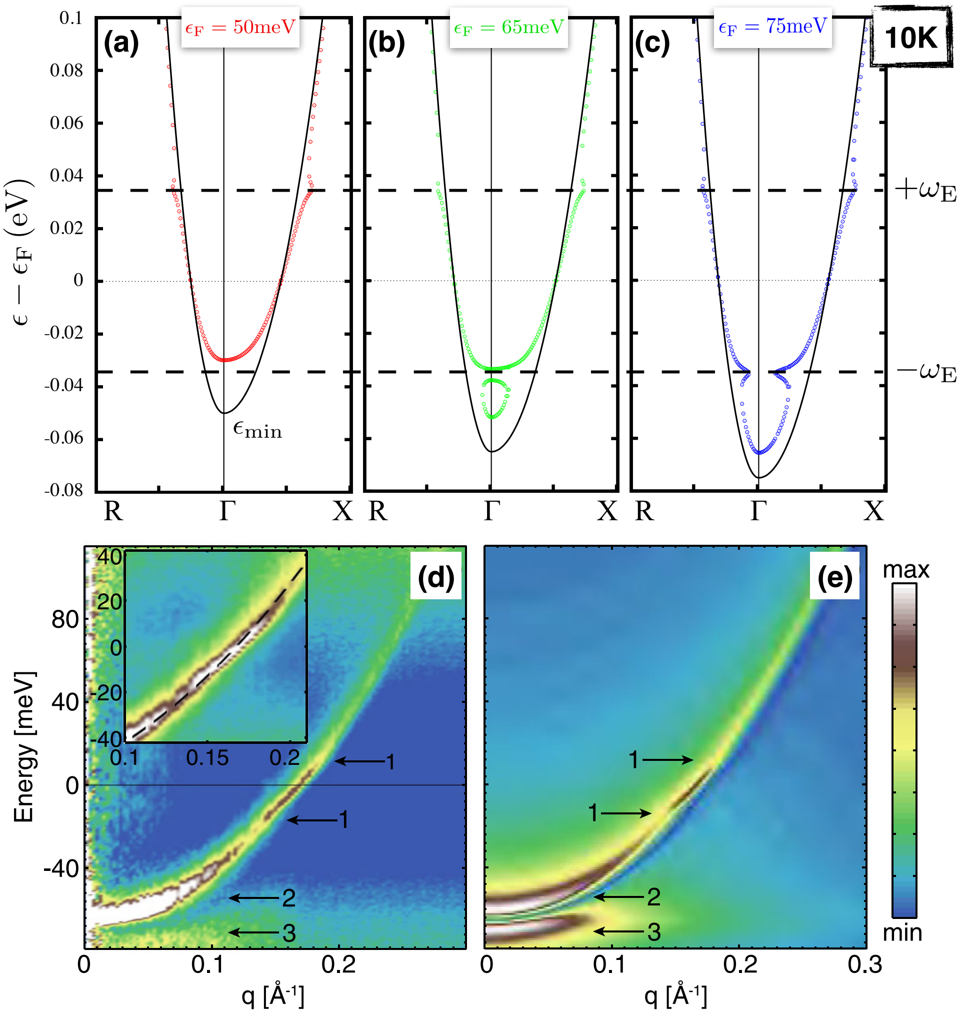

Figure 3.18.: (a)-(c) Renormalized band structure at $T = 10\text{K}$ for a free electron model with a parabolic band dispersion for various Fermi energies. The energy of the renormalized states are shown as dots while the bare state energies are given as black line. The phonons are treated in an Einstein model with $\omega_E = 35\text{meV}$. The coupling constant is set to $\lambda = 0.5$. Qualitatively, the band bottom ϵ_{min} increases in energy towards ϵ_F. Additionally, so-called *kinks* occur at the Einstein frequencies $\pm\omega_E$, which are characteristic for the renormalization due to electron-phonon interaction. Far away from ω_E, the renormalized band structure fits the bare one. If the band bottom is related to ω_E in a special way, a band splitting occurs at ω_E (b). (d) Measured spectral function of the parabolic surface state in Ag(111) at 4.2K. (e) The calculated spectral function reveals kinks around the obtained Debye frequency (1). Figure (d) and (e) were taken from a publication from Grothe *et al.* [49].

this scenario, the interacting electron system can be investigated within the band structure picture.

Going from the free electron model to the p-doped semiconductor reveals the same qualitative effects due to the renormalization. Figure 3.19 shows three semiconductors with the same Fermi energy but varying band gaps ϵ_{gap} from 50meV to 150meV. One can clearly see, that kinks appear at $-\omega_E$. As before, the electron energies still shift towards ϵ_F. As a result of the band-splitting electron states occur in the band gap, which are pinned around ω_E. The decrease of the renormalized band gap E_{gap} compared to the bare band gap is therefore rather large. If no band-splitting occurs, E_{gap} can be equal (b) or larger (c) than ϵ_{gap}. Electron states far away from ϵ_F and ω_E are less affected by the electron-phonon interaction and their renormalization is weak, which is the reason for the increasing band gap. Related to the shown example, the difference $\Delta\epsilon_{gap} = \epsilon_{gap} - E_{gap}$ is about 3meV in the narrow gap semiconductor (c). This value increases up to 6meV for a large gap semiconductor with $\epsilon_{gap} = 1.2\text{eV}$ (not shown). The influence of the temperature is shown in figure (d). The valence band maximum is almost unaffected by the renormalization, which results in total in a decrease of the band gap by $\Delta\epsilon_{gap} = -3\text{meV}$. In 2010,

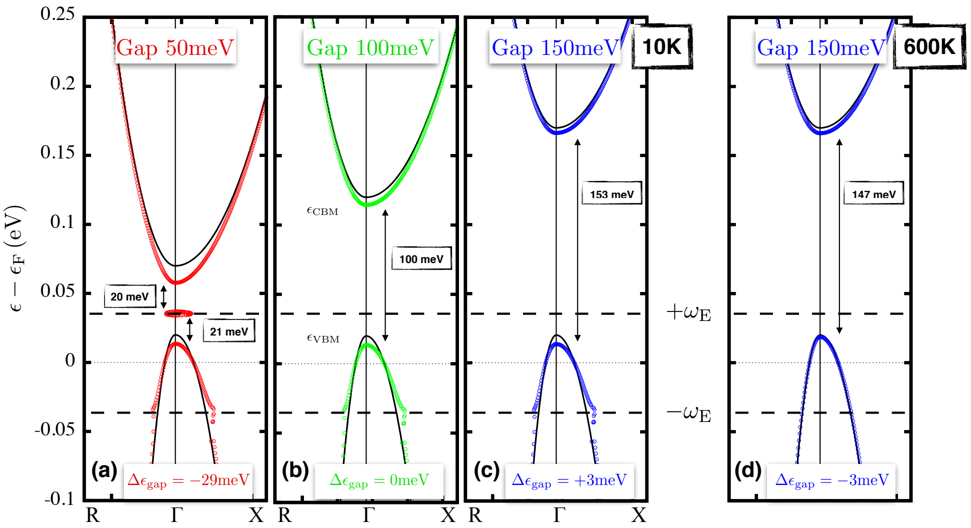

Figure 3.19.: (a)-(c) Renormalized band structure at $T = 10$K for a modeled p-doped semiconductor with varying band gap. The style of the figure and parameters are the same as in fig. 3.18. The valence band maximum ϵ_{VBM} and the conduction band minimum ϵ_{CBM} decreases in energy towards the Fermi energy. A band-splitting can occur as well (a). Depending on the gap size, the renormalized band gap can be smaller, equal or even larger than the bare band gap. The difference is given as $\Delta\epsilon_{\mathrm{gap}}$ in each figure. (d) Same as (c) but at $T = 600$K. The renormalized band gap is smaller than the bare bare band gap.

Giustino *et al.* calculated the zero-point band gap renormalization in diamond with *ab initio* methods, which includes the Fan self-energy and the Debye-Waller term in $\Sigma_{\mathbf{k}}$ as introduced in section 2.1.2, and showed that the band gap decreases with increasing temperature [44]. Very roughly spoken and bearing in mind that the model presented in this work and the assumptions for the phonon spectrum and the the electron-phonon coupling are very simple, the overall trend for $\epsilon_{\mathrm{gap}}(T)$ is reproduced. Apart from that, the kinks disappear at high temperatures as seen in figure (d).

As mentioned before, the occurence of a band-splitting depends on a variety of properties. The solution of the renormalization condition (eq. 3.3.2) is illustrated in fig. 3.20 for the free electron model introduced in fig. 3.18. The number of solutions depends on the energy of the not-renormalized state $\epsilon_{\mathbf{k}}$. Three cases are possible: First, the condition is fullfilled by one solution (red and blue line) and no splitting occurs. The same holds for the case of two solutions, which creates a touching point (not

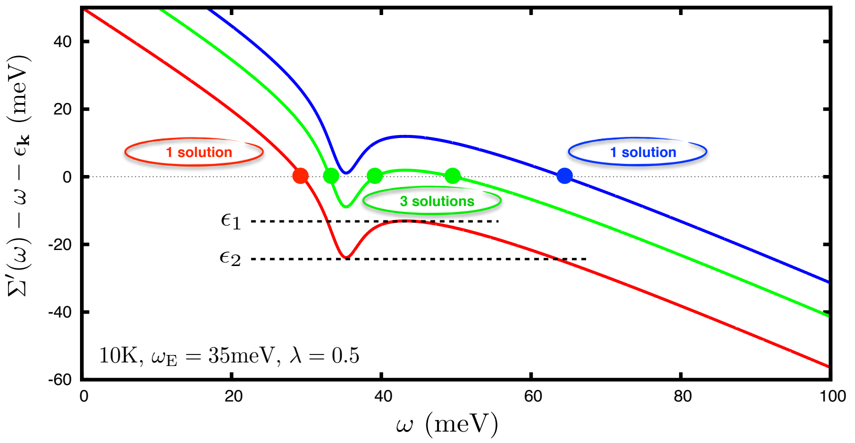

Figure 3.20.: (a) Graphical solution of the renormalization condition $\Sigma'(\omega) - \omega - \epsilon_{\mathbf{k}} = 0$. Besides the renormalization itself, it can be used for the estimation whether a band-splitting occurs or not. To link the condition to figure 3.18, the electron state is chosen to be the band minimum at Γ with the energy $\epsilon_{\mathbf{k}} = \epsilon_{\mathrm{min}}$. If the condition is fullfilled by one solution (red and blue line), the renormalization is of type (a) or (c) in figure 3.18. If there are three solutions (green line), the renormalization leads to a splitting as shown in fig. 3.18(b). The energies ϵ_1 and ϵ_2 are the energy boundaries for this region.

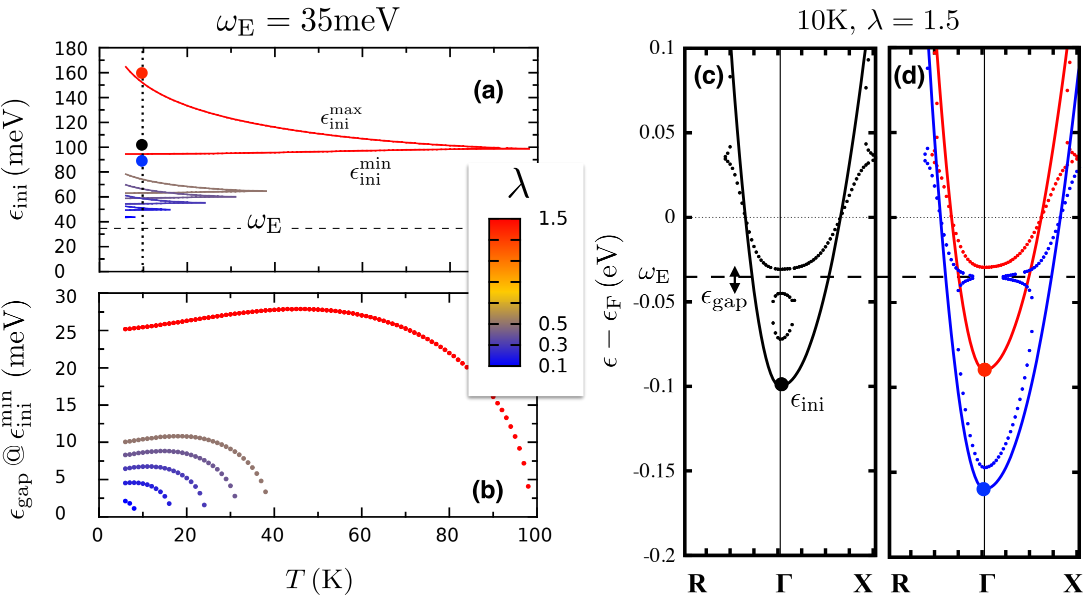

Figure 3.21.: (a) Guide to find band-splitting with respect to temperature, coupling strength and initial electron energy ϵ_{ini} as explained in figure 3.20 and the text. Each coloured line-pair corresponds to one coupling constant λ. In this example, **k** is restricted to the Γ point but the same analysis can be done at every **k** point. If ϵ_{ini} is inside (outside) the confined region given by the line-pair a band-splitting occurs (does not occur). Both cases are shown in (c) and (d) for $T = 10\mathrm{K}$ and $\lambda = 1.5$. All ϵ_{ini} are shown as large points and correspond to the points in (a). The obtained energy gap ϵ_{gap} for $\epsilon_{\mathrm{ini}} = \epsilon_{\mathrm{ini}}^{\mathrm{min}}$, which is the lower line of the line-pair, is shown in (b). The example with the parameter choice $\lambda = 1.5$ and $\omega_{\mathrm{E}} = 35\mathrm{meV}$ is not physical due to $\Sigma'_{\mathrm{max}} > \omega_{\mathrm{E}}$ but easier to visualise and is therefore used to explain the guide.

shown). Last, if the condition is true for three solutions, the band splits (green line). Quantitatively, this region is confined by ϵ_1 and ϵ_2 as indicated in the figure. ϵ_2 is calculated as $\epsilon_2 = \Sigma'_{\mathrm{max}} + \omega_{\mathrm{E}}$ but ϵ_1 can be obtained only visually as long as Σ' is not known as an exact functional expression.

The above analysis can be applied to find regions in the band structure, where band-splitting may occur. If one uses an isotropic self-energy as done throughout this chapter, a numerical scan with respect to the coupling constant λ, temperature T and electron energy $\epsilon_{\mathbf{k}} = \epsilon_{\mathrm{ini}}$ can be performed. Such a guide is shown in figure 3.21 (a) for the free electron model introduced earlier. For a fixed coupling strength, the coloured line pair marks the energy range $[\epsilon_{\mathrm{min}}, \epsilon_{\mathrm{max}}]$ for ϵ_{ini} in which the band splits with respect to T. Figure (c) shows the renormalized band structure at 10K and $\lambda = 1.5$ for ϵ_{ini} within the energy range while (d) shows the other case. The coloured points in (a), (c) and (d) match each other. The emerging energy gap ϵ_{gap} for a splitted band is largest for $\epsilon_{\mathrm{ini}} = \epsilon_{\mathrm{ini}}^{\mathrm{min}}$, which coincides with the lower line of each line pair. Its values are given in (b) revealing that ϵ_{gap} is not maximal at the lowest temperatures, which one might expect. As a remark, the parameter choice $\omega_{\mathrm{E}} = 35\mathrm{meV}$ and $\lambda = 1.5$ is not physical due to $\Sigma'_{\mathrm{max}} > \omega_{\mathrm{E}}$ and the largest possible coupling constant in this model is $\lambda \approx 0.5$ for the chosen Einstein frequency. However, the visualisation is more difficult in this case since the effect is weaker and the larger coupling was used to explain the guide.

As a general observation, a band-splitting is found predominantly for small phonon energies, i.e. $\omega_{\mathrm{E}} < 100\mathrm{meV}$, since otherwise the coupling constant has to be extremely large ($\lambda > 2$). This tendency might be valid for real systems as well. Obviously, the presented scheme can be adapted to any sort of self-energy meaning that it does not matter whether Σ' is obtained from a model system, an isotropic Éliashberg function of a real system, calculated as $\Sigma'_{\mathbf{k}}$ at each **k** point separatly or obtained from experiment.

Impact of the renormalization onto transport properties

Even if the band structure seems to be rather unaffected by the renormalization due to electron-phonon interaction, its impact is clearly seen in quantities like the density of states (DOS) or the transport distribution function (TDF), which is shown in figure 3.22. To be consistent with the previous analysis in this chapter, the electron system is supposed to be free electron like with a quadratic band dispersion. Again, the phonons are treated within an Einstein model with ω_E = 35meV and the coupling constant is $\lambda = 0.5$.

The system is doped with half an electron and the chemical potential is accordingly calculated at every temperature. Hence, the integrated DOS, which is shown in the inset in (b), are equal at ϵ_F. The Fermi surfaces at each temperature are equal as well, which is expected due to the Luttinger theorem [84]. It states, that the Fermi surface does not change whether the system is considered to be interacting or non-interacting.

The density of states and the squared velocity v^2 are almost unaffected at 1000K (red line) since the renormalization of the electron states is very weak. The only noticeable is, that the band bottom is slightly shifted. Since the transport distribution function is roughly estimated by the product of DOS and v^2, no effect due to electron-phonon interaction is seen there as well.

At 10K (blue line), however, the changes in the DOS, v^2 and TDF are significant. The density of states exhibits Van Hove singularities at $\pm\omega_\mathrm{E}$ since the kinks force a horizontal dispersion with vanishing velocity at these energies. In between, v^2 is decreased, which is in agreement with the expected reduction of the velocity at the Fermi energy by the factor $(1 + \lambda)$ [48]. According to the changes in the velocity, the DOS increases for $\epsilon \leq |\omega_\mathrm{E}|$ due to the flat dispersion. The inverse statements hold for

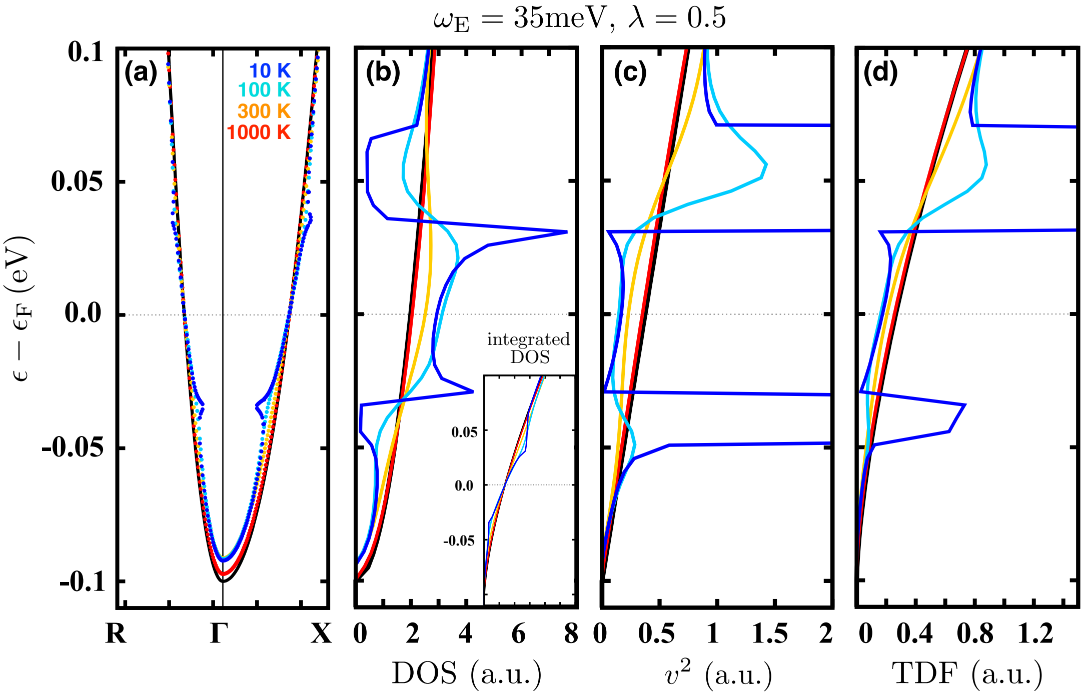

Figure 3.22.: (a) Renormalized band structures (colored dotted lines) for a free electron model at different temperatures. The bare dispersion and other quantities related to it in (b)-(d) are shown as solid black line. (b) Density of states (DOS). Singularities occur at low temperatures due to the horizontal dispersion at ω_E = 35meV. At each temperature, the density of states is enhanced at the Fermi energy but decreased at $\epsilon \lesssim -\omega_\mathrm{E}$ and $\epsilon \gtrsim \omega_\mathrm{E}$. The inset shows the integrated DOS, which is equal at ϵ_F. (c) Squared group velocity v^2. At each temperature, v^2 is decreased at ϵ_F compared to v^2 of the bare dispersion. At low temperatures, the velocity drops to zero directly at ω_E. (d) Transport distribution function (TDF), which is roughly given by DOS × v^2. Comparing with (b) and (c), one can see that the TDF mimics the behaviour of the squared velocity.

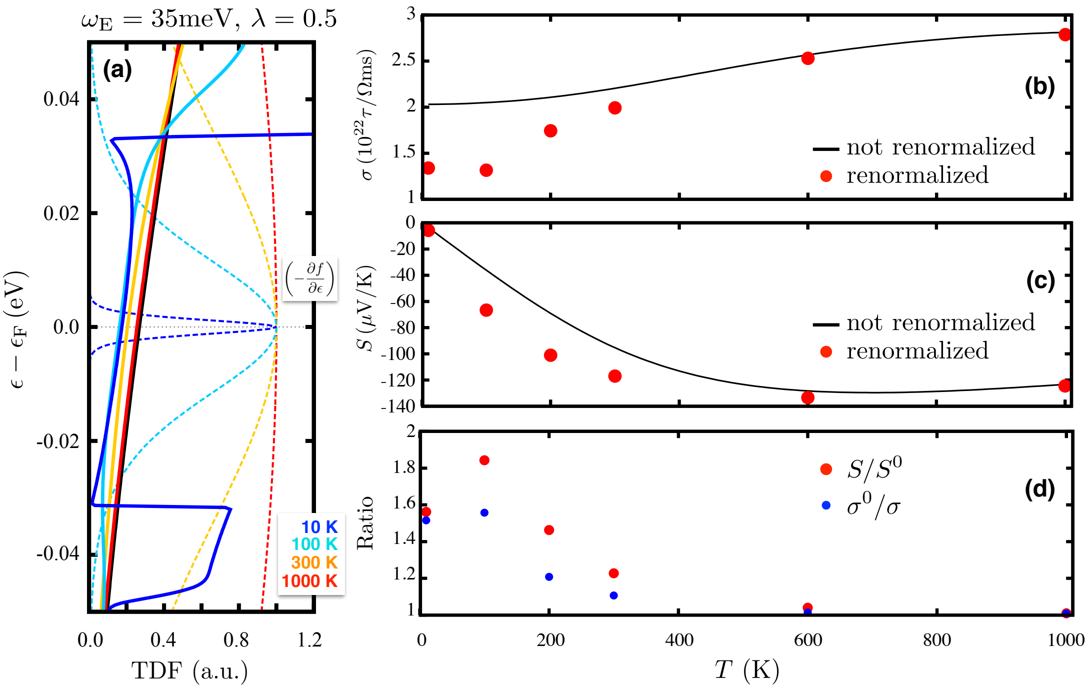

Figure 3.23.: Transport properties of the renormalized free electron model shown in figure 3.22. (a) Transport distribution function as shown in fig. 3.22(d). The additional dashed lines show the derivative of the Fermi-Dirac distribution function which enters the transport integral. The maximal value of each function is scaled to 1. (b) The electrical conductivity σ of the renormalized states (red points) is decreased at lower temperatures compared to σ of the free electron model (black line), which is directly related to the smaller TDF around the Fermi energy. (c) The thermopower S is enhanced at lower temperatures and its ratio S/S^0 is shown in (d), where S^0 is the thermopower of the non-interacting system. The increase is up to 80% and mainly related to the decreased electrical conductivity. A detailed explanation is given in the text.

$\epsilon > \omega_E$ and $\epsilon < -\omega_E$. As a remark, the bijection between $\epsilon_{\mathbf{k}n}$ and $\mathbf{k}$ for an electron state in the n-th band is violated in the region where kinks occur. This causes some technical problems while calculating the DOS, v^2 and TDF appearing as coarse lines, which are especially seen around $-\omega_E$ in (b) and (d). Nevertheless, this does not affect the calculation of the electrical conductivity σ and thermopower S as shown later on.

The overall trends of the DOS, v^2 and TDF are also valid for emerging temperatures but show some minor differences. The density of states is still enhanced at ϵ_F but its curvature changes, which is best seen by comparing the blue (10K) and yellow line (300K). In addition, the singularities at $\pm\omega_E$ are smeared out at higher temperatures due to the missing kinks, which is finally based on the broadening of the distribution functions n and f.

Comparing the density of states and the squared velocity with the transport distribution function, one can see, that the TDF is mainly determined by v^2 at each temperature. Figure 3.23 (a) shows the TDF on a smaller energy scale around ϵ_F. The derivatives of the Fermi-Dirac distribtution functions $-(\partial f/\partial\epsilon)$ at every temperature are also given as dashed lines to highlight the relevant integration range for the calculation of the transport properties σ and S. At 10K, it is $\epsilon \ll |\omega_E|$ and the technical issues mentioned before are not crucial.

The electrical conductivity shown in (b) is directly proportional to the generalized transport coefficient $\mathscr{L}^0$, which is obtained as an integral over the TDF via equation 2.2.31. Hence, the decrease of σ compared to σ^0, which is the electrical conductivity of the non-interacting electron system, reflects the decrease of the TDF at each temperature. For $T \geq 600$K it is $\sigma \sim \sigma^0$. Decreasing the temperature reduces σ up to 65% at 100K, which is even slightly lower than σ at 10K. Nevertheless, a reduction of the electrical conductivity due to a renormalization is not expected in the literature [48]. Within the

Drude model σ is obtained as

$$\sigma^{\text{Drude}} = \frac{ne^2\tau}{m} \quad , \tag{3.3.3}$$

where m is the effective mass. The renormalization factors, $(1+\lambda)$, for τ and m cancel each other and σ should be unaffected [48]. On the other hand, assuming the relaxation time to be inversely proportional to the density of states (DOS) as in equation 3.2.8, a different result is obtained. Assuming DOS to be renormalized by the factor $(1+\lambda)$ as obtained from figure 3.22 and stated by Grimvall [48], the renormalized relaxation time reads as

$$\tau^* \propto \frac{1}{\text{DOS}^*} = \frac{1}{\text{DOS}(1+\lambda)} = \frac{\tau}{(1+\lambda)} \quad , \tag{3.3.4}$$

which would explain the decreased electrical conductivity.

Figure (c) shows, that the thermopower is enhanced due to the renormalization compared to S^0 of the bare system for $T < 600$K. The maximal enhancement throughout the temperature range is found at 100K with an increase of 84% (d). Keeping in mind, that the thermopower is roughly proportional to the slope of the TDF divided by the TDF itself, one reason for the enhancement is directly given by the decrease of the conductivity. However, this alone can not explain the large increase and the different slope of the transport distribution functions at each T has to favour the enhancement as well. The last is not obvious since the TDFs look quite similar in the relevant energy range.

3.3.2. Renormalization in metals and possible issues with transport calculations

The scheme, which was introduced in the previous section and explained for a model system to calculate the renormalized band structure and subsequently the transport properties, could be applied only in parts to lead.

The renormalization due to the real part of the electron self-energy Σ' is done with two approaches. The first one uses the $\mathbf{k}$-dependent Éliashberg spectral function $\alpha^2F_\mathbf{k}$ obtained for the real phonon spectrum, which is shown in figure 3.11, to calculate $\Sigma''_\mathbf{k}$ via eq. 2.1.44 and $\Sigma'_\mathbf{k}$ with the Kramers-Kronig transformation in eq. 2.1.54. The second one simply uses the isotropic Éliashberg function α^2F. Figure 3.24 (a) shows the bare band structure with the renormalized band structure around the Fermi energy at 10K as large insets. The underlying figure is the same as in fig. 3.4. All qualitative features were already discussed in the previous section. The kinks themselves are not so well established due to technical reasons. This means, that the computational effort is large to perform the renormalization and to resolve the renormalized bands on an energy scale less than 10meV. This issue will be addressed later on again during the calculation of the transport distribution function. The renormalizations based on $\alpha^2F_\mathbf{k}$ and α^2F are similar for the states along the $\overline{\text{XW}}$-line (upper figure) and more diverging for the states along the $\overline{\Gamma\text{X}}$-line (bottom figure), which favours the use of an anisotropic Éliashberg function . Anyhow, the isotropic Éliashberg function was used further on to reduce the computational effort. The related real and imaginary parts of Σ are shown in (b). Characteristic features due to the specific phonon spectrum of lead are only visible at very low temperatures. They disappear extremly fast with emerging temperature and are already lost at 10K.

The transport distribution function was first calculated on a $\mathbf{k}$ point mesh with nearly 360'000 $\mathbf{k}$ points in the irreducible part of the Brillouin zone (IBZ). Usually, such a mesh is dense enough to obtain σ and S of metals. However, expected features in the TDF known from the investigation of the free electron model could not be reproduced (dark blue line in fig. 3.24(c)). Especially the peaks around

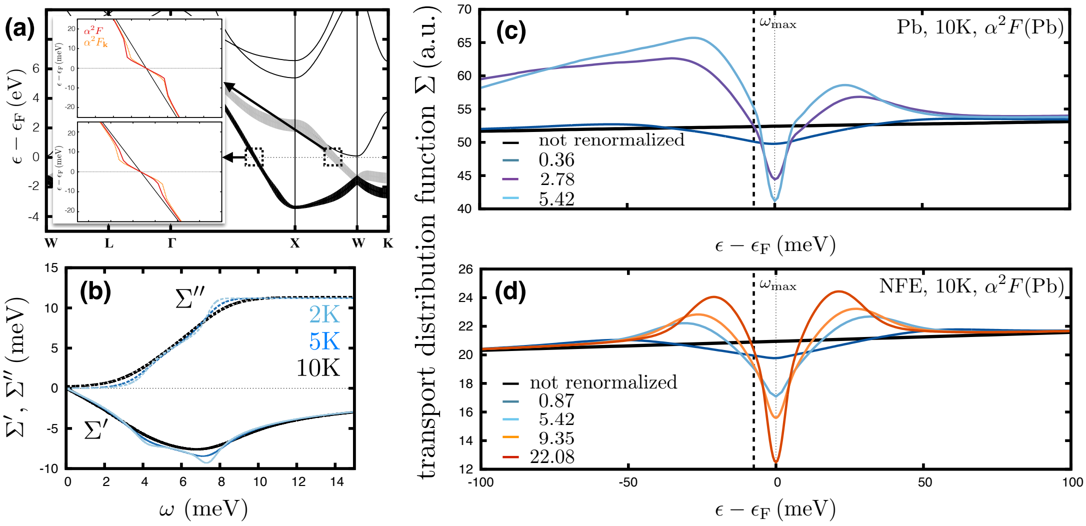

Figure 3.24.: Transport properties due to renormalization effects from the electron-phonon interaction in lead. (a) Band structure of lead. The insets show the bare dispersion and renormalized dispersion around the Fermi energy. The renormalization is performed with the isotropic Éliashberg function α^2F (red line) and the **k**-dependent one $\alpha^2F_{\mathbf{k}}$ (dashed orange line). (b) Real and imaginary part of the self-energy calculated with α^2F. Two peaks occur at 4 and 7 meV in Σ' at very low temperatures originating from the peaks in the Éliashberg function . Nevertheless, these features are already lost at 10K. (c) Transport distribution function (TDF) for the renormalized band structure at 10K for three **k** point sets (colored lines). The numbers, given in 10^6, are the **k** points in the irreducible part of the Brillouin zone (IBZ). In principal, the same behaviour is found as in the case of the free electron model in fig. 3.22 but the TDF could not be used to calculate an electrical conductivity or thermopower due to convergence issues, which are discussed in the text. (d) TDF of a free electron model, which mimics the band structure of lead around the Fermi energy in terms of an isotropic velocity taken from the inner Fermi sheet. The renormalization is done with the Éliashberg function of Pb. As before, the numbers are the **k** points in the IBZ given in 10^6. The TDF did not converge within the used **k** point sets, which indicates that the convergence of the transport distribution function of lead in fig. (c) is difficult to achieve as well.

$\pm\omega_{max}$ and the flat plateau in between is missing. A drastical increase of the **k** points up to 5.42 million points in the IBZ did not lead to a converged TDF (light blue line). The reason for that is probably related to the small phonon band width in lead of ~ 10meV and the large electron-phonon coupling constant of ~ 1. Both conditions and the large velocity (steep slope in the band structure) of several **k** points at the Fermi energy requires a really dense sampling of the Brillouin zone to accurately describe the renormalization. Therefore, a cross-comparison with a free electron model was considered. The velocity of the model was supposed to be isotropic at ϵ_F and its value was taken from a state of the inner Fermi sheet of lead, which lies at the $\overline{\Gamma L}$-line and was refered to as P1 in chapter 3.2. The self-energy was calculated with the isotropic Éliashberg function of lead. Although these approximations are rather crude for lead they are appropriate as a first step. The transport distribution functions calculated in this way are shown in figure 3.24(d) for various sets of **k** points. The TDFs for the **k** point grids with the two lowest amounts of **k** points are in qualitative good agreement with the TDF derived from the renormalized band structure in lead (compare (c) and (d)). A further increase of **k** points up to 22 million points in the IBZ, which is computationally not feasible for lead but can be realized for the model system, does not lead to convergence of the transport distribution but the key features mentioned before are slowly appearing.

The calculation of the electrical conductivity and thermopower in lead due to renormalized states seems to be peculiar and challenging. The situation is probably completely different and easier to handle in other metals, where the phonon band width is larger (~ 30meV) like in copper or niob.

3.4. Spectral function and its application in transport calculations

The upcoming chapter addresses the spectral function $\mathcal{A}$ due to electron-phonon coupling.

First, the spectral function obtained in experiments and the extraction of the real and imaginary part of the self-energy from measurements are discussed. A calculated spectral function for the model system introduced in the previous chapter is also shown. The second part deals with the role of the spectral function in transport calculations since all many-body effects, i.e. renormalization and lifetime broadening, are already accounted for in $\mathcal{A}$. Unfortunately, the electrical conductivity and thermopower can not be calculated from the spectral function within Boltzmann theory. As a step beyond the detached investigation of the imaginary and real part of the self-energy and their impact onto the electrical conductivity and thermopower presented in chapter 3.2 and 3.3, some comments and thoughts about the combination of both parts without use of the spectral function are given.

3.4.1. Spectral function in experiment and theory

The experimental access to the electron-phonon coupling is naturally given by the spectral function, which is measureable by angle-resolved photoemission spectroscopy (ARPES) [26, 29, 59, 70, 95]. Due to several subsequent investigations, i.e. energy distribution curves (EDC) or momentum distribution curves (MDC), the extraction of both parts of the self-energy is possible. A MDC represents a cut through the photoemission intensity map as function of the wave vector $\mathbf{k}$ at constant photon and kinetic energies. Unfortunately, the spectral function is only a part of the measured photoemission intensity $\mathcal{I}$. Assuming several approximations, which are discussed in detail in the aforementioned citations, the intensity reads as

$$\mathcal{I}(E_{\text{kin}},\mathbf{k}) \propto \left|M_{fi}(\mathbf{k}_f,\mathbf{k}_i)\right| f(h\nu - E_{\text{kin}} - \Phi, T)\mathcal{A}(h\nu - E_{\text{kin}} - \Phi,\mathbf{k})F(\mathcal{L})\mathcal{R} \quad . \tag{3.4.1}$$

Here, E_{kin} is the kinetic energy of the photoelectron, $\left|M_{fi}\right|$ is the corresponding matrix element of the photoemission process, $h\nu$ is the photon energy, Φ is the work function, f is the Fermi-Dirac distribu-

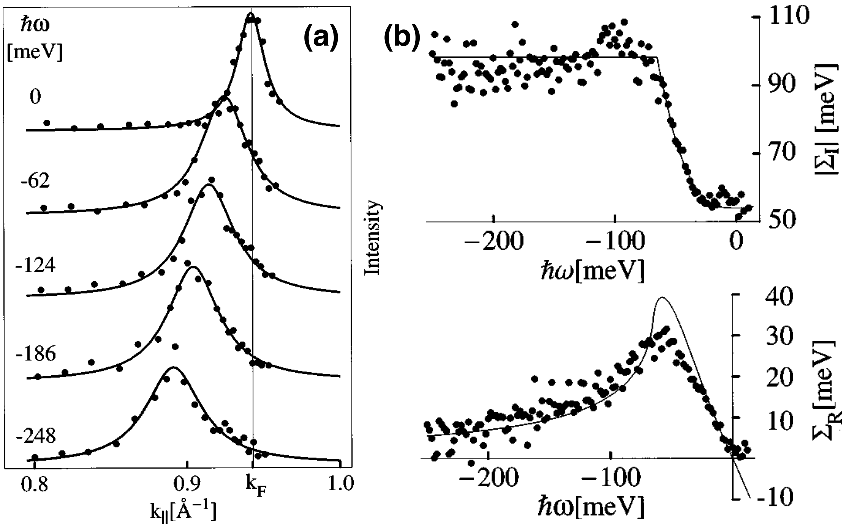

Figure 3.25.: Photoemission data from the Be(0001) surface state. (a) Momentum distribution curves fitted by Lorentzians (solid line). (b) Imaginary and real part of the self-energy obatined from the fitted MDCs in the upper and lower figure, respectively. The solid lines show the calculated Σ'' and Σ' for a Debye model with $\omega_{\text{D}} = 65\text{meV}$ and $\lambda = 0.65$. The figures were taken from LaShell *et. al* [76].

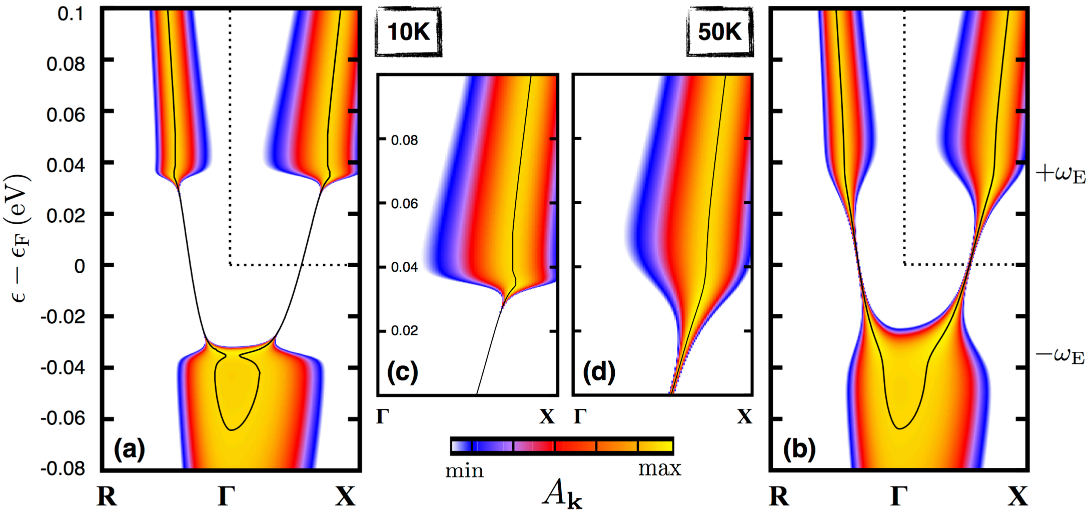

Figure 3.26.: Spectral function $\mathscr{A}_k$ for a free electron model at 10K (a) and 50K (b). The model is the same as introduced in fig. 3.18(c) with the parameters $\lambda = 0.5$ and $\omega_E = 35$meV. The values of $\mathscr{A}_k$ are given by the color code. The obtained renormalized band is shown as solid black line. Figure (c) and (d) are closer views of the band structure marked by dotted lines at 10K and 50K, respectively. Energy scales are equal in (a) and (b) as well as in (c) and (d).

tion function and $\mathscr{A}$ is the spectral function. The function $F(\mathscr{L})$ is an integrated Lorentzian $\mathscr{L}$ while the last term $\mathscr{R}$ describes the resolution function, which depends on the experimental setup. Within further assumptions and assuming the resolution function to be known, the photoemission intensity is directly proportional to the spectral function times the Fermi-Dirac distribution function. Fitting the obtained MDCs with Lorentzians relates Σ'' to their width and Σ' to their maximum as shown in figure 3.25 for an ARPES measurement from the Be(0001) surface [76]. In addition to the experiment, the spectral function is nowadays often calculated within certain phonon models, i.e. Debye model or Einstein model, and with the parameters ω_D or ω_E and λ, which are obtained from the measurement, to provide an additional check.

To close this section, figure 3.26 shows the calculated spectral function $\mathscr{A}_k$ of the free electron model discussed previously in section 3.3.1. The black line indicates the renormalized band structure obtained from the maximum of $\mathscr{A}_k$. The width of the spectral function is related to the imaginary part of the self-energy. Within the Einstein model Σ'' is very small at 10K for $\epsilon \leq |\omega_E|$. Hence, the width of $\mathscr{A}_k$ is very small in this energy range but does not vanish, which one might suggest due to the figure. Compared to a Debye model with similar parameters, $\Sigma''_{\text{Einstein}}$ is a factor 10^2 smaller than Σ''_{Debye} at $\omega = 0$meV.

3.4.2. Remarks on transport calculations accounting for the full complex electron self-energy

In general, the calculation of transport properties due to many-body effects like the electron-phonon interaction requires the use of the spectral function instead of the detached consideration of the real and imaginary part of the self-energy. Such an approach is given by the Kubo formalism, where the electrical conductivity can be expressed in terms of Green's functions and which is known as Kubo-Greenwood formula [47, 74]. Rewriting the Green's functions in their *spectral representations* reveals the link to the spectral function $\mathscr{A}$. Such a description was out of scope in this thesis and further information can be found elsewhere [3].

While chapter 3.2 and 3.3 discusses Σ'' and Σ', respectively the relaxation time τ and renormalization effects, separately, the following is about the combination of both parts in transport calculations to

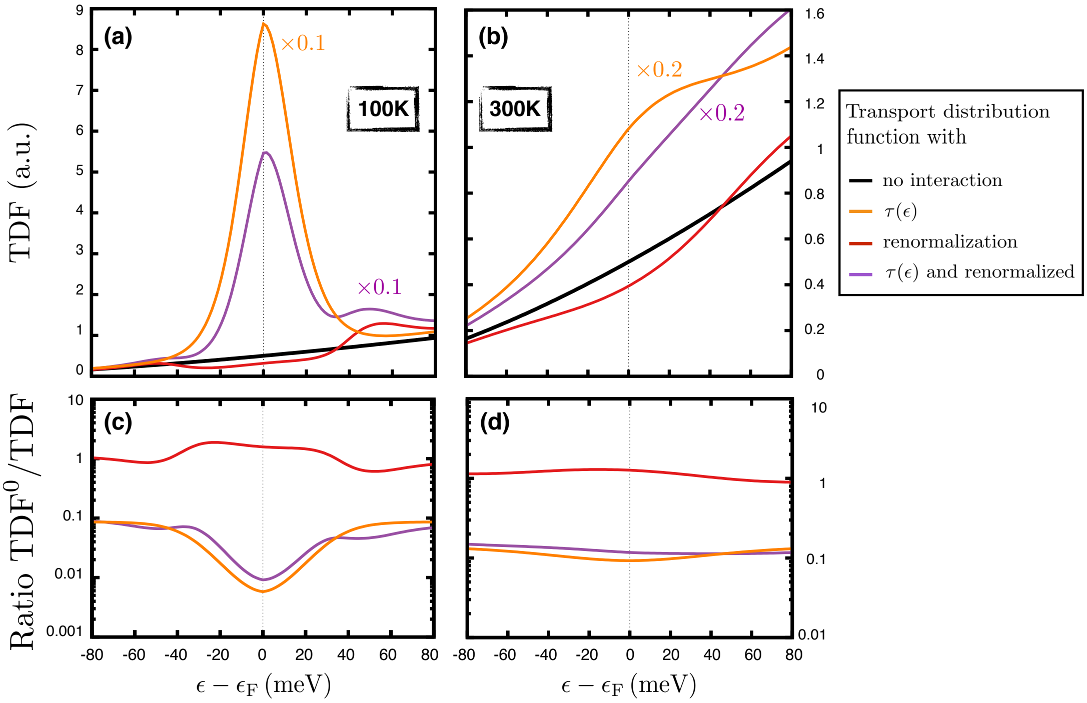

Figure 3.27.: Transport distribution function (TDF) of a free electron model under the influence of the electron-phonon interaction (EPI) considered in different ways at 100K and 300K in (a) and (b), respectively. The transport distribution function of the bare system TDF^0 is shown as black line. The TDF calculated with an energy-dependent relaxation time $\tau(\epsilon)$ is shown as orange line while the TDF obtained from the renormalized band structure is shown as red line. The TDF calculated due to the relaxation time and the renormalization is shown as purple line. The influence of the EPI onto the TDF in each consideration (according to the color) is given as ratio $\mathrm{TDF}^0/\mathrm{TDF}$ in (c) and (d). The combinded TDF including the relaxation time and renormalization effects is dominated by $\tau(\epsilon)$ at lower temperatures. At higher temperatures however, the renormalization seems to be the dominanting part.

account for both effects without using the spectral function. The most obvious approach is to calculate the self-energy of the bare system and obtain the relaxation time and the renormalized band structure as previously. Subsequently, the transport distribution function (TDF) is calculated from the renormalized bands and simply multiplied with the energy-dependent relaxation time. The only difference compared to the treatment in chapter 3.2 is the calculation of the TDF from the interacting instead of the non-interacting system. A similar approach, where the band structure is renormalized first and the relaxation time is calculated afterwards, is probably not correct since Σ'' would somehow depend on Σ' and therefore not considered here.

Figure 3.27 shows the comparison of the transport distribution function calculated in different ways as mentioned before. Again, the system of choice is the free eletron model with the parabolic band dispersion. The black line shows the TDF of the non-interacting electron gas TDF^0, which is proportional to $(\epsilon - \epsilon_\mathrm{F})^{3/2}$. The orange and red lines account for the detached description of the relaxation time and renormalization effects. The purple line shows the TDF for the combined description given by $\mathrm{TDF}^{\mathrm{combined}} = \mathrm{TDF}^{\mathrm{renorm}} \times \tau(\epsilon)$. At 100K (a), the combined TDF is clearly dominated by $\tau(\epsilon)$ revealing a similar peaked structure. Minor differences are found far away from ϵ_F due to the renormalization. To compare more quantitatively, the ratio $\mathrm{TDF}^0/\mathrm{TDF}$ is shown in (c). One can see that the absolute value of the TDF as well as the curvature around ϵ_F are almost solely determined by the relaxation time, which directly transfers to the electrical conductivity and thermopower and is even more pronounced at lower temperatures. At higher temperatures (b), however, the impact of the relaxation time decreases since the characteristic peak of $\tau(\epsilon)$ vanishes as already shown in figure 3.15. Of course, the renormalization is weaker as well but remains strong enough to determine the slope of the transport distribution function (d). Thus, a temperature in between should act as a crossing point separating the two temperature regions, where either Σ'' or Σ' determine the electrical conductivity and thermopower.

Interestingly, the correlation between the temperature region and the major impact of Σ'' or Σ' onto the transport properties is counter intuitive. The influence of the electron-phonon interaction is most visible at the kinks of the band structure at low temperatures. Hence, one might expect that the renormalization is important in transport calculations at those temperatures. However, this is not the case and Σ' dominates at higher temperatures, while Σ'' is the dominant part at lower temperatures. The reason is given by the energetic position of the kinks at the Einstein or Debye frequency, which is off the Fermi energy. Their influence at low temperatures is therefore rather weak compared to the relaxation time, which directly influences the TDF around the Fermi energy.

In conclusion, the consideration of the electron-phonon interaction by means of the relaxation time and the renormalization effects is equally necessary while investigating the whole temperature range below and above the Debye temperature. Nevertheless, the influence of the renormalization will be weaker due to the nature of the electron-phonon coupling meaning that its impact vanishes at higher temperatures. Furthermore, temperatures below the Debye temperatur are usually considered and hence the accurate description of the relaxation time is probably the main purpose in transport calculations.

4 | Summary

The aim of this work was the developement of a procedure, which allows for a very detailed investigation of the interaction between electrons and phonons on the one hand and the computationally demanding calculation of transport properties with respect to the electron-phonon interaction on the other hand. Besides the usual investigation of the relaxation time, the influence due to renormalization effects ought to be addressed as well.

For this reason, *ab initio* calculations based on a pseudopotential method and Wannier functions were performed to evaluate the electron-phonon matrix elements in arbitrary large numbers. The transport properties were subsequently calculated by solving a linearised Boltzmann equation. Thereby, the state-dependency of the electron-phonon relaxation time was mapped on an energy-dependency, which reduces the computational cost.

Results were shown predominantly for lead, which is an archetypal elemental superconductor with strong electron-phonon coupling. Nevertheless, the presented scheme is not limited to any sort of solid and can be applied to more complicated systems.

It was shown, that simple single sheeted Fermi surfaces yield larger relaxation times compared to complicated multi-sheeted ones due to a reduced scattering phase space. Although this was found in lead it seems to be a more general statement. In addition, small Fermi surfaces like in n-doped silicon can act as phonon filter due to the condition of momentum conservation in the scattering process. The experimentally observed enhancement of the thermopower in lead at low temperatures could be reproduced and traced back to the peaked structure of the relaxation time at these temperatures without accounting for the phonon-drag effect.

The renormalization of electron states and its impact onto the electrical conductivity and thermopower was discussed for several model systems. In dependence of the chosen parameters, i.e. temperature, coupling strength, phonon band width, etc., band-splitting occurs and a guide is presented to find these splittings in real systems. Furthermore, an enhanced thermopower due to the renormalization of states was found for a free electron gas as well. The computational effort while performing transport calculations was found to be drastically increased if the phonon band width is rather small, i.e. $\omega_{\mathrm{D}} \lesssim 10\mathrm{meV}$, which is the case in lead.

Conclusively, the combined consideration of the renormalization and the relaxation time was discussed stating that the latter yields the dominant contribution to transport properties in the low-temperature regime, which is usually the temperature range of interest. Nevertheless, a description, which directly takes care of the spectral function would be necessary in the future to accurately deal with the interacting electron system within the Boltzmann theory.

Further improvements can be achieved due to the consideration of the phonon-drag contribution in the Boltzmann equation on a general and for everyone accessible level. An iterative solution of the coupled electron and phonon Boltzmann equations remains an open task by now, while the methodology to do so was laid out within this thesis.

A | Enlarged figures

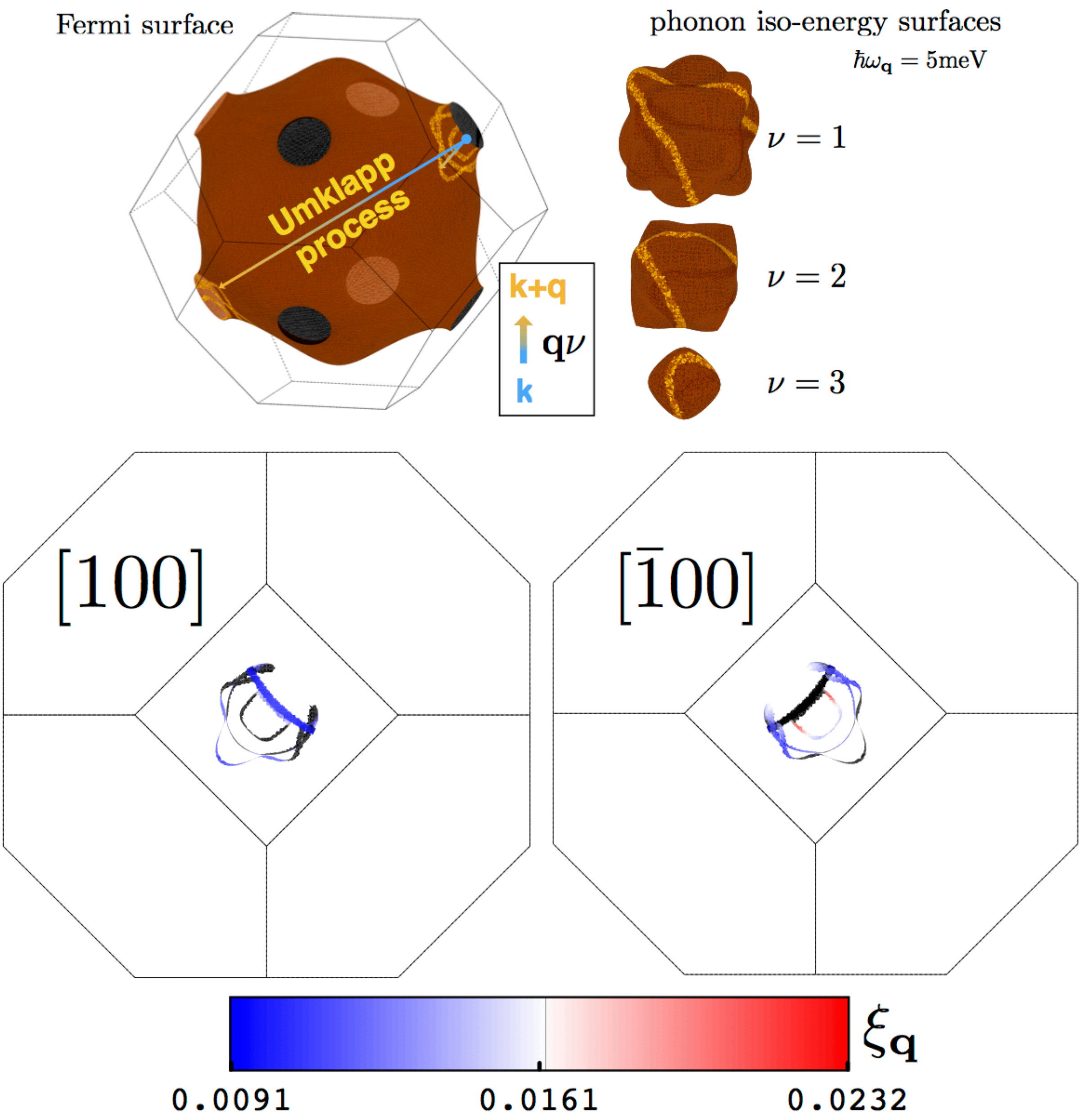
Fermi surface
Umklapp process
k+q
$q\nu$
k
phonon iso-energy surfaces
$\hbar\omega_{\mathbf{q}} = 5\text{meV}$
$\nu = 1$
$\nu = 2$
$\nu = 3$
[100]
[$\bar{1}$00]
$\xi_{\mathbf{q}}$
0.0091
0.0161
0.0232

Figure A.1.: Enlargement of figure 3.1 to highlight the nesting values $\xi_{\mathbf{q}}$ of the Umklapp processes for the initial electron state marked in blue at Fermi surface (top left) in Cu. The bottom figures show only the involved phonon wave vectors from all three modes with the superimposed nesting values.

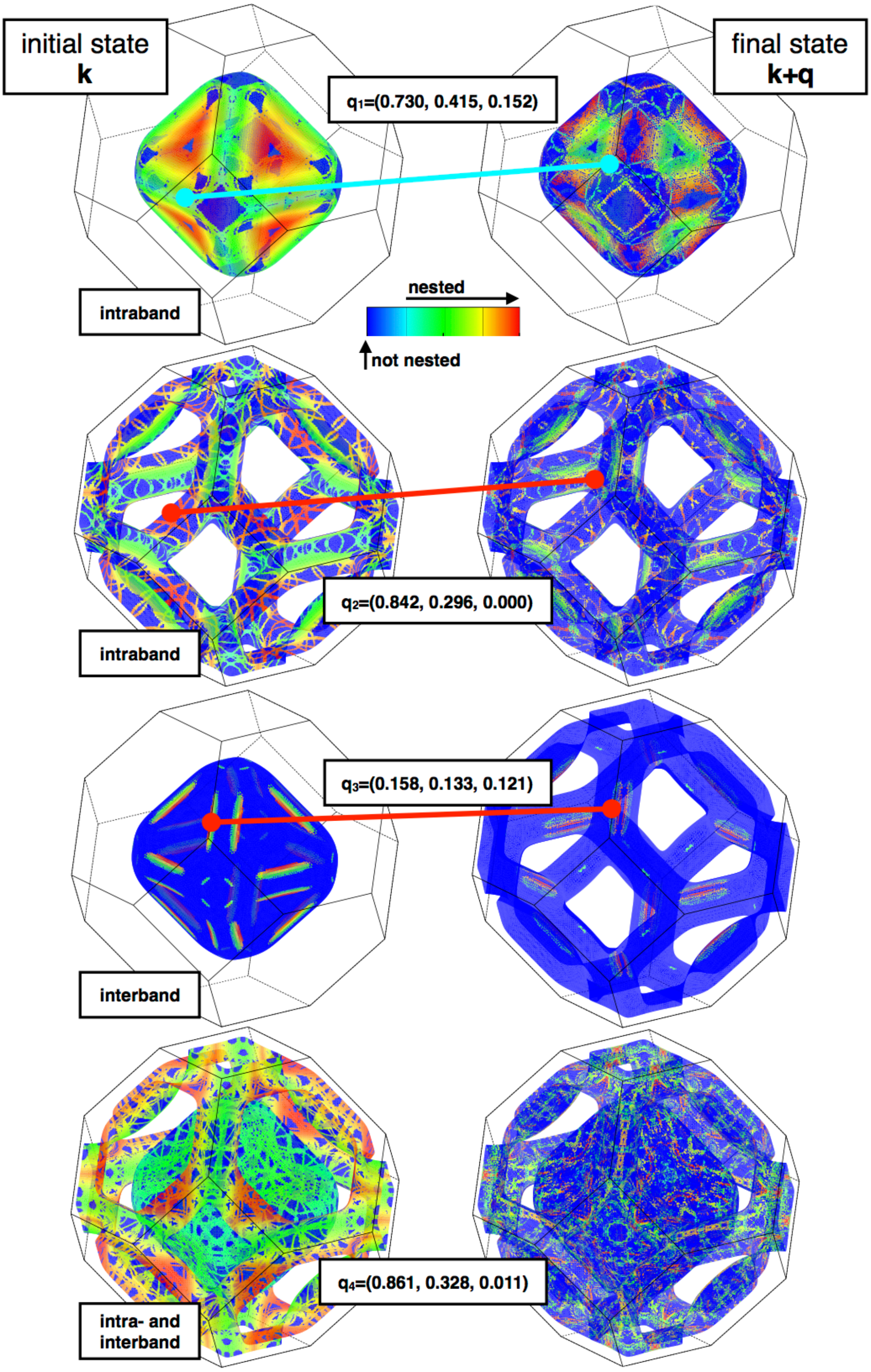
initial state
k
final state
k+q
q1=(0.730, 0.415, 0.152)
intraband
nested
not nested
q2=(0.842, 0.296, 0.000)
intraband
q3=(0.158, 0.133, 0.121)
interband
q4=(0.861, 0.328, 0.011)
intra- and interband

Figure A.2.: Enlargement of figure 3.2 to highlight the nested pairs in Pb. Same color marks a nested pair with initial and final state, except for blue, which displays the bare Fermi surface.

Bibliography

[1] M. Alcántara Ortigoza, I. Y. Sklyadneva, R. Heid, E. V. Chulkov, T. S. Rahman, K. P. Bohnen, and P. M. Echenique. *Ab initio lattice dynamics and electron-phonon coupling of Bi(111).* Physical Review B **90** (19), (2014) (cit. on p. 1).

[2] P. B. Allen. *Solids with thermal or static disorder. I. One-electron properties.* Physical Review B **18** (10), (1978) (cit. on p. 12).

[3] P. B. Allen. *Chapter 6 Electron Transport. Conceptual Foundations of MaterialsA Standard Model for Ground- and Excited-State Properties.* Ed. by S. G. Louie and M. L. Cohen. Vol. 2. Contemporary Concepts of Condensed Matter Science. Elsevier, 2006 (cit. on p. 59).

[4] P. B. Allen and V. Heine. *Theory of the temperature dependence of electronic band structures.* Journal of Physics C: Solid State Physics **9** (12), (1976) (cit. on p. 12).

[5] P. B. Allen. *Neutron Spectroscopy of Superconductors.* Physical Review B **6** (7), (1972) (cit. on p. 13).

[6] P. B. Allen and M. L. Cohen. *Pseudopotential Calculation of the Mass Enhancement and Superconducting Transition Temperature of Simple Metals.* Physical review **187** (2), (1969) (cit. on p. 14).

[7] J. M. An, S. Y. Savrasov, H. Rosner, and W. E. Pickett. *Extreme electron-phonon coupling in boron-based layered superconductors.* Physical Review B **66** (22), (2002) (cit. on p. 32).

[8] P. Aynajian, T. Keller, L. Boeri, S. M.S. K. Habicht, and B. Keimer. *Energy Gaps and Kohn Anomalies in Elemental Superconductors.* preprint (2008). arXiv: `0808.1028v1` (cit. on pp. 32, 37).

[9] J. Bardeen and W. Shockley. *Deformation Potentials and Mobilities in Non-Polar Crystals.* Phys. Rev. **80** (1), (1950) (cit. on p. 1).

[10] J. Bardeen, L. N. Cooper, and J. R. Schrieffer. *Theory of superconductivity.* Physical Review **108** (5), (1957) (cit. on p. 1).

[11] J. Bardeen and D. Pines. *Electron-Phonon Interaction in Metals.* Physical review **99** (4), (1955) (cit. on p. 1).

[12] S. Baroni, P. Giannozzi, and A. Testa. *Green-Function Approach to Linear Response in Solids.* Physical Review Letters **58** (18), (1987) (cit. on p. 7).

[13] S. Baroni, S. de Gironcoli, A. Dal Corso, and P. Giannozzi. *Phonons and related crystal properties from density-functional perturbation theory.* Reviews of Modern Physics **73** (2001) (cit. on p. 7).

[14] J. Bass and K. H. Fischer. *Metals: Electronic Transport Phenomena.* Landolt-Börnstein, New Series III/15a. 1982 (cit. on p. 48).

[15] M. Battiato, J. M. Tomczak, Z. Zhong, and K. Held. *Unified Picture for the Colossal Thermopower Compound FeSb$_2$.* Physical Review Letters **114** (23), (2015) (cit. on p. 27).

[16] R. Bauer, A. Schmid, P. Pavone, and D. Strauch. *Electron-phonon coupling in the metallic elements Al, Au, Na, and Nb: A first-principles study.* Physical Review B **57** (18), (1998) (cit. on p. 1).

[17] M. Bernardi, D. Vigil-Fowler, J. Lischner, J. B. Neaton, and S. G. Louie. *Ab Initio Study of Hot Carriers in the First Picosecond after Sunlight Absorption in Silicon.* Physical Review Letters **112** (25), (2014) (cit. on pp. 1, 37, 42).

[18] M. Bernardi, D. Vigil-Fowler, C. S. Ong, J. B. Neaton, and S. G. Louie. *Ab initio study of hot electrons in GaAs.* Proceedings of the National Academy of Sciences **112** (17), (2015) (cit. on p. 37).

[19] C. M. Bhandari. *Effect of phonon-drag on electrical conductivity in copper and its alloys.* Physica **40** (1), (1968) (cit. on p. 27).

[20] J. Blatt. *Thermoelectric Power of Metals.* Springer-Verlag, 1976 (cit. on p. 48).

[21] K. M. Borysenko, J. T. Mullen, E. A. Barry, S. Paul, Y. G. Semenov, J. M. Zavada, M. B. Nardelli, and K. W. Kim. *First-principles analysis of electron-phonon interactions in graphene.* Physical Review B **81** (12), (2010) (cit. on p. 1).

[22] M. Calandra and F. Mauri. *Electron-phonon coupling and phonon self-energy in MgB_2: Interpretation of MgB_2 Raman spectra.* Physical Review B **71** (6), (2005) (cit. on p. 13).

[23] E. Cannuccia and A. Marini. *Ab-initio study of the effects induced by the electron-phonon scattering in carbon based nanostructures.* preprint (2013). arXiv: `1304.0072v1` (cit. on p. 12).

[24] D. G. Cantrell and P. N. Butcher. *A calculation of the phonon-drag contribution to the thermopower of quasi-2D electrons coupled to 3D phonons. I. General theory.* Journal of Physics C: Solid State Physics **20** (13), (1987) (cit. on p. 27).

[25] J. G. Cook, M. J. Laubitz, and M. P. Van der Meer. *Thermal conductivity, electrical resistivity, and thermoelectric power of Pb from 260 to 550 K.* Journal of Applied Physics **45** (2), (1974) (cit. on p. 48).

[26] T. Cuk, D. H. Lu, X. J. Zhou, Z. X. Shen, T. P. Devereaux, and N. Nagaosa. *A review of electron-phonon coupling seen in the high-T_c superconductors by angle-resolved photoemission studies (ARPES).* physica status solidi (b) **242** (1), (2005) (cit. on pp. 15, 58).

[27] M. M. Dacorogna, M. L. Cohen, and P. K. Lam. *Self-consistent calculation of the q dependence of the electron-phonon coupling in aluminum.* Physical Review Letters **55** (8), (1985) (cit. on p. 1).

[28] A. Dal Corso. *Ab initio phonon dispersions of face centered cubic Pb: effects of spin–orbit coupling.* Journal of Physics: Condensed Matter **20** (44), (2008) (cit. on pp. 16, 33, 42).

[29] A. Damascelli, Z. Hussain, and Z. X. Shen. *Angle-resolved photoemission studies of the cuprate superconductors.* Reviews of Modern Physics **75** (2003) (cit. on pp. 15, 58).

[30] A. Eiguren, S. de Gironcoli, E. V. Chulkov, P. M. Echenique, and E. Tosatti. *Electron-Phonon Interaction at the Be(0001) Surface.* Physical Review Letters **91** (16), (2003) (cit. on p. 1).

[31] A. Eiguren, B. Hellsing, F. Reinert, G. Nicolay, E. V. Chulkov, V. M. Silkin, S. Hüfner, and P. M. Echenique. *Role of Bulk and Surface Phonons in the Decay of Metal Surface States.* Physical Review Letters **88** (6), (2002) (cit. on p. 1).

[32] G. M. Eliashberg. *Interactions between electrons and lattice vibrations in a superconductor.* Sov. Phys.-JETP (Engl. Transl.);(United States), 1960 (cit. on p. 1).

[33] G. M. Eliashberg. *Temperature Greens Function for Electrons in a Superconductor.* Soviet Physics Jetp-Ussr **12** (5), (1961) (cit. on p. 1).

[34] H. Y. Fan. *Temperature Dependence of the Energy Gap in Monatomic Semiconductors.* Physical review **78** (6), (1950) (cit. on p. 11).

[35] H. Y. Fan. *Temperature Dependence of the Energy Gap in Semiconductors.* Physical review **82** (6), (1951) (cit. on p. 11).

[36] R. P. Feynman. *Forces in Molecules.* Physical Review **56** (4), (1939) (cit. on p. 7).

[37] M. Fiorentini and N. Bonini. *Thermoelectric coefficients of n-doped silicon from first principles via the solution of the Boltzmann transport equation.* Physical Review B **94** (8), (2016) (cit. on pp. 27–28).

[38] A. Floris, A. Sanna, S. Massidda, and E. K. U. Gross. *Two-band superconductivity in Pb from ab initio calculations.* Physical Review B **75** (5), (2007) (cit. on p. 37).

[39] P. Giannozzi, S. de Gironcoli, P. Pavone, and S. Baroni. *Ab initio calculation of phonon dispersions in semiconductors.* Physical Review B **43** (9), (1991) (cit. on p. 7).

[40] P. Giannozzi et al. *QUANTUM ESPRESSO: a modular and open-source software project for quantum simulations of materials.* Journal of Physics: Condensed Matter **21** (39), (2009) (cit. on p. 1).

[41] S. de Gironcoli. *Lattice dynamics of metals from density-functional perturbation theory.* Physical Review B **51** (10), (1995) (cit. on p. 8).

[42] F. Giustino. *Electron-phonon interactions from first principles.* Reviews of Modern Physics **89** (2017) (cit. on pp. 3, 12).

[43] F. Giustino, M. Cohen, and S. Louie. *Electron-phonon interaction using Wannier functions.* Physical Review B **76** (16), (2007) (cit. on pp. 9–10, 12, 34).

[44] F. Giustino, S. G. Louie, and M. L. Cohen. *Electron-Phonon Renormalization of the Direct Band Gap of Diamond.* Physical Review Letters **105** (26), (2010) (cit. on pp. 1, 52).

[45] X. Gonze. *Perturbation Expansion of Variational-Principles at Arbitrary Order.* Physical Review A **52** (2), (1995) (cit. on p. 7).

[46] X. Gonze. *Adiabatic density-functional perturbation theory.* Physical Review A **52** (2), (1995) (cit. on p. 7).

[47] D. A. Greenwood. *The Boltzmann equation in the theory of electrical conduction in metals. Proceedings of the Physical Society.* Vol. 71. 4. 1958 (cit. on p. 59).

[48] G. Grimvall. *The electron-phonon interaction in metals.* North-Holland Publishing Company, 1981 (cit. on pp. 1, 12, 27, 54–56).

[49] S. Grothe, S. Johnston, S. Chi, P. Dosanjh, S. A. Burke, and Y. Pennec. *Quantifying Many-Body Effects by High-Resolution Fourier Transform Scanning Tunneling Spectroscopy.* Physical Review Letters **111** (24), (2013) (cit. on pp. 50–51).

[50] T. Gunst, T. Markussen, K. Stokbro, and M. Brandbyge. *First-principles method for electron-phonon coupling and electron mobility: Applications to two-dimensional materials.* Physical Review B **93** (3), (2016) (cit. on pp. 1, 34, 37).

[51] L. Gurevich. *Thermoelectric properties of conductors.* Journal of Physics USSR **9** (477), (1945) (cit. on p. 27).

[52] L. Gurevich. *Thermoelectric properties of conductors.* Journal of Physics USSR **10** (67), (1946) (cit. on p. 27).

[53] Y. G. Gurevich and O. L. Mashkevich. *The electron-phonon drag and transport phenomena in semiconductors.* Physics reports **181** (6), (1989) (cit. on p. 27).

[54] R. Heid, K. P. Bohnen, I. Y. Sklyadneva, and E. V. Chulkov. *Effect of spin-orbit coupling on the electron-phonon interaction of the superconductors Pb and Tl.* Physical Review B **81** (17), (2010) (cit. on pp. 36, 42).

[55] R. Heid. *Lecture notes - Density Functional Perturbation Theory and Electron Phonon Coupling.* 2013 (cit. on p. 12).

[56] R. Heid, I. Y. Sklyadneva, and E. V. Chulkov. *Electron-phonon coupling in topological surface states: The role of polar optical modes.* Scientific Reports (2017) (cit. on p. 1).

[57] H. Hellmann. *Einführung in die Quantenchemie.* Ed. by D. Andrae. 1st ed. Berlin, Heidelberg: Springer Berlin Heidelberg, 2015 (cit. on p. 7).

[58] C. Herring. *Theory of the Thermoelectric Power of Semiconductors.* Physical review **96** (5), (1954) (cit. on p. 27).

[59] P. Hofmann, I. Y. Sklyadneva, E. D. L. Rienks, and E. V. Chulkov. *Electron–phonon coupling at surfaces and interfaces.* New Journal of Physics **11** (12), (2009) (cit. on pp. 20, 50, 58).

[60] P. Hohenberg and W. Kohn. *Inhomogeneous Electron Gas.* Physical review **136** (3B), (1964) (cit. on p. 4).

[61] R. P. Huebener. *Effect of phonon drag on the electrical resistivity of metals.* Physical review **146** (2), (1966) (cit. on p. 27).

[62] C. Jacoboni, C. Canali, G. Ottaviani, and A. A. Quaranta. *A review of some charge transport properties of silicon.* Solid-State Electronics (1977) (cit. on p. 42).

[63] C. Jacoboni and L. Reggiani. *The Monte-Carlo Method for the Solution of Charge Transport in Semiconductors with Applications to Covalent Materials.* Reviews of Modern Physics **55** (1983) (cit. on p. 42).

[64] M. Jonson and G. D. Mahan. *Electron-phonon contribution to the thermopower of metals.* Physical Review B **42** (15), (1990) (cit. on p. 1).

[65] K. Kaasbjerg, K. S. Thygesen, and K. W. Jacobsen. *Phonon-limited mobility in n-type single-layer MoS_2 from first principles.* Physical Review B **85** (11), (2012) (cit. on p. 1).

[66] D. Kasinathan, K. Koepernik, J. Kuneš, H. Rosner, and W. E. Pickett. *Origin of strong coupling in lithium under pressure.* Physica C: Superconductivity and its Applications **460-462** (2007) (cit. on p. 16).

[67] D. Kasinathan, J. Kuneš, A. Lazicki, H. Rosner, C. S. Yoo, R. T. Scalettar, and W. E. Pickett. *Superconductivity and Lattice Instability in Compressed Lithium from Fermi Surface Hot Spots.* Physical Review Letters **96** (4), (2006) (cit. on p. 16).

[68] O. Kilian, G. Allan, and L. Wirtz. *Near Kohn anomalies in the phonon dispersion relations of lead chalcogenides.* Physical Review B **80** (24), (2009) (cit. on p. 32).

[69] H.-S. Kim, Z. M. Gibbs, Y. Tang, H. Wang, and G. J. Snyder. *Characterization of Lorenz number with Seebeck coefficient measurement.* APL Materials **3** (4), (2015) (cit. on p. 28).

[70] C. Kirkegaard, T. K. Kim, and P. Hofmann. *Self-energy determination and electron–phonon coupling on Bi(110).* New Journal of Physics **7** (2005) (cit. on pp. 50, 58).

[71] W. Kohn. *Image of the Fermi Surface in the Vibration Spectrum of a Metal.* Physical Review Letters **2** (9), (1959) (cit. on p. 16).

[72] W. Kohn and L. J. Sham. *Self-Consistent Equations Including Exchange and Correlation Effects.* Physical review **140** (4A), (1965) (cit. on pp. 4–5).

[73] H. A. Kramers. *La diffusion de la lumiere par les atomes.* 1927 (cit. on p. 15).

[74] R. Kubo. *Statistical-Mechanical Theory of Irreversible Processes. I. General Theory and Simple Applications to Magnetic and Conduction Problems.* Journal of the Physical Society of Japan **12** (6), (1957) (cit. on p. 59).

[75] R. de L. Kronig. *On the Theory of Dispersion of X-Rays.* Journal of the Optical Society of America **12** (6), (1926) (cit. on p. 15).

[76] S. LaShell, E. Jensen, and T. Balasubramanian. *Nonquasiparticle structure in the photoemission spectra from the Be(0001) surface and determination of the electron self energy.* Physical Review B **61** (3), (2000) (cit. on pp. 58–59).

[77] A. Leonardo, I. Y. Sklyadneva, V. M. Silkin, P. M. Echenique, and E. V. Chulkov. *Ab initio calculation of the phonon-induced contribution to the electron-state linewidth on the Mg(0001) surface versus bulk Mg.* Physical Review B **76** (3), (2007) (cit. on p. 1).

[78] L.-P. Lévy. *Magnetism and Superconductivity.* Springer-Verlag, 2000 (cit. on p. 15).

[79] W. Li. *Electrical transport limited by electron-phonon coupling from Boltzmann transport equation: An ab initio study of Si, Al, and MoS_2.* Physical Review B **92** (7), (2015) (cit. on pp. 1, 23, 37, 45).

[80] X. Li, J. T. Mullen, Z. Jin, K. M. Borysenko, M. Buongiorno Nardelli, and K. W. Kim. *Intrinsic electrical transport properties of monolayer silicene and MoS_2 from first principles.* Physical Review B **87** (11), (2013) (cit. on p. 1).

[81] B. Liao, B. Qiu, J. Zhou, S. Huberman, K. Esfarjani, and G. Chen. *Significant Reduction of Lattice Thermal Conductivity by the Electron-Phonon Interaction in Silicon with High Carrier Concentrations: A First-Principles Study.* Physical Review Letters **114** (11), (2015) (cit. on pp. 1, 37).

[82] B. Liao, J. Zhou, B. Qiu, M. S. Dresselhaus, and G. Chen. *Ab initio study of electron-phonon interaction in phosphorene.* Physical Review B **91** (23), (2015) (cit. on pp. 1, 37).

[83] A. Y. Liu and A. A. Quong. *Linear-response calculation of electron-phonon coupling parameters.* Physical Review B **53** (12), (1996) (cit. on p. 37).

[84] J. M. Luttinger. *Fermi Surface and Some Simple Equilibrium Properties of a System of Interacting Fermions.* Physical Review **119** (4), (1960) (cit. on p. 54).

[85] S. K. Lyo. *Electron-phonon enhancement of thermoelectricity in metals.* Physical Review B **17** (6), (1978) (cit. on p. 1).

[86] A. H. MacDonald and S. H. Vosko. *A relativistic density functional formalism.* Journal of Physics C: Solid State Physics **12** (15), (1979) (cit. on p. 5).

[87] G. D. Mahan. *Many particle physics.* Springer Science+ Business Media New York, 2000 (cit. on p. 12).

[88] G. D. Mahan, L. Lindsay, and D. A. Broido. *The Seebeck coefficient and phonon drag in silicon.* Journal of Applied Physics **116** (24), (2014) (cit. on p. 27).

[89] E. R. Margine and F. Giustino. *Anisotropic Migdal-Eliashberg theory using Wannier functions.* Physical Review B **87** (2), (2013) (cit. on p. 34).

[90] A. Marini. *Ab Initio Finite-Temperature Excitons.* Physical Review Letters **101** (10), (2008) (cit. on p. 1).

[91] A. Marini, C. Hogan, M. Grüning, and D. Varsano. *yambo: An ab initio tool for excited state calculations.* Computer Physics Communications **180** (8), (2009) (cit. on pp. 1, 12).

[92] N. Marzari, A. A. Mostofi, J. R. Yates, and I. Souza. *Maximally localized Wannier functions: Theory and applications.* Reviews of Modern Physics **84** (2012) (cit. on pp. 9–10).

[93] N. Marzari and D. Vanderbilt. *Maximally localized generalized Wannier functions for composite energy bands.* Physical Review B **56** (20), (1997) (cit. on p. 9).

[94] N. Marzari, D. Vanderbilt, A. De Vita, and M. C. Payne. *Thermal Contraction and Disordering of the Al(110) Surface.* Physical Review Letters **82** (16), (1999) (cit. on p. 8).

[95] R. Matzdorf. *Investigation of line shapes and line intensities by high-resolution UV-photoemission spectroscopy - Some case studies on noble-metal surfaces.* Surface Science Reports **30** (4-5), (1998) (cit. on p. 58).

[96] I. Mertig. *Transport properties of dilute alloys.* Reports on Progress in Physics **62** (2), (1999) (cit. on p. 19).

[97] M. Methfessel and A. T. Paxton. *High-precision sampling for Brillouin-zone integration in metals.* Physical Review B **40** (6), (1989) (cit. on p. 8).

[98] A. B. Migdal. *Interaction between electrons and lattice vibrations in a normal metal.* Soviet Physics JETP **34** (6), (1958) (cit. on pp. 1, 12).

[99] A. A. Mostofi, J. R. Yates, G. Pizzi, Y.-S. Lee, I. Souza, D. Vanderbilt, and N. Marzari. *An updated version of wannier90: A tool for obtaining maximally-localised Wannier functions.* Computer Physics Communications **185** (8), (2014) (cit. on p. 10).

[100] J. I. Mustafa, M. Bernardi, J. B. Neaton, and S. G. Louie. *Ab initio electronic relaxation times and transport in noble metals.* Physical Review B **94** (15), (2016) (cit. on pp. 1, 37–38).

[101] S. Nakajima. *Proceedings of the International Conference on Theoretical Physics at Kyoto-Tokyo.* 1954 (cit. on p. 1).

[102] S. Nakajima and M. Watabe. *On the Electron-Phonon Interaction in Normal Metals. I.* Progress of Theoretical Physics **30** (6), (1963) (cit. on p. 1).

[103] J. Noffsinger, F. Giustino, B. D. Malone, C.-H. Park, S. G. Louie, and M. L. Cohen. *EPW: A program for calculating the electron–phonon coupling using maximally localized Wannier functions.* Computer Physics Communications **181** (12), (2010) (cit. on pp. 9, 34).

[104] C.-H. Park, N. Bonini, T. Sohier, G. Samsonidze, B. Kozinsky, M. Calandra, F. Mauri, and N. Marzari. *Electron–Phonon Interactions and the Intrinsic Electrical Resistivity of Graphene.* Nano Letters **14** (3), (2014) (cit. on p. 34).

[105] J. P. Perdew and A. Zunger. *Self-interaction correction to density-functional approximations for many-electron systems.* Physical Review B **23** (10), (1981) (cit. on p. 5).

[106] W. E. Pickett. *Pseudopotential Methods in Condensed Matter Applications.* Computer Physics Reports **9** (3), (1989) (cit. on p. 6).

[107] S. Piscanec, M. Lazzeri, F. Mauri, A. C. Ferrari, and J. Robertson. *Kohn Anomalies and Electron-Phonon Interactions in Graphite.* Physical Review Letters **93** (18), (2004) (cit. on pp. 16, 32).

[108] C. N. Plâvitu. *On the Phonon Drag Effect Contribution to the Electrical Conductivity of Semiconductors.* physica status solidi (b) **32** (2), (1969) (cit. on p. 27).

[109] S. Poncé, G. Antonius, Y. Gillet, P. Boulanger, J. Laflamme Janssen, A. Marini, M. Côté, and X. Gonze. *Temperature dependence of electronic eigenenergies in the adiabatic harmonic approximation.* Physical Review B **90** (21), (2014) (cit. on p. 3).

[110] S. Poncé, E. R. Margine, C. Verdi, and F. Giustino. *EPW: Electron–phonon coupling, transport and superconducting properties using maximally localized Wannier functions.* Computer Physics Communications **209** (2016) (cit. on pp. 1, 9–10, 34, 42).

[111] R. E. Prange and L. P. Kadanoff. *Transport Theory for Electron-Phonon Interactions in Metals.* Physical review **134** (3A), (1964) (cit. on p. 1).

[112] C. A. Rahim and R. D. Barnard. *The absolute thermopower of lead above room temperature.* Journal of Physics D: Applied Physics **8** (11), (1975) (cit. on p. 48).

[113] O. D. Restrepo, K. Varga, and S. T. Pantelides. *First-principles calculations of electron mobilities in silicon: Phonon and Coulomb scattering.* Applied Physics Letters **94** (21), (2009) (cit. on p. 1).

[114] R. B. Roberts. *The absolute scale of thermoelectricity.* Philosophical Magazine **36** (1), (1977) (cit. on p. 48).

[115] S. Y. Savrasov and D. Y. Savrasov. *Electron-phonon interactions and related physical properties of metals from linear-response theory.* Physical Review B **54** (23), (1996) (cit. on pp. 1, 48).

[116] S. Y. Savrasov, D. Y. Savrasov, and O. K. Andersen. *Linear-response calculations of electron-phonon interactions.* Physical Review Letters **72** (3), (1994) (cit. on p. 1).

[117] M. Schackert, T. Märkl, J. Jandke, M. Hölzer, S. Ostanin, E. K. U. Gross, A. Ernst, and W. Wulfhekel. *Local Measurement of the Eliashberg Function of Pb Islands: Enhancement of Electron-Phonon Coupling by Quantum Well States.* Physical Review Letters **114** (4), (2015) (cit. on p. 14).

[118] G. Schierning. private communication (2016) (cit. on p. 48).

[119] T. J. Seebeck. *Ueber die magnetische Polarisation der Metalle und Erze durch Temperatur-Differenz.* Annalen der Physik **82** (1), (1826) (cit. on p. 25).

[120] L. J. Sham. *Electron-Phonon Interaction by the Method of Pseudo-potentials. Proceedings of the Physical Society.* 1961 (cit. on p. 1).

[121] F. W. Sheard. *The effect of phonon drag on the electrical resistivity of metals at low temperatures.* Journal of Physics F: Metal Physics **3** (11), (1973) (cit. on p. 27).

[122] W. Shockley and J. Bardeen. *Energy bands and mobilities in monatomic semiconductors.* Physical review **77** (3), (1950) (cit. on p. 1).

[123] J. Sjakste, N. Vast, and V. Tyuterev. *Ab initio Method for Calculating Electron-Phonon Scattering Times in Semiconductors: Application to GaAs and GaP.* Physical Review Letters **99** (23), (2007) (cit. on p. 1).

[124] I. Y. Sklyadneva, E. V. Chulkov, P. M. Echenique, and A. Eiguren. *Electron–phonon interaction and hole (electron) lifetimes on Be(0001).* Surface Science **600** (18), (2006) (cit. on p. 1).

[125] I. Y. Sklyadneva, E. V. Chulkov, W. D. Schöne, V. M. Silkin, R. Keyling, and P. M. Echenique. *Role of electron-phonon interactions versus electron-electron interactions in the broadening mechanism of the electron and hole linewidths in bulk Be.* Physical Review B **71** (17), (2005) (cit. on p. 1).

[126] I. Y. Sklyadneva, R. Heid, P. M. Echenique, K. B. Bohnen, and E. V. Chulkov. *Electron-phonon interaction in bulk Pb: Beyond the Fermi surface.* Physical Review B **85** (15), (2012) (cit. on pp. 1, 36–37, 43).

[127] S. Smirnov. *Physical Modeling of Electron Transport in Strained Silicon and Silicon-Germanium.* PhD thesis. 2004 (cit. on p. 42).

[128] J. O. Sofo and G. D. Mahan. *The best thermoelectric.* Proc. Natl. Acad. Sci. USA, 1996 (cit. on p. 24).

[129] I. Souza, N. Marzari, and D. Vanderbilt. *Maximally localized Wannier functions for entangled energy bands.* Physical Review B **65** (3), (2001) (cit. on p. 9).

[130] N. Tandon, J. D. Albrecht, and L. R. Ram-Mohan. *Electron-phonon interaction and scattering in Si and Ge: Implications for phonon engineering.* Journal of Applied Physics **118** (4), (2015) (cit. on p. 37).

[131] V. G. Tyuterev, S. V. Obukhov, N. Vast, and J. Sjakste. *Ab initio calculation of electron-phonon scattering time in germanium.* Physical Review B **84** (3), (2011) (cit. on p. 1).

[132] D. Vanderbilt. *Soft self-consistent pseudopotentials in a generalized eigenvalue formalism.* Physical Review B **41** (11), (1990) (cit. on p. 6).

[133] M. Wagner-Reetz, D. Kasinathan, W. Schnelle, R. Cardoso-Gil, H. Rosner, Y. Grin, and P. Gille. *Phonon-drag effect in* $FeGa_3$. Physical Review B **90** (19), (2014) (cit. on p. 27).

[134] Z. Wang, S. Wang, S. Obukhov, N. Vast, J. Sjakste, V. Tyuterev, and N. Mingo. *Thermoelectric transport properties of silicon: Toward an ab initio approach.* Physical Review B **83** (20), (2011) (cit. on pp. 1, 42).

[135] G. H. Wannier. *The Structure of Electronic Excitation Levels in Insulating Crystals.* Physical review **52** (3), (1937) (cit. on p. 9).

[136] E. L. Wolf. *Principles of Electron Tunneling Spectroscopy: Second Edition.* Oxford University Press, 2012 (cit. on p. 14).

[137] P. Zahn. *Screened Korringa-Kohn-Rostoker-Methode für Vielfachschichten.* PhD thesis. 1998 (cit. on p. 37).

[138] A. D. Zdetsis, E. N. Economou, and D. A. Papaconstantopoulos. *Ab initio bandstructure of lead.* Journal of Physics F: Metal Physics **10** (6), (1980) (cit. on p. 36).

[139] J. Zhou, B. Liao, and G. Chen. *First-principles calculations of thermal, electrical, and thermoelectric transport properties of semiconductors.* Semiconductor Science and Technology **31** (4), (2016) (cit. on p. 1).

[140] J. Zhou, B. Liao, B. Qiu, S. Huberman, K. Esfarjani, M. S. Dresselhaus, and G. Chen. *Ab initio optimization of phonon drag effect for lower-temperature thermoelectric energy conversion.* Proceedings of the National Academy of Sciences **112** (48), (2015) (cit. on p. 1).

[141] J.-J. Zhou and M. Bernardi. *Ab initio electron mobility and polar phonon scattering in GaAs.* Physical Review B **94** (20), (2016) (cit. on p. 37).

[142] X. Zhu, L. Santos, R. Sankar, S. Chikara, C. Howard, F. C. Chou, C. Chamon, and M. El-Batanouny. *Interaction of Phonons and Dirac Fermions on the Surface of* Bi_2Se_3*: A Strong Kohn Anomaly.* Physical Review Letters **107** (18), (2011) (cit. on p. 32).

[143] J. M. Ziman. *Electrons and phonons.* Oxford University Press, 1963 (cit. on pp. 19, 21, 27, 48).

List of publications

[FR1] N. F. Hinsche, F. Rittweger, M. Hölzer, P. Zahn, A. Ernst, and I. Mertig. *Ab initio description of the thermoelectric properties of heterostructures in the diffusive limit of transport.* physica status solidi (a) **213** (3), (2015).

[FR2] N. F. Hinsche, S. Zastrow, J. Gooth, L. Pudewill, R. Zierold, F. Rittweger, T. Rauch, J. Henk, K. Nielsch, and I. Mertig. *Impact of the Topological Surface State on the Thermoelectric Transport in* Sb_2Te_3 *Thin Films.* ACS Nano **9** (4), (2015).

[FR3] F. Rittweger, N. F. Hinsche, P. Zahn, and I. Mertig. *Signature of the topological surface state in the thermoelectric properties of* Bi_2Te_3. Physical Review B **89** (3), (2014).

[FR4] F. Rittweger, N. F. Hinsche, and I. Mertig. *Phonon limited electronic transport in Pb.* Journal of Physics: Condensed Matter **29** (355501), (2017).

Danksagung

Zum Ende meiner Promotionszeit möchte ich mich bei Allen bedanken, die mich in den letzten Jahren auf die eine oder andere Art und Weise unterstützt und begleitet haben.

Zuallerst danke ich Frau Prof. Ingrid Mertig für die Aufnahme in ihre Gruppe und die langjährige wissenschaftliche Betreuung. Ich bin sowohl für die fachlichen Diskussionen als auch die privaten Ratschläge sehr dankbar und bin froh, in dieser gutherzigen und produktiven Umgebung gearbeitet haben zu dürfen.

In besonderer Weise bedanke ich mich bei Dr. Nicki Hinsche für die, wenn benötigt, fast tägliche Bereitschaft, mit mir auch über kleinste fachliche und technische Details zu sprechen und immer einen Rat oder eine Idee parat gehabt zu haben. Auch abseits der wissenschaftlichen Arbeit gab es viele interessante Gespräche, in denen sich besonders meine Kenntnisse über Whisky und amerikanischen Basketball vervielfältigt haben.

Weiterhin danke ich auch allen anderen aktuellen und ehemaligen Gruppenmitgliedern für eine abwechslungsreiche und humorvolle Zeit im Büro. Stellvertretend möchte ich hier meine Bürokollegen Markus Flieger, Dr. Steven Achilles und Dr. Nicki Hinsche sowie die regen Teilnehmer der Kaffeerunde Dr. Tomáš Rauch, Dr. Igor Maznichenko und Michael Strauch erwähnen, die für Streiche, Witze aber auch vielschichtige Diskussionen immer zu haben waren.

Stellvertretend für viele aus meinem Jahrgang geht ein spezieller Dank an Marco John, Olga Wid sowie Dr. Matthias Maiberg für die interessanten Diskussionen und Gespräche während der Mittagspausen und vor allem für die schöne Zeit und zahlreichen Aktivitäten abseits der Universität. Für die vielen tollen Momente, Geschichten und Erlebnisse bin ich sehr dankbar.

Ebenso bedanke ich mich bei den Gutachtern, die sich die Zeit genommen und sich mit dieser Arbeit beschäftigt haben.

Als Letztes möchte ich mich bei meiner Familie und meinen Eltern für ihre Unterstützung, Geduld und Ratschläge in den vergangenen Jahren bedanken. Meiner Freundin Jessica danke ich besonders, war sie doch immer eine verständnisvolle Partnerin, die mich auch in schwierigen Situationen stets unterstützt hat.

Curriculum vitae

Personal information

Name	Florian Rittweger
Address	August-Bebel-Str. 9 in 06108 Halle (Saale), Germany
Date and place of birth	9th of June, 1988 Halle (Saale)

Education

since 04/2013	PhD studies at the “Martin-Luther-Universität Halle-Wittenberg” and the “Max Planck Institute of Microstructure Physics”, Halle (Saale)
10/2010-03/2013	Studies of Physics at the “Martin-Luther-Universität Halle-Wittenberg”, Halle(Saale) - Master of Science in Physics ”Rolle des Oberflächenzustandes topologischer Isolatoren in den Transportkoeffizienten”
10/2007-10/2010	Studies of Physics at the “Martin-Luther-Universität Halle-Wittenberg”, Halle(Saale) - Bachelor of Science in Physics ”Transporteigenschaften thermoelektrischer Materialien”
08/2000-07/2007	Grammar school, ”Gymnasium im Bildungszentrum”, Halle (Saale)
09/1998-07/2000	Secondary school, ”Heinrich Heine”, Halle (Saale)
08/1994-07/1998	Elementary school, ”Ernest Hemingway”, Halle (Saale)

Academic career

01/2015-06/2017	Research assistant at the “Martin-Luther-Universität Halle-Wittenberg”, Halle(Saale)
04/2013-12/2014	Research assistant at the “Max Planck Institute of Microstructure Physics”, Halle(Saale)
04/2011-12/2012	Student assistant at the “Martin-Luther-Universität Halle-Wittenberg”, Halle(Saale)
01/2011-02/2011	

Miscellaneous

11/2015	Part of the team that won the Hugo-Junkers-Preis ”Nanostrukturierte thermoelektrische Schichtsysteme”

Halle, 7th February 2018

Eidesstattliche Erklärung

Hiermit erkläre ich, gemäß §5 der Promotionsordnung der Naturwissenschaftlichen Fakultät I, II und III der Martin-Luther-Universität Halle-Wittenberg vom 13.07.2016, dass ich die vorliegende Arbeit

INFLUENCE OF THE ELECTRON-PHONON INTERACTION
ONTO ELECTRONIC TRANSPORT IN METALS

selbständig und ohne fremde Hilfe angefertigt und keine anderen Quellen und Hilfsmittel als die von mir angegebenen benutzt habe. Wörtlich oder inhaltlich entnommene Stellen der benutzen Werke sind als solche kenntlich gemacht.

Ich versichere, die vorliegende Dissertation in dieser oder einer anderen Form zu keinem Zeitpunkt an einer anderen wissenschaftlichen Einrichtung zur Erlangung eines akademischen Grades eingereicht zu haben.

Weiterhin erkläre ich, dass ich nicht vorbestraft bin und kein Ermittlungsverfahren gegen mich eingeleitet ist.

Halle, den 07.02.2018
Florian Rittweger